JETP Letters, Vol. 76, No. 6, 2002, pp. 327–331. Translated from Pis'ma v Zhurnal Éksperimental'noĭ i Teoreticheskoĭ Fiziki, Vol. 76, No. 6, 2002, pp. 387–391.

Gell-Mann–Low Function in QCD

I. M. Suslov

Kapitza Institute for Physical Problems, Russian Academy of Sciences, ul. Kosygina 2, Moscow, 117973 Russia
e-mail: suslov@kapitza.ras.ru

Received April 29, 2002; in final form, June 5, 2002

The Gell-Mann–Low function in QCD $\beta(g)$ ($g = \bar{g}^2/16\pi^2$, where $\bar{g}$ is the coupling constant in the Lagrangian) is shown to behave in the strong-coupling region as $\beta_\infty g^\alpha$, where $\alpha \approx -13$ and $\beta_\infty \sim 10^5$. © *2002 MAIK "Nauka/Interperiodica".*

PACS numbers: 12.38.Cy

Recently, using an algorithm proposed in [1, 2] for summing divergent series of perturbation theory, I determined the Gell-Mann–Low function of φ^4 theory [1, 2] and QED [3]. Here, this algorithm is applied to QCD, for which previous calculations provided ambiguous results [4].

1. Information about all terms of the perturbation series can be acquired by interpolating first terms with the Lipatov asymptotic behavior [5]. The first four terms in the expansion of the Gell-Mann–Low function for QCD are known in the MS scheme [6]:

$$\beta(g) = \sum_{N=0}^{\infty} \beta_N g^N = \beta_2 g^2 + \beta_3 g^3 + \beta_4 g^4 + \ldots, \qquad g = \bar{g}^2/16\pi^2, \tag{1}$$

where

$$-\beta_2 = 11 - \frac{2}{3}N_\mathrm{f}, \quad -\beta_3 = 102 - \frac{38}{3}N_\mathrm{f},$$

$$-\beta_4 = \frac{2857}{2} - \frac{5033}{18}N_\mathrm{f} + \frac{325}{54}N_\mathrm{f}^2,$$

$$-\beta_5 = \left[\frac{149\,753}{6} + 3564\zeta(3)\right] - \left[\frac{1\,078\,361}{162} + \frac{6508}{27}\zeta(3)\right]N_\mathrm{f} + \left[\frac{50\,065}{162} + \frac{6472}{81}\zeta(3)\right]N_\mathrm{f}^2 + \frac{1093}{729}N_\mathrm{f}^3. \tag{2}$$

Here, N_f is the number of types of quarks and $\bar{g}$ is the coupling constant in the QCD Lagrangian

$$L = -\frac{1}{4}F^a_{\mu\nu}F^a_{\mu\nu} - \frac{1}{2\xi}(\partial_\mu A^a_\mu)^2 + \sum_f \bar{\psi}_\mathrm{f}\hat{D}\psi_\mathrm{f} + \partial_\mu\bar{\omega}^a(\partial_\mu\omega^a - \bar{g}f^{abc}\omega^b A^c_\mu), \tag{3}$$
$$F^a_{\mu\nu} = \partial_\mu A^a_\nu - \partial_\nu A^a_\mu + \bar{g}f^{abc}A^b_\mu A^c_\nu,$$
$$\hat{D} = i\gamma_\mu(\partial_\mu - i\bar{g}A^a_\mu T^a),$$

where A^a_ν, ψ_f, and ω^a are gluon, quark, and ghost fields, respectively; T^a and f^{abc} are the generators of the fundamental representation and structure constants of the Lie algebra, respectively; ξ is the gauge parameter; and subscript f specifies the type of quark.

2. The asymptotic behavior in perturbation theory was discussed for Yang–Mills fields [7–9] and QCD [10, 11]. However, the results are not quite general. Below, this deficiency will be partially compensated.[1]

The pre-exponential factor of the most general functional integral for QCD involves M gluon, $2L$ ghost, and $2K$ quark fields, i.e.,

$$Z_{MLK} = \int DAD\bar{\omega}D\omega D\bar{\psi}D\psi A(x_1)\ldots A(x_M) \times \omega(y_1)\bar{\omega}(\bar{y}_1)\ldots\omega(y_L)\bar{\omega}(\bar{y}_L)\psi(z_1) \times \bar{\psi}(\bar{z}_1)\ldots\psi(z_K)\bar{\psi}(\bar{z}_K)\exp(-S\{A, \bar{\omega}, \omega, \bar{\psi}, \psi\}), \tag{4}$$

where vector indices immaterial for further consideration are omitted. The substitution $A \longrightarrow B/\bar{g}$ reduces the Euclidean action to the form

$$S\{A, \bar{\omega}, \omega, \bar{\psi}, \psi\} \longrightarrow \frac{S\{B\}}{\bar{g}^2} + \int d^4x\left[\bar{\omega}\hat{Q}\omega + \sum_f \bar{\psi}_\mathrm{f}\hat{D}\psi_\mathrm{f}\right], \tag{5}$$

[1] My view on the renormalon contributions was formulated in [3]. The existence of renormalon singularities in QCD was neither proven nor disproven, and I will assume that they are absent.

and the integration over the fermion fields yields

$$Z_{MLK} = (1/\bar{g})^M \int DAB(x_1)\dots B(x_M) \times G(y_1, \bar{y}_1)\dots G(y_L, \bar{y}_L)\bar{G}(z_1, \bar{z}_1)\dots \tilde{G}(z_K, \bar{z}_K) \times \det\hat{Q}(\det\hat{D})^{N_f} \exp\{-S\{B\}/\bar{g}^2\} + \dots, \quad (6)$$

where G and $\tilde{G}$ are the Green's functions of the operators $\hat{Q}$ and $\hat{D}$, and ellipsis means terms with other pairings. It is important that $S\{B\}$, G, and $\tilde{G}$ are independent of $\bar{g}$. Functional integral (6) is determined by the Yang–Mills action, and the asymptotic behaviors of its expansion coefficients in $\bar{g}$ are calculated by the Lipatov method [5]. For the saddle-point configuration, $\bar{g} \sim N^{-1/2}$, where N is the order of perturbation theory. Therefore, each field $A(x_i)$ in the pre-exponential factor in Eq. (4) provides the factor $N^{1/2}$, whereas other fields do not give N-dependent factors. The dependence of the expansion coefficients on N is determined according to [10]; it differs from the result for the quark correlation function only by the factor $N^{M/2}$. The Nth-order contribution to Z_{MLK} has the form

$$[Z_{MLK}]_N \bar{g}^{2N} = \text{const}(16\pi^2)^{-N} \times \Gamma\left(N + \frac{M}{2} + 4N_c + \frac{11(N_c - N_f)}{6}\right)\bar{g}^{2N}, \quad (7)$$

for even M and, with the additional factor $\bar{g}N^{1/2}$, for odd M (N_c is a number of colors).[2]

Using the result for the functional integral and applying the algebra of factorial series [16], one can easily obtain the result for any quantity. Let $F_N\bar{g}^{2N}$ be the Nth-order contribution to the vacuum integral ($M = L = K = 0$). Then, the general term of asymptotic function (except for a coefficient) has the form $NF_N\bar{g}^{2N}$ for the gluon propagator Δ, $F_N\bar{g}^{2N}$ for the ghost propagator G and quark propagator G_f, $NF_N\bar{g}^{2N+1}$ for the gluon–ghost vertex γ_3 and gluon–quark vertex γ_3^f, $N^2F_N\bar{g}^{2N+1}$ for the three-gluon vertex Γ_3, and $N^3F_N\bar{g}^{2N+2}$ for the four-gluon vertex Γ_4. In view of the generalized Ward identities $\Gamma_3 \sim \gamma_3 G$ and $\Gamma_4 \sim \Gamma_3^2\Delta$, the leading contributions to the asymptotic behaviors of Γ_3 and Γ_4 cancel each other, and the invariant charge has the general expansion term $NF_N\bar{g}^{2N+2}$ or $F_N\bar{g}^{2N}$ when determining it from any vertex. The expansion of the β function has the same form [5]. Since $g = \bar{g}^2/16\pi^2$, the coefficients of series (1) have the form

$$\beta_N = \text{const}\Gamma\left(N + 4N_c + \frac{11(N_c - N_f)}{6}\right). \quad (8)$$

This result for $N_c = 2$ and $N_f = 0$ agrees with the result obtained in [7].

3. Series (1) is of constant sign, and the familiar problem arises as to how one can treat the poorly defined Borel integral. In particular, the principal-value interpretation of this integral is not necessarily correct [17]. The gamma function is generally defined as

$$\Gamma(z) = \sum_i \gamma_i \int_{C_i} dx e^{-x} x^{z-1}, \quad \sum_i \gamma_i = 1, \quad (9)$$

where C_1, C_2, … are arbitrary contours beginning at the origin and tending to infinity in the right half-plane. The Borel transformation of series (1) yields

$$\beta(g) = \sum_i \gamma_i \int_{C_i} dx e^{-x} x^{b_0 - 1} B(gx), \quad B(z) = \sum_{N=0}^{\infty} B_N z^N, \quad B_N = \frac{\beta_N}{\Gamma(N + b_0)}, \quad (10)$$

where b_0 is an arbitrary parameter. If the Borel transform $B(z)$ has singularities in the right half-plane, contours C_i are no longer equivalent and cannot be reduced to the positive semiaxis, as was possible in Eq. (9). For this reason, the summation result depends on the choice of γ_i and C_i.[3] We bypass this problem as follows. For the power behavior of the Borel transform at infinity, i.e., when $B(z) \sim z^\alpha$, we have

$$\beta(g) = \beta_\infty g^\alpha, \quad g \longrightarrow \infty \quad \text{and} \quad \beta(g) = \bar{\beta}_\infty |g|^\alpha, \quad g \longrightarrow -\infty, \quad (11)$$

where the exact relation between β_∞ and $\bar{\beta}_\infty$ depends on the chosen γ_i and C_i, but $\beta_\infty \sim \bar{\beta}_\infty$ in the general case. Therefore, index α can be determined and β_∞ can be estimated by summing series (1) at negative values of g.

4. According to the algorithm developed in [1, 2], the resummation of the alternating series with the coef-

[2] The term $M/2$ in the argument of gamma function in Eq. (7) is related to the number of external fields, $4N_c$ is half the number of zero modes, and the term $11(N_c - N_f)/6$ arises because certain zero modes are soft, under more rigorous consideration, and must be nontrivially integrated. For the quark correlation function, Eq. (6) involves divergences, which were removed in [10, 11] by a doubtful method [14]. These divergences are absent for $M \geq 1$.

[3] Results for different γ_i and C_i differ by terms similar to $\exp(-a/g)$, and these nonperturbative contributions must generally be added to the Borel integral. For correctly chosen γ_i and C_i, these contributions are included in the Borel integral and must not be explicitly taken into account.

ficients behaving asymptotically as $ca^N\Gamma(N + b)$ provides the convergent series with the coefficients

$$U_N = \sum_{K=1}^{N} B_K a^{-K}(-1)^K C_{N-1}^{K-1}, \quad (12)$$

whose behavior for large N

$$U_N = U_\infty N^{\alpha-1}, \quad U_\infty = \frac{\bar{\beta}_\infty}{a^\alpha \Gamma(\alpha)\Gamma(b_0+\alpha)} \quad (13)$$

determines the parameters of asymptotic function (11). The coefficient function is interpolated via the formula

$$\beta_N = ca^N N^{\tilde{b}}\Gamma(N + b - \tilde{b}) \times\left[1 + \frac{A_1}{N-\tilde{N}} + \frac{A_2}{(N-\tilde{N})^2} + \ldots\right] \quad (14)$$

by breaking the series and choosing the coefficients A_K from agreement with Eq. (2). The optimal parameterization of the asymptotic behavior with $\tilde{b} = b - 1/2$ is taken [2], and parameter $\tilde{N}$ is used to control the stability of results and to optimize the calculations.

Similar to QED, the parameter c of the Lipatov asymptotic behavior is unknown, and it was determined through the interpolation in [3]. In the case under consideration, this procedure gives large uncertainty in the results, which is not reduced by optimization. For this reason, interpolation was carried out for a test c value, which then varied from 10^{-5} to 1.[4] Under this variation, the results change only slightly compared to other uncertainties. The results below were obtained for $N_c = 3$, $N_f = 0$, and $c = 10^{-5}$.

Processing U_N in terms of the power law and considering the dependence of χ^2 on $\tilde{N}$, we separate the interval $0.5 \lesssim \tilde{N} \lesssim 2.0$, where the χ^2 values are minimal. This procedure determines the set of interpolations consistent with the power behavior of U_N. The typical behavior of χ^2 and effective values U_∞ and α as functions of b_0 (Fig. 1) indicates that $\alpha \approx -15$. Indeed, U_∞ determined by Eqs. (13) changes sign at $b_0 = -\alpha \approx 15.5$. For this b_0 value, χ^2 has a minimum, because the leading contribution $U_\infty N^{\alpha-1}$ is equal to zero due to the pole of the gamma function in Eq. (13), and we have power behavior $U_N \sim N^{\alpha'-1}$ corresponding to the first correction to the asymptotic behavior of $\beta(g)$ [we assume that $\beta(g) = \beta_\infty g^\alpha + \beta'_\infty g^{\alpha'} + \ldots$ for large g values]. The α_{eff}

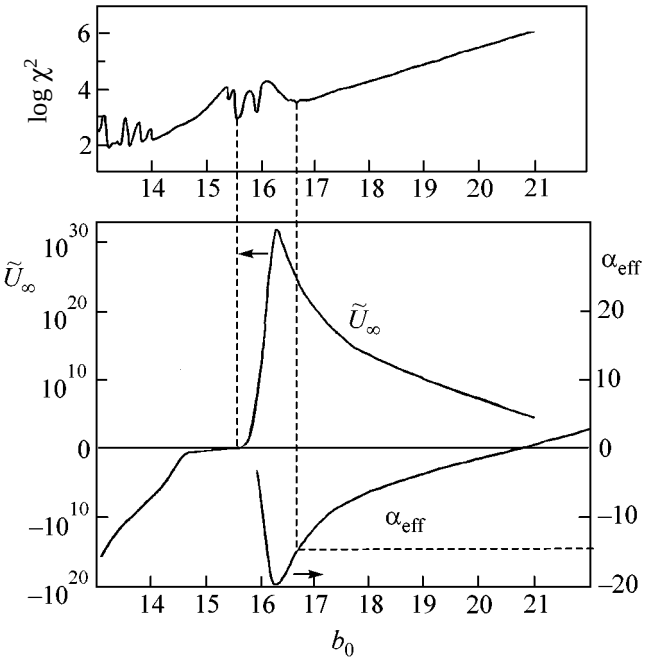

Fig. 1. Quantities χ^2, α_{eff}, and $\tilde{U}_\infty = U_\infty\Gamma(b_0 + 2)$ vs. b_0 for the optimal interpolation with $\tilde{N} = 1.58$ and averaging interval $23 \le N \le 35$. Function $\tilde{U}_\infty(b_0)$ for $|\tilde{U}_\infty| < 10$ is shown schematically. The minima at $b_0 = 15.4$ and 15.9 are treated as the satellites of the principal minimum at $b_0 = 15.5$, because they, together with the principal minimum, are shifted with varying parameters.

value in the first (from large b_0) minimum of χ^2 is closest to the exact value $\alpha \approx -15$, because the leading correction to asymptotic function (13) vanishes at $b_0 = -\alpha'$. The results obtained by the above methods of estimating index α are close only for $\tilde{N}$ values close to the optimal value $\tilde{N} = 1.58$ (Fig. 1) but are inconsistent for $\tilde{N}$ values far from the optimal value.

The result for index α cannot immediately be taken as final. First, the large index can imitate an exponential. Second, for $\alpha = 0, -1, -2, \ldots$, the leading contribution to the asymptotic behavior of U_N vanishes due to the pole of $\Gamma(\alpha)$ [see Eq. (13)], and the observed result can correspond, e.g., to α' rather than to the principal index α [2]. In view of these circumstances, we analyze the function $W(g) = g^{n_s}\beta(g)$ and increase integer parameter n_s until the observed index $\alpha_W = \alpha + n_s$ becomes positive. The results (Fig. 2a) conclusively demonstrate that we observe a large negative noninteger index rather than an exponential (if it were $\alpha = -n$, we would observe the behavior shown in the insert). Each point in Fig. 2a is obtained by independent optimization in $\tilde{N}$. The optimal $\tilde{N}$ value decreases mono-

[4] Parameter c is equal to the product of the square of the 't Hooft constant c_H in the expression for one-instanton contribution [12, 13] ($c_H^2 \sim 10^{-5}$ and 10^{-4} for $N_f = 0$ and 3, respectively) and the dimensionless integral of the instanton configuration. The latter factor can be rather large (characteristic scale is $8\pi^2$).

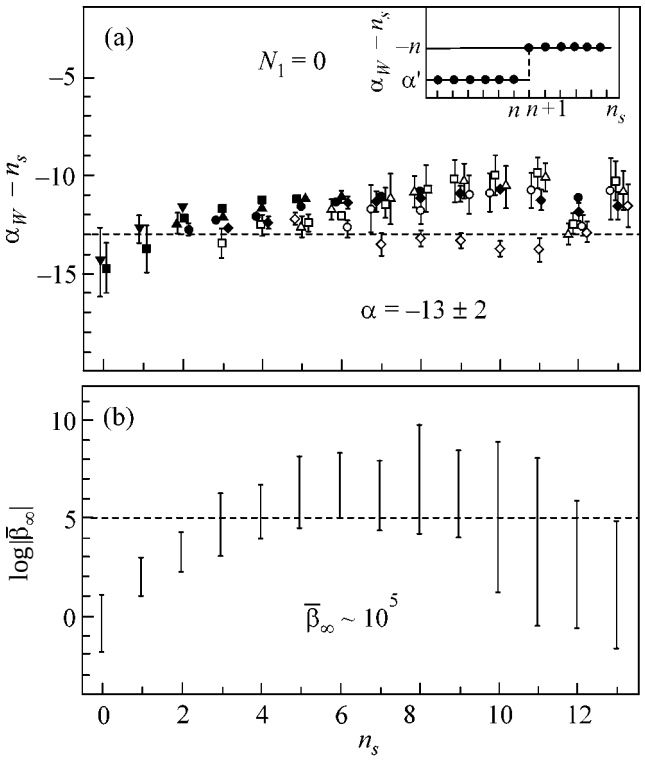

Fig. 2. (a) Index α_W obtained by summing the series for function $W(g) = g^{n_s}\beta(g)$ vs. n_s for various averaging intervals $N_{\min} \le N \le N_{\max}$: (▼) for $N_{\min} = 22 + n_s$ and $N_{\max} = 35 + n_s$ and (■, ▲, ●, □, △, ○, ◇) for sequentially increasing $N_{\min}$ by one unit; (b) parameter $\bar{\beta}_\infty$ as a function of n_s.

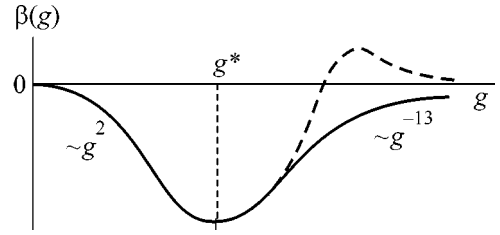

Fig. 3.

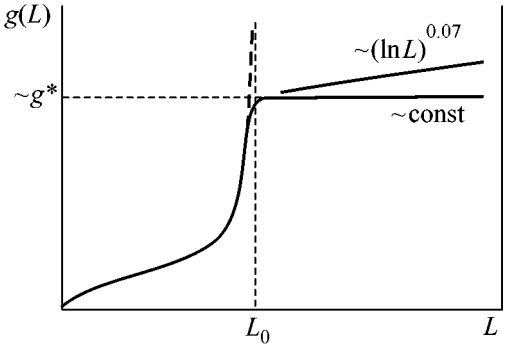

Fig. 4.

tonically with increasing n_s. Uncertainty in the results is primarily attributed to the dependence at the lower bound of averaging interval $N_{\min} \le N \le N_{\max}$. The upper points in Fig. 2a correspond to small $N_{\min}$ and to $\chi^2 \sim 10^6$ in the minima. As $N_{\min}$ increases, α decreases monotonically until χ^2 reaches a value of $\sim 10^3$ (lower points). With a further increase in $N_{\min}$, the pattern of χ^2 minima becomes indistinct, and the uncertainty of the results increases considerably. We admit a certain small decrease in α until the required values $\chi^2 \sim 10$ are reached, which is taken into account when errors are estimated. The uncertainty in parameter $\bar{\beta}_\infty$ is of several orders of magnitude (Fig. 2b), but the most probable value is $\sim 10^5$, which is consistent with the basic array of data. Thus, we have for $N_f = 0$

$$\alpha = -13 \pm 2, \quad \bar{\beta}_\infty \sim 10^5. \tag{15}$$

For $N_f = 3$, one has $\alpha = -12 \pm 3$ and the same most probable value $\bar{\beta}_\infty$ (whereas the total scatter is $\bar{\beta}_\infty = 1$–10^7). The stability in the results against a change in the summation procedure testifies that their uncertainty is adequately estimated. Some underestimation of the error is possible due to the nonlinear effects [3] and because the asymptotic behavior is reached slowly.

Large uncertainty in $\bar{\beta}_\infty$ corresponds to comparatively small uncertainty in the β function: we found that the one-loop law $\beta_2 g^2$ was matched with asymptotic function (11) in characteristic scale $g^* \sim 2$, and $\bar{\beta}_\infty$ changes by four orders of magnitude as g^* changes by a factor of two. The sign of $\bar{\beta}_\infty$ is indeterminate in negative α_W region, because error in α is large and the factor $\Gamma(\alpha)$ in Eq. (13) is alternating, but this sign is definitely negative in positive α_W region (large n_s values). Figure 3 shows (solid line) the behavior of β function for $g < 0$ and (dashed line) the analytic continuation to positive g values, where the behavior is qualitatively the same, but the sign of asymptotic function (11) can change.[5] Nevertheless, the behavior of the effective coupling constant as a function of the length scale L is definite (Fig. 4). As is known, $g(L)$ in the one-loop approximation has a pole at $L = L_0 = 1/\Lambda_{QCD}$ (dashed line in Fig. 4). For the resulting β function (Fig. 3), $g(L)$ increases near L_0 up to $\sim g^*$ and then either (for $\beta_\infty > 0$) becomes constant or (for $\beta_\infty < 0$) increases as $(\ln L)^{0.07}$, which is close to a constant.

In the weak-coupling region, interaction $V(L)$ between quarks is described by he modified Coulomb law $\bar{g}^2(L)/L$, and the sharp increase in $\bar{g}(L)$ near $L = L_0$ testifies to the tendency to confinement. In the strong-coupling region, the relation between $V(L)$ and $\bar{g}(L)$ is

[5] In particular, $\beta_\infty = \bar{\beta}_\infty \cos(\pi\alpha)$ when the Borel integral is treated as the principal-value integral.

unknown, but Wilson [17] obtained the following result for the lattice QCD version:

$$V(L) = \frac{\ln 3\bar{g}^2(a)}{a^2}L, \quad \bar{g}(a) \gg 1, \qquad (16)$$

where a is the lattice constant. From the condition that the result is independent of a, the β function in the strong-coupling region is estimated as $\beta(g) \sim g\ln g$ [18], which is, however, incorrect. The cross size of the string in the region $a \gg 1/\Lambda_{QCD}$ is equal to $\sim a$, which is considerably higher than its actual physical size $\sim 1/\Lambda_{QCD}$. Therefore, the lattice introduces strong distortions, and there is no reason to expect that the result is independent of a. These reasons exist in the region $a \ll 1/\Lambda_{QCD}$, where, however, the coupling constant $\bar{g}(a)$ becomes small, and Eq. (16) does not apply. Thus, Eq. (16) is meaningful only for $a \sim 1/\Lambda_{QCD}$. In the saturation region, $\bar{g}(L) \sim \sqrt{2 \times 16\pi^2} \sim 20$, and, because of a sharp increase in $g(L)$ near $L = L_0$ (Fig. 4), the conditions $a \sim 1/\Lambda_{QCD}$ and $\bar{g}(a) \gg 1$ are compatible, which likely justifies the applicability of Eq. (16) to actual QCD.

This work was supported by INTAS (grant no. 99-1070), the Russian Foundation for Basic Research (project no. 00-02-17129), and the Russian Foundation for Support of Science.

REFERENCES

1. I. M. Suslov, Pis'ma Zh. Éksp. Teor. Fiz. **71**, 315 (2000) [JETP Lett. **71**, 217 (2000)].
2. I. M. Suslov, Zh. Éksp. Teor. Fiz. **120**, 5 (2001) [JETP **93**, 1 (2001)].
3. I. M. Suslov, Pis'ma Zh. Éksp. Teor. Fiz. **74**, 211 (2001) [JETP Lett. **74**, 191 (2001)].
4. D. I. Kazakov, in *Proceedings of the Conference QUARKS-80, Sukhumi, 1980* (INR, Moscow, 1981), p. 52.
5. L. N. Lipatov, Zh. Éksp. Teor. Fiz. **72**, 411 (1977) [Sov. Phys. JETP **45**, 216 (1977)].
6. T. van Ritbergen, J. A. M. Vermaseren, and S. A. Larin, Phys. Lett. B **400**, 379 (1997).
7. E. B. Bogomolny and V. A. Fateyev, Phys. Lett. B **71**, 93 (1977).
8. L. N. Lipatov, A. P. Bukhvostov, and E. I. Malkov, Phys. Rev. D **19**, 2974 (1979).
9. E. B. Bogomolny, V. A. Fateyev, and L. N. Lipatov, Sov. Sci. Rev., Sect. A **2**, 247 (1980).
10. I. I. Balitsky, Phys. Lett. B **273**, 282 (1991).
11. S. V. Faleev and P. G. Silvestrov, Nucl. Phys. B **463**, 489 (1996).
12. G. t'Hooft, Phys. Rev. D **14**, 3433 (1976).
13. C. Bernard, Phys. Rev. D **19**, 3013 (1979).
14. I. M. Suslov, Zh. Éksp. Teor. Fiz. **116**, 369 (1999) [JETP **89**, 197 (1999)].
15. I. M. Suslov, Usp. Fiz. Nauk **168**, 503 (1998) [Phys. Usp. **41**, 441 (1998)].
16. R. Seznec and J. Zinn-Justin, J. Math. Phys. **20**, 398 (1979).
17. K. Wilson, Phys. Rev. D **10**, 2445 (1974).
18. C. Callan, R. Dashen, and D. Gross, Phys. Rev. D **20**, 3279 (1979).

Translated by R. Tyapaev

JETP Letters, Vol. 76, No. 6, 2002, pp. 332–336. From Pis'ma v Zhurnal Éksperimental'noĭ i Teoreticheskoĭ Fiziki, Vol. 76, No. 6, 2002, pp. 392–396.

The Upper Limit of the Branching Ratio for Radiative Beta Decay of Free Neutrons¶

M. Beck[1], J. Byrne[2], R. U. Khafizov[3], V. Yu. Kozlov[1], Yu. A. Mostovoi[3], O. V. Rozhnov[4], N. Severijns[1], and V. A. Solovei[4]

[1] *Katholieke Universiteit Leuven, B-3001 Leuven, Belgium*
[2] *University of Sussex, Brighton BN1 9RH, Sussex, UK*
[3] *Russian Research Centre Kurchatov Institute, Moscow, 127562 Russia*
[4] *St. Petersburg Nuclear Physics Institute, Gatchina, 188350 Russia*

Received August 9, 2002

We conducted an experiment on radiative neutron beta decay on an intensive cold-neutron beam at ILL during April and May 2002. This work is dedicated to the analysis of the methodology and the results of the study. The main outcome of this experiment is the branching ratio (BR) for the rare neutron-decay mode in the gamma-ray quanta energy region from 35 to 100 keV. The limit obtained is $BR < 6.9 \times 10^{-3}$ (90% C.L.), which is only a few permilles greater than the theoretical BR value calculated within the standard weak-interactions model.

PACS numbers: 13.30.Ce; 13.40.Hq; 14.20.Dh

1. Introduction. This experiment is the first step in a research for radiative neutron beta decay, where, along with the usual three particles (i.e., electron, antineutrono, and proton), another particle is created, namely, a gamma-ray quantum:

$$n \longrightarrow p + e + \bar{\nu} + \gamma.$$

It is necessary to note that this decay branch is the most intensive of all the rare elementary-particle decay modes and is therefore well investigated for practically all elementary-particle decays where charged particles are formed in the final state. However, this branch is yet to be discovered for the neutron [1]. Calculations of the gamma-ray quanta spectrum were conducted in the framework of standard electroweek theory, and the branching ratio (BR) for this decay mode as a function of the gamma energy threshold was given in [2, 3].

The experiment was conducted in the radiative gamma-ray quanta energy region from 35 to 100 keV, and for this region the theoretical BR value is about one permille [2, 3]. It is not such a difficult task to measure this relatively large value, as a rather significant background could be overcome with the help of triple electron, gamma quanta, and recoil proton coincidences. The presence of such a coincidence will be the factor used to identify a radiative neutron decay event. An ordinary neutron beta decay is then defined by the double coincidences of electron and recoil proton. This double coincidence scheme has already been used in measuring the emission asymmetry [4, 5] of the decay electron by the joint group of physicists from PNPI (Gatchina) and RSC Kurchatov Institute (Moscow). The setup used in those experiments is upgraded now for the conduction of the experiment on radiative neutron decay suggested here.

This upgrade was realized by placing an additional gamma-ray quanta detector in the existing vacuum chamber, the size and geometry of which allowing to do so. However, the simple addition of a third gamma-ray quanta detector to the two detectors for the decay electrons and recoil protons would not suffice by itself. The point is that in this experiment, besides the noncorrelated background, there is also a correlated background of bremstrahlung gamma-ray quanta which fully simulates the desired fundamental process. It is therefore necessary to concider this problem in more detail.

Indeed, when measuring the BR, a correlated background will occur, which is impossible to decrease even with triple coincidences of the electron, the photon, and the proton. This background is connected with bremsstrahlung emission of the electron traveling through the plastic scintillator, which completely simulates the events of radiative neutron decay and is quite significant even when the thickness of the plastic scintillator is only 3 mm. The idea of diminishing this correlated background centers around using the spatial resolution. If a sectioned *e*-gamma detector is used and electron and gamma-ray quanta are registered in different sections, then the background can be overcome completely, because the bremsstrahlung emission occurs only in the section that registers electrons. Within the electroweak interaction model, calculations demonstrate one important particularity of radiative emission for the rare neutron mode being studied: it is

¶This article was submitted by the authors in English.

not forward directed, as the bremsstrahlung, but achieves the maximum intensity of radiative gamma-ray quanta emission at an angle of 35 degrees with respect to the electron takeoff direction. It was this particularity of radiative neutron decay that we had realized in the methodology of this experiment, having placed the gamma detectors at 35 degrees to the electron detector. In this case, part of the statistics are lost, of course, but, as can be seen from [3] and Fig. 4, this is only a small fraction.

2. Experimental setup. The experimental setup is shown schematically in Fig. 1. The intense cold neutron beam passes through a rather long neutron guide in which is installed a collimation system made of LiF diaphragms placed at regular distances of 1 m. The neutrons enter the vacuum chamber (*1*) through the last diaphragm (*10*), which is located directly before the decay zone. This zone is observed by three types of detector: the microchannel-plate (MCP) proton detector (*3*), the electron detector (*14*) consisting of a 7-cm-diameter and 3-mm-thick plastic scintillator, and six gamma detectors (*12*) that are located on a ring centered around the electron detector and which consist of photomultiplier tubes each covered with a layer of CsI(Tl) scintillator. The thickness of these 7-cm-diameter CsI(Tl) scintillators is 4 mm and has been selected so as to have a 100% detection efficiency for photons with energies up to 100 keV. The six gamma detectors surround the electron detector (see [3]) at an angle of 35° and are shielded from it by 6 mm of lead (*13*).

By requiring a coincidence between the electron detector and any of the gamma detectors, the bremsstrahlung background can in principle be overcome completely, because bremsstrahlung emission occurs only in the section that registers the electron. In this case, part of the statistics are lost, of course, as can be seen from [3] and Fig. 4. However, the neutron-beam intensity of 10^{12} n/s in our experimental chamber is sufficiently high to still allow for a good count rate. Recoil protons, formed in the decay zone, pass through a cylindrical time-of-flight electrode (*7*) in the direction of the proton detector (*3*) and are focused onto this detector with the help of spherical focusing electrodes (*2*). The focusing electrostatic field between the high-voltage spherical and cylindrical electrodes (*2*) and (*7*) is created by the grids (*5*) and (*6*) at one side and by the proton detector grid (*4*), at ground potential, at the other side. It is important to note that the recoil protons take off isotropically from the decay point. In order not to lose half of the protons emitted, an additional grid (*11*) is added on the other side of the decay volume. The potential difference between the grid (*11*) and the grids and electrodes at the other side of the decay volume in principle assure a 4π solid-angle coverage for the recoil protons. At present this 4π solid angle coverage is not realized due to the presence of the plastic collimator (*8*) with a hole of diameter 70 mm, i.e., the diameter of the decay zone, on the side of the proton detector. For future measurements, this collimator will therefore be

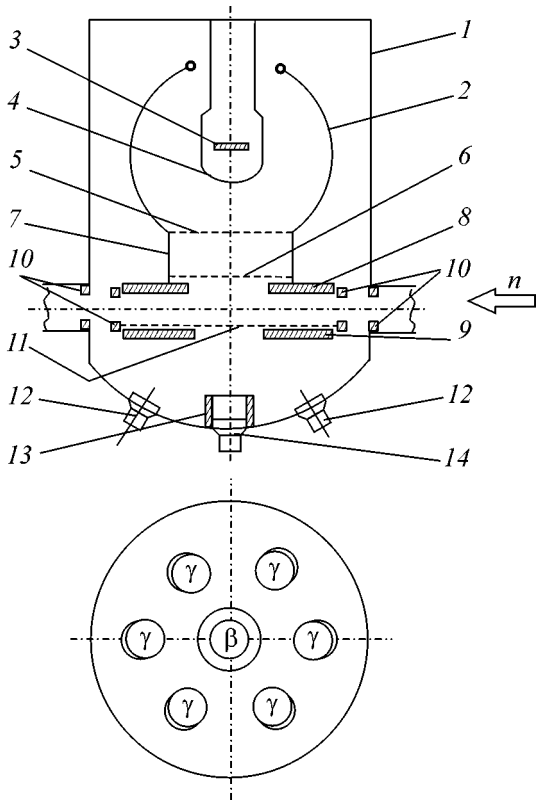

Fig. 1. Schematic layout of the experimental setup: (*1*) vacuum chamber, (*2*) spherical electrodes to focus the recoil protons on the detector (at 13–20 kV), (*3*) proton detector, (*4*) grid for proton detector (at ground potential), (*5*) and (*6*) grids for time-of-flight electrode, (*7*) time-of-flight electrode (at 13–20 kV), (*8*) plastic collimator (5 mm thick, diameter 70 mm) for recoil protons, (*9*) plastic collimator (5-mm-thick, diameter 70 mm) for beta electrons, (*10*) LiF diafragms, (*11*) grid to turn the recoil proton backward (at 22–26 kV), (*12*) six photomultiplier tubes for the CsI(Tl) gamma detectors, (*13*) lead cup, and (*14*) photomultiplier tube for the plastic scintillator electron detector.

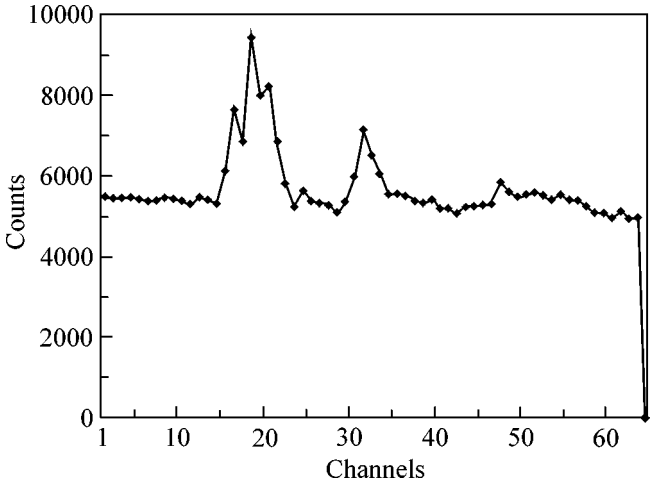

Fig. 2. Timing spectrum for *e–p* coincidences. Each channel corresponds to 25 ns. The peak at channel 17 corresponds to the prompt (momentary) coincidences. The coincidences between the decay electrons and delayed recoil protons (*e–p* coincidences) are contained in the large peak centered at channel 30.

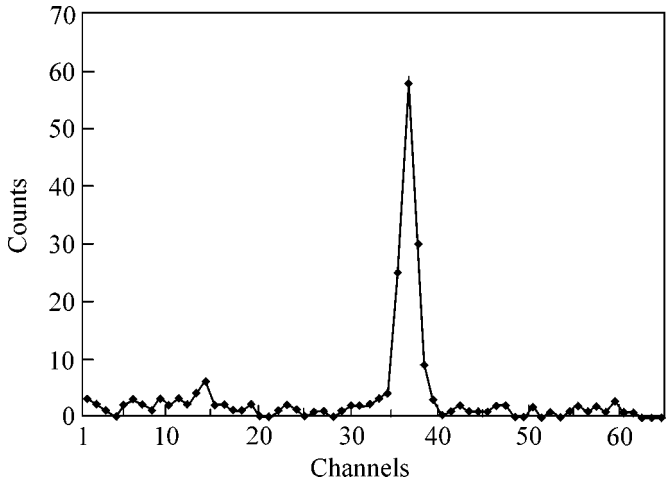

Fig. 3. Timing spectrum for triple *e–p–g* coincidences (peak centered at channel 35). Each channel corresponds to 25 ns.

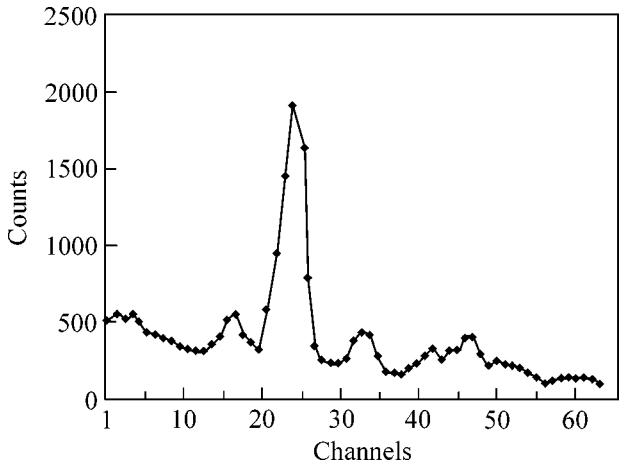

Fig. 4. Timing spectrum for *e–p* coincidences. Each channel corresponds to 25 ns. The peak at channel 17 corresponds to the prompt coincidences. The coincidences between the decay electrons and delayed recoil protons (*e–p* coincidences) are contained in the large peak centered at channel 24.

removed, which will increase the proton count rate by about a factor 50.

The start signal that opens the time windows for all detectors is the signal from the electron, registered in the electron detector. For an event to be considered as a radiative neutron-decay event simultaneous signals from the electron detector and one of the gamma detectors, followed by a delayed signal from the proton detector, are required. Besides these triple coincidences, electron–proton coincidences, signaling a neutron decay event also are monitored.

It is important to note here that, thanks to the LiF ceramics diaphragm system which was installed in the neutron beam line, the gamma background from the intense cold neutron beam was significantly suppressed. The background level in the gamma detector amounted to only about 100 Hz (at a neutron-beam intensity of 10^{12} n/s). If the number of the diaphragms in the neutron guide were doubled, the background of the gamma detectors could be further reduced by another order of magnitude, thus becoming comparable to the noise of the photomultiplier tubes. The count rate in the electron detector was just about 100 Hz. It is very likely that most of this count rate is due to electrons from neutron decay, since the count rate in this detector almost immediately dropped to zero when the neutron beam was switched off. The main problem in this experiment was the proton detector background, which turned out to be very sensitive to the vacuum conditions in the experimental chamber. This is discussed in detail in the next section.

3. Results. The experiment itself could be divided into two stages. At the beginning of statistics collection, we immediately discovered a peak of triple coincidences; however, the ratio of the triple electron–proton–gamma (*e–p–g*) coincidences to the number of double electron–proton (*e–p*) coincidences was about 5×10^{-2}, which exceeds the theoretical value by more than one order of magnitude. At the same time, at the beginning of the experiment, we had a rather poor vacuum and we consitantly registered a very high ion background in our proton detector. These results at the beginning of our experiment are best demonstrated in the time spectra given in Figs. 2 and 3.

Spectra of double *e–p* coincidences are given at the Fig. 2, and triple *e–p–g* coincidences are given at the Fig. 3. Two peaks can be clearly seen on Fig. 2: the so-called peak of false or momentary coincidences, which occurs when the proton detector registers backward-scattered bremstrahlung gamma-ray quanta (see Fig. 2), caused when the electron gets into the electron detector, this peak (in the 15 channel area) corresponds to the physical zero of recoil-proton delay time countdown. The recoil protons, in turn, form the second peak (from channels 30 to 40) of electron coincidences with time-delayed recoil proton (peak of *e–p* coincidences). A rather significant ion background can be seen here as well. In Fig. 3, one can clearly see a peak of triple coincidences of electron, gamma-ray quanta and delayed recoil proton (from channels 30 to 40, which corresponds to the position of the proton peak at the Fig. 2, we artificially shifted this peak under the peak of *e–p* coincidences; of course, this peak really corresponds to the position of the momentary coincidence peak). The numerical analysis of the spectra, shown in Figs. 2 and 3, gave a BR limit at the level of 5×10^{-2}, which exceeds the theoretical value more than one order. The results obtained at the first stage of the experiment, when on one hand we saw this large BR value with a very high ion background and on the other hand we had poor vacuum, forced us to analyze the situation in more detail.

The analysis showed that our vacuum chamber was filled with vapors of used oil from our old oil pumping system, installed on the vacuum chamber. We decided to replace this system, after which vacuum in the chamber improved, reaching the value of 7×10^{-5} mbar. After that we started collecting statistics again and found that it took much longer than the first time to obtain the peak of triple coincidences and that the ion background in the proton detector fell by almost two orders of magnitude.

The results obtained in the remaining beam time, with a vacuum of about 7×10^{-5} mbar, are presented in Figs. 4 and 5. Figure 4 shows the electron–proton coincidence timing spectrum, while the corresponding triple electron–proton–gamma coincidence timing spectrum is shown in Fig. 5. The first peak in Fig. 4, centered at channel 16, contains the prompt coincidences between backward-scattered bremsstrahlung gamma-ray quanta that are generated by electrons penetrating into the electron detector and are registered by the proton detector. The central position of this peak corresponds to $t = 0$ for the detection of the delayed recoil protons. The second peak (centered at about channel 24) contains the coincidences between electrons and recoil protons (*e–p* coincidence peak). The distance between the momentary coincidence peak and the *e–p* coincidence peak in Fig. 4 is less than the distance between these two peaks in Fig. 2 due to an increase of high voltage in the electrodes (a sharp fall of the ion background allowed to increase the high voltage in the electrodes). A comparison of these two figures also shows that when the vacuum improved, the value of the momentary coincidences peak declined sharply. The smaller secondary peaks on the right-hand side of the main peak in Fig. 4 are most probably connected with a small number of those recoil protons that, after being reflected from plastics (*8*) and (*9*) in Fig. 1, did get into the hole of plastic (*8*) and were registered by the proton detector (*3*). From the data presented in Figs. 4 and 5, an upper limit for the branching ratio for radiative neutron decay in the energy region from 35 keV to 100 keV could be deduced. For this, it is important to note that the radiative photons are emitted anisotropically [2]. The triple coincidence count rate N_T can be expressed as

$$N_T = \frac{N_D}{\varepsilon_e \Omega_e \varepsilon_p \Omega_p} \varepsilon_e \Omega_e \varepsilon_p \Omega_p \varepsilon_\gamma \Omega_\gamma f \mathrm{BR}, \qquad (1)$$

where N_D is the *e–p* coincidence count rate and ε_i and Ω_i ($i = e, p, \gamma$) are, respectively, the efficiencies and the solid angles for the electron detector, the proton detector, and the six gamma detectors. Further, the product $\Omega_\gamma f$ stands for the integral of the normalized photon-distribution function f (which reaches a maximum at 35° [3]) over the stereometric angle of the six gamma detectors and BR is the branching ratio of the radiative decay mode for the observed energy region. Adopting the procedure suggested by the Particle Data Group [6] to deduce upper limits for Poisson processes when only a small number of events is observed, Eq. (1) changes to

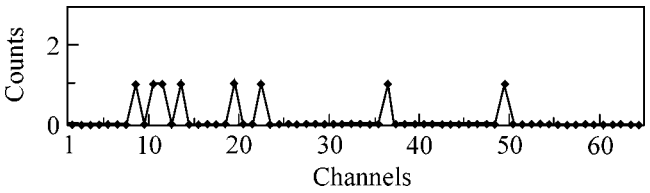

Fig. 5. Timing spectrum for triple *e–p–g* coincidences. Each channel corresponds to 25 ns.

$$\mathrm{BR} \le k \frac{N_T}{N_D} (\varepsilon_\gamma \Omega_\gamma f)^{-1}, \qquad (2)$$

where the factor k stands for the upper limit for the number of radiative-decay events when n_0 events are observed. Note that this result is independent of the efficiency or solid angle of both the electron and the proton detectors. For a calculated expected number of background counts of about 1.5 in the region where the triple coincidence peak is expected, and with $n_0 \equiv N_T = 1$ event observed in this region, the procedure described in [5] yields $k = 3.11$ at 90% C.L. With the number of observed *e–p* coincidences $N_D = 5382$, $\varepsilon_\gamma = 1$ and $\Omega_\gamma f \ge 0.084$, one then deduces an upper limit of 6.9×10^{-3} (90% C.L.) for the branching ratio of radiative neutron decay in the energy region from 35 to 100 keV.

It is interesting to note here that the maximum *e–p* coincidence rate reached during the experiment amounted to several events per minute. However, estimates show that this rate could be increased by about two orders of magnitude, corresponding to about 10–20 *e–p* coincidences per second. The main reason for the low count rate during the experiment was the very low efficiency of the MCP proton detector, even after the vacuum problem was solved, caused by the oil vapor which could not be removed from the detector during the beam time.

4. Conclusion. Results from the first experiment aiming to observe the as yet undiscovered radiative decay mode of the free neutron are reported. Although the experiment could not be performed under ideal conditions, the data still allowed one to deduce an upper limit of 6.9×10^{-3} (90% C.L.) for the branching ratio of radiative neutron decay in the energy region between 35 and 100 keV. This value has the same order of magnitude as the theoretical prediction based on the standard model of weak interactions [2].

Taking into account the fact that the experimental conditions can still be significantly optimized, an *e–p* coincidence count rate of 10–20 events per second is within reach. Together with the standard model prediction for the branching ratio of this decay mode, this would correspond to a triple *e–p–*γ coincidence rate of several events per 100 seconds. This can easily be observed with the current experimental setup, which is

now being optimized with a view to performing such an experiment. The aim of that experiment will then be, not only to establish the existence of radiative neutron beta decay, but also to study the radiative gamma spectrum in more detail.

We thank Profs. D. Dubbers, J. Deutsch, V.A. Nazarenko, Drs. V.V. Nesvizhevskii, A. Petukhov, and T. Soldner for valuable remarks and discussions. We are also grateful to the administration of the ILL, especially Dr. Christian Vettier and scientific coordinator Giovanna Cicognani for organizing our work. This work was supported by INTAS (project no. 1-A-115; Open 2000), the Russian Foundation for Basic Research (project no. 00-02-17383), and the Flemish Fund for Scientific Research (F.W.O.).

REFERENCES

1. Particle Data Group (K. Hagiwara, K. Hikasa, K. Nakamura, *et al.*), Phys. Rev. D **66**, VIII.8 (2002).
2. Yu. V. Gaponov and R. U. Khafizov, Phys. Lett. B **379**, 7 (1996).
3. R. U. Khafizov and N. Severijns, in *Proceedings of the International Symposium on the Interactions of Neutrons and Nuclei (ISINN-8), Dubna, 2000*, p. 185.
4. B. G. Yerozolimsky, Yu. A. Mostovoi, V. P. Fedunin, *et al.*, Yad. Fiz. **28**, 98 (1978) [Sov. J. Nucl. Phys. **28**, 48 (1978)].
5. I. A. Kuznetsov, A. P. Serebrov, I. V. Stepanenko, *et al.*, Phys. Rev. Lett. **75**, 794 (1995).
6. Particle Data Group (G. P. Yost, R. Michael Barnet, I. Hichliffe, *et al.*), Phys. Lett. B **204**, 81 (1988).

JETP Letters, Vol. 76, No. 6, 2002, pp. 337–340. Translated from Pis'ma v Zhurnal Éksperimental'noĭ i Teoreticheskoĭ Fiziki, Vol. 76, No. 6, 2002, pp. 397–400.

Coherent Diffraction Radiation of a 6-MeV Microtron Electron Beam

A. N. Aleinik*, A. S. Aryshev*, B. N. Kalinin*, G. A. Naumenko*, [1], A. P. Potylitsyn*, G. A. Saruev*, A. F. Sharafutdinov*, O. Yu. Malakhovskii, and E. A. Monastyrev****

** Research Institute of Nuclear Physics, Tomsk Polytechnical University, Tomsk, 634050 Russia*

[1] *e-mail: naumenko@npi.tpu.ru*

*** Research Institute of Semiconductor Devices, Tomsk, 634050 Russia*

Received August 19, 2002

PACS numbers: 41.75.Fr; 29.27.Fh; 41.60.-m

After the experiment [1] in which Shibata *et al.* observed coherent diffraction radiation (CDR) of a bunched electron beam from the KURRY accelerator (energy $E = 150$ MeV, mean current $\langle I \rangle = 10$ nA, bunch length $l = 1$ mm, and number of electrons in the bunch $N_e = 1.8 \times 10^8$), interest in this type of radiation has increased appreciably. This interest stems, first, from the possibility of producing an intense radiation source in the millimeter and submillimeter wavelength ranges and, second, from the possibility of nondisturbing determination of the electron-bunch length in electron–positron colliders and free-electron lasers when measuring the spectral composition of CDR [2–4]. However, as was noted in [5, 6], the standard single-particle model of diffraction radiation (DR) [7], which describes the DR parameters when a relativistic particle passes near a semi-infinite, perfectly conducting half-plane (see also [8] for a review), should be modified when the crosswise (in a direction perpendicular to the electron trajectory) target dimension a is commensurable with the characteristic parameter $\gamma\lambda/2\pi$ (γ is the particle Lorentz factor and λ is the radiation wavelength). Therefore, it is of considerable interest to compare estimates based on the theoretical model [7] with experimental data for a $a \leq \gamma\lambda/2\pi$.

We carried out an experiment on the generation of DR using a beam from the Tomsk microtron with the energy $E = 6.1$ MeV ($\gamma = 12$). Basic parameters of the microtron are given below:

Energy of accelerated electrons:	6.1 MeV
Macropulse duration:	2–6 μs
Macropulse frequency:	1–10 Hz
Current amplitude in macropulse:	40 mA
Micropulse duration:	17–20 ps
Micropulse length:	0.6 cm
Number of micropulses in macropulse:	10^4
Current amplitude in micropulse:	0.6 A
Mean microtron current:	2.4 μA
Beam nonmonochromacity:	0.5%
Beam dimensions at exit from microtron:	4×2 mm
Divergence:	
Horizontal	15×10^{-3} rad
Vertical	5×10^{-3} rad

The experimental setup is shown in Fig. 1. The detector of electromagnetic radiation was set at angle $\theta_D = 90°$ relative to the electron beam. The target was a $50 \times 50 \times 1$-mm^3 aluminum plate. It was placed in goniometer G, which measured the impact parameter h (the shortest distance between the target edge and the electron-beam axis) and the tilt angle ψ relative to the beam (see Fig. 1). A set of magnetic quadrupole lenses provided such a beam focusing in the horizontal and vertical directions that the beam at the place of its passage through the target had dimensions of the order of $\Delta_v \times \Delta_h = 4 \times 1$ mm. They were measured using a luminescent screen and a wire scanner. The beam current was measured by an inductive current sensor.

To test the optical system and to estimate the electron-beam divergence, we measured the orientation dependence of the optical transient radiation yield. In these measurements, the detector was a photomultiplier FEU-110 (with the photocathode sensitivity range $\lambda = 350$–850 nm). The derived dependence is well described by theory for the beam divergence $\Delta\theta = 3.5$ mrad [9]; the symmetry center of the measured distribution corresponds to $\psi = 45° \pm 1.5° = \theta_D/2$, which confirms that the chosen experimental setup is operational.

0021-3640/02/7606-0337$22.00

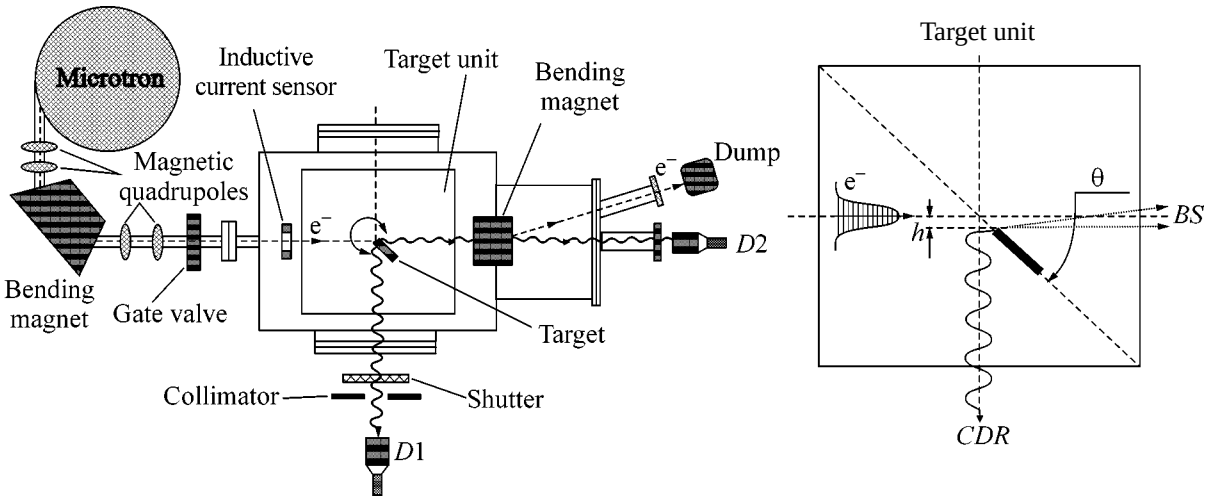

Fig. 1. The experimental setup.

A detector based on a broadband antenna of diameter ϕ = 15 mm with an output signal preamplifier was used to record the CDR pulse. The detector parameters were investigated with a millimeter oscillator on a special bench. The detector sensitivity band was λ = 1–25 mm. The detector response linearity was checked by varying the distance R between the oscillator and the detector. The derived decreasing quadratic dependence of the signal Y confirms that the detector operates in a linear mode.

Figure 2 shows a plot of the measured CDR yield against the mean accelerated-electron current in a macropulse (i.e., against a quantity proportional to the number of electrons in the bunch). The accelerated current was varied over the range I = 5–30 mA. As follows from the figure, we observed a quadratic dependence of the CDR yield on current I. Fitting the measured dependence by the function $Y = kI^B$ yielded the exponent $B = 2.28 \pm 0.08$. This confirms that CDR was recorded in the following geometry: the target tilt angle $\psi = 45 \pm 1.5° = \theta_D/2$, the impact parameter h = 7 mm, and the electron-beam dimensions $\Delta = 4 \times 1.5$ mm.

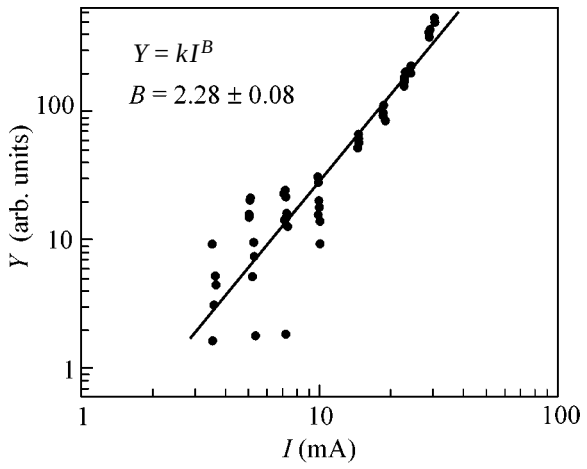

Fig. 2. CDR yield versus mean microtron current (the dots represent the experimental data and the solid line represents the fit $Y = kI^B$).

In our experiment, we also measured the dependence of the CDR yield on impact parameter for a parallel passage of the electron beam by the target. In this geometry, the "physical zero" of the impact parameter (i.e., the coincidence of the electron-beam axis with the target) can be easily determined with a high accuracy. In addition, the crosswise target dimension in this case is much smaller than the parameter $\gamma\lambda/2\pi$.

This dependence can be described by using a simple CDR model for the Gaussian charge-density distribution in an electron bunch with variance σ_z [1, 2]:

$$Y_B(h) = N_e^2 \int_{\Delta\Omega} d\Omega \int_0^\infty d\omega \frac{d^2W_0(\theta_x, \theta_y, \omega, h)}{d\omega d\Omega} \times \exp\left(-\frac{\sigma_z^2\omega^2}{c^2}\right)\varepsilon(\omega). \quad (1)$$

Here, $Y_B(h)$ is the CDR yield of a single bunch with the number of electrons N_e, $d^2W_0(\theta_x, \theta_y, \omega, h)/d\omega d\Omega$ is the spectral angular intensity of DR from a single electron, $\exp(-\sigma_z^2\omega^2/c^2)$ is the square of the modulus of the Fourier transform of the longitudinal electron distribution in the bunch (the square of the modulus of the longitudinal formfactor), and $\varepsilon(\omega)$ is the transfer function of the detector [10].

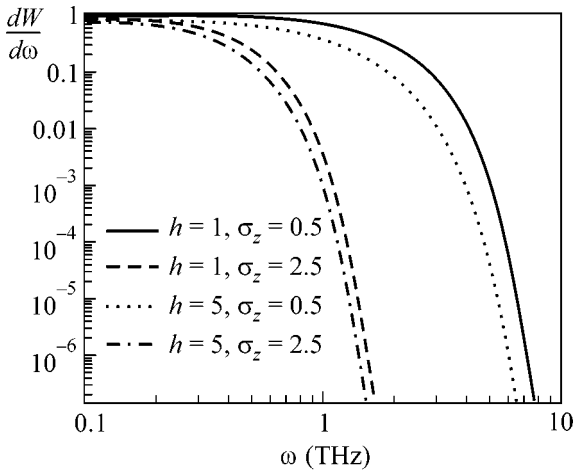

Fig. 3. CDR spectra for various bunch lengths at various impact parameters.

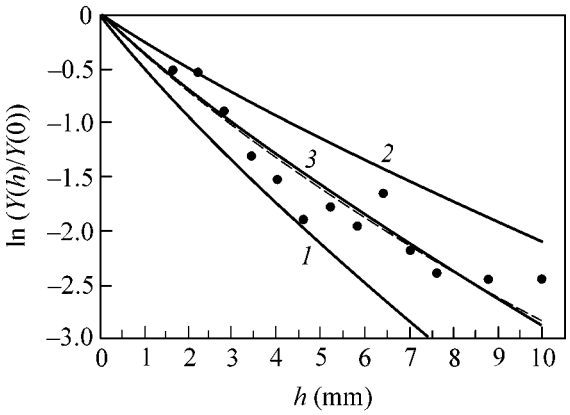

Fig. 4. The logarithm of CDR yield versus impact parameter for a parallel passage of the electron beam by the target. The dots represent the experimental data and the dashed line represents a nonparametric fit to the experimental data. Curves *1*, *2*, and *3* are the computed dependences for L = 1, 2, and 1.4 mm, respectively.

Below, we use the following simple transfer function:

$$\varepsilon(\omega) = \begin{cases} \text{const} & \omega_{\min} \le \omega \le \omega_{\max} \\ 0 & \omega < \omega_{\min}, \quad \omega > \omega_{\max}. \end{cases} \tag{2}$$

In this approximation, instead of (1), we have

$$Y_B(h) = \text{const} N_e^2 \int_{\omega_{\min}}^{\omega_{\max}} d\omega \frac{(dW_0)(0, \pi/2, \omega, h)}{d\omega} \times \exp\left(-\frac{\sigma_z^2 \omega^2}{c^2}\right). \tag{3}$$

The integration limits are $\omega_{\min}$ = 0.094 THz ($\lambda_{\max}$ = 20 mm) and $\omega_{\max} = \frac{2\pi}{\lambda_{\min}} c$ = 1.88 THz. In our experiment, we used a detector with a small angular aperture $\Delta\Omega \ll \gamma^{-1}$. Therefore, the frequency spectrum of the DR intensity for a single electron as it passes parallel to the half-plane, $\frac{d^2 W_0}{d\omega d\Omega}$, has a simple form [11],

$$\frac{dW_0(0, \pi/2, \omega, h)}{d\omega} \approx \frac{\alpha}{2\pi^2} \exp\left(-\frac{4\pi h}{\gamma\lambda}\right). \tag{4}$$

Since the lengthwise target dimension significantly exceeds the maximum radiation wavelength, formula (4) can be used by disregarding interference from the target edges. Figure 3 shows the CDR spectra for various bunch lengths at various impact parameters.

Since $S(h) = \ln(Y(h)/Y(0))$ does not depend on the absolute value of the radiation intensity, we can easily compare it with the experimental result. At the same time, $S(h)$ depends on the electron-bunch length. Thus, by fitting $S(h)$ in bunch length L ($L = 4.58\sigma_z$ is the bunch length at the 10% level for a Gaussian electron distribution in the bunch) to its experimental dependence, we can estimate L. Figure 4 shows the results of this procedure (curve *3* for L = 1.4 mm) and, for comparison, $S(h)$ for L = 1 mm (curve *1*) and L = 2 mm (curve *2*). The value of $Y(0)$ for the experimental data was taken by the extrapolation of their nonparametric fit.

In conclusion, we note the following:

(1) Coherent diffraction radiation whose intensity is proportional to the square of the number of electrons in the bunch was recorded from a bunched microtron electron beam with energy E = 6.1 MeV and with the number of electrons in the bunch $N_e = 10^8$.

(2) When a broadband detector is used, the electron-bunch length can be measured from the dependence of the CDR yield on impact parameter without resorting to cumbersome spectral measurements.

This study was supported by the Ministry of Education of Russia (project no. 226 “The Development of Intense Positron Sources and Beam Diagnostic Facilities for Modern Colliders” of the Program “State Support for Regional Scientific and Technical Policy of the Higher School and the Development of its Scientific Potential”).

REFERENCES

1. Y. Shibata, Sh. Hasebe, *et al.*, Phys. Rev. E **52**, 6787 (1995).

2. A. H. Lumpkin, N. S. Sereno, *et al.*, in *Proceedings of the 9th Beam Instrumentation Workshop, Cambridge, 2000*, AIP Conf. Proc., Vol. 546.
3. M. Castellano, V. A. Verzilov, *et al.*, Phys. Rev. E **63**, 056501 (2001).
4. B. Feng, M. Oyamada, *et al.*, Nucl. Instrum. Methods Phys. Res. A **475**, 492 (2001).
5. A. P. Potylitsyn, Nucl. Instrum. Methods Phys. Res. B **145**, 169 (1998).
6. A. P. Potylitsyn, Phys. Rev. E **60**, 2272 (1999).
7. A. P. Kazantsev and G. I. Surdutovich, Dokl. Akad. Nauk SSSR **147** (1), 74 (1962) [Sov. Phys. Dokl. **7**, 990 (1963)].
8. B. M. Bolotovskiĭ and E. A. Galst'yan, Usp. Fiz. Nauk **170**, 8 (2001).
9. A. N. Aleĭnik, O. V. Chefonov, B. N. Kalinin, *et al.*, Nucl. Instrum. Methods Phys. Res. B (in press).
10. L. N. Kurbatov, *Optoelectronics of Visible and Infrared Regions of Spectrum* (Mosk. Fiz.-Tekh. Inst., Moscow, 1999).
11. A. P. Potylitsyn, Izv. Vyssh. Uchebn. Zaved., Fiz., No. 3, 93 (2001).

Translated by V. Astakhov

JETP Letters, Vol. 76, No. 6, 2002, pp. 341–345. Translated from Pis'ma v Zhurnal Éksperimental'noĭ i Teoreticheskoĭ Fiziki, Vol. 76, No. 6, 2002, pp. 401–405.

Waveguide Modes of Hollow Photonic-Crystal Fibers

S. O. Konorov*, A. B. Fedotov*, **, O. A. Kolevatova*, V. I. Beloglazov*, N. B. Skibina***, A. V. Shcherbakov***, and A. M. Zheltikov*, ****

** Physics Faculty, Moscow State University, Vorob'evy gory, Moscow, 119899 Russia*
e-mail: zheltikov@top.phys.msu.su
*** International Laser Center, Moscow State University, Vorob'evy gory, Moscow, 119899 Russia*
**** Technology and Equipment for Glass Structures Institute, pr. Stroitelei 1, Saratov, 410044 Russia*
Received August 19, 2002

Waveguide modes of microstructure fibers with a hollow core and a two-dimensionally periodic cladding are studied experimentally and theoretically. The spectrum of modes guided in the hollow core of these fibers displays isolated maxima, indicating that waveguiding is supported due to the high reflectivity of the fiber cladding within photonic band gaps. The main properties of the spectrum of modes guided in a hollow core of a photonic-crystal fiber and radiation intensity distribution in these modes are qualitatively explained in terms of the model of a periodic coaxial waveguide. © *2002 MAIK "Nauka/Interperiodica".*

PACS numbers: 42.81.Qb; 42.65.Wi; 42.70.Qs

Fiber with a two-dimensionally periodic microstructure (two-dimensional photonic crystal) and a hollow core is one of the most interesting and promising types of microstructure fibers [1–4]. Such fibers were demonstrated for the first time by Cregan *et al.* [5]. The photonic band gap in the transmission spectrum of a two-dimensional periodic cladding in these fibers provides high reflection coefficients for electromagnetic radiation propagating along the hollow core of the fiber, allowing a specific regime of waveguiding to be implemented. This mechanism of waveguiding is of special interest for telecommunication applications and opens, at the same time, possibilities to enhance nonlinear-optical processes, including high-order harmonic generation, in a gas medium filling the fiber core [6]. The possibility of using such fibers for laser manipulation of small particles was recently demonstrated by Benabid *et al.* [7].

In spite of many potential exciting applications of hollow-core photonic-crystal fibers in telecommunication technologies, high-power laser physics, and nonlinear optics, only a few experiments have been performed with such fibers. This is largely due to the difficulties one encounters when fabricating hollow photonic-crystal fibers. In this paper, we present the results of our experimental and theoretical investigations of glass fibers with a hollow core and a two-dimensionally periodic cladding. Such fibers may guide electromagnetic radiation due to the high reflectivity of the cladding within photonic band gaps, holding much promise for telecommunication applications, high-power laser radiation guiding, laser manipulation and laser guiding of atoms and charged particles, high-order harmonic generation, and transport of ultrashort laser pulses. We will demonstrate that the main properties of the spectrum of modes guided in the hollow core of photonic-crystal fibers can be qualitatively explained within the framework of the model of a periodic coaxial waveguide.

Microstructure fibers were fabricated with the use of a preform consisting of a set of identical glass capillaries. Seven capillaries were removed from the central part of the preform for the hollow core of photonic-crystal fibers. The cross-section image of a fiber fabricated by drawing such a preform is presented in Fig. 1. A typical period of the structure in the cladding of the fiber shown in Fig. 1 is about 5 μm. The diameter of the hollow core of the fiber is then approximately equal to 13 μm. The length of fiber samples employed in our experiments ranged from several centimeters up to 1 m.

The idea of lowering the magnitude of optical losses in a hollow fiber with a periodically microstructured cladding relative to the magnitude of optical losses in a hollow fiber with a solid cladding is based on the high reflectivity of a periodic structure within photonic band gaps [8]. In hollow fibers, the refractive index of the core is lower than the refractive index of the cladding. Therefore, the propagation constants of hollow-fiber modes have nonzero imaginary parts, and the propagation of light in such fibers is accompanied by radiation losses. The coefficient of optical losses in hollow fibers scales [9] as λ^2/a^3, where λ is the radiation wavelength and a is the inner radius of the fiber. This behavior of the magnitude of optical losses prevents one from using hollow fibers with very small inner diameters in nonlinear-optical experiments [10]. Our estimates show that the magnitude of radiation losses for the fundamental mode of a hollow fiber with a fused silica cladding and an inner radius of 6.5 μm may reach 20 cm^{-1} for 0.8-μm

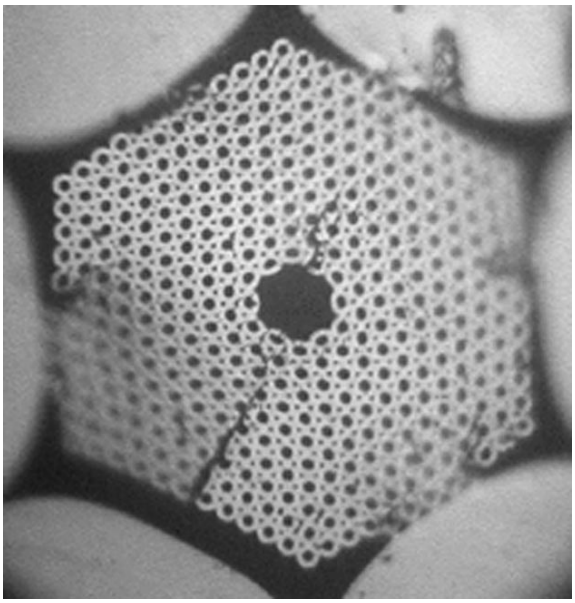

Fig. 1. Cross-sectional image of a microstructure fiber with a two-dimensionally periodic cladding consisting of an array of identical capillaries. This periodic cladding supports guided modes in the hollow core of the fiber due to the high reflectivity of a periodic structure within photonic band gaps. The hollow core of the fiber is formed by removing seven capillaries from the central part of the structure. The period of the structure in the cladding is about 5 μm and the core diameter is about 13 μm.

radiation, which, of course, imposes serious limitations on the applications of such fibers. Radiation losses can be radically reduced in the case of hollow fibers with a periodic cladding.

Our experimental studies confirm the possibility of using hollow photonic-crystal fibers with a core diameter of about 13 μm to guide coherent and incoherent radiation. Figure 2 displays the spatial distributions of intensity of incoherent (Fig. 2a) and coherent (Fig. 2b) radiation obtained by imaging the output end of a hollow photonic-crystal fiber with the above-specified parameters. Optimizing the geometry of coupling of laser radiation into the fiber, we were able to achieve a high degree of light-field confinement in the hollow core of the fiber without losing too much energy through mode excitation in the photonic-crystal cladding (Fig. 2a). The spatial distribution of radiation intensity at the output end of the fiber under these conditions corresponded to the fundamental waveguide mode.

To investigate the spectrum of modes guided in the hollow core of photonic-crystal fibers, we used a diaphragm to separate radiation transmitted through the hollow core from radiation guided by the cladding. The spectra of modes supported by the hollow core of photonic-crystal fibers were measured within the range of wavelengths from 450 up to 1000 nm. These spectra

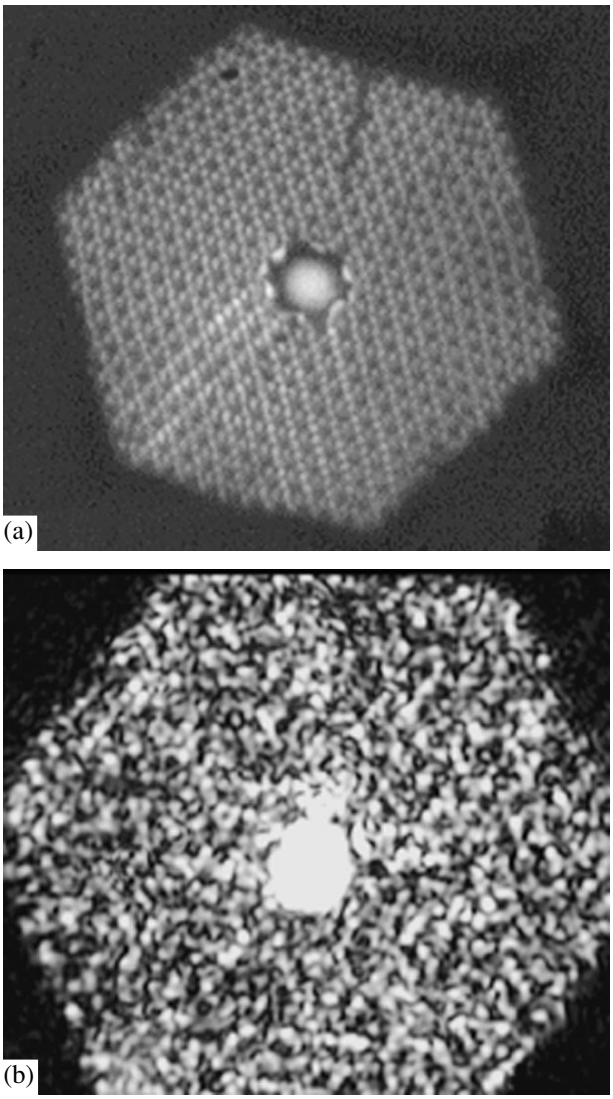

Fig. 2. Radiation intensity distribution in the cross section of a hollow photonic-crystal fiber with a period of the structure in the cladding of about 5 μm and the core diameter of approximately 13 μm. (a) A waveguide mode is excited in the hollow core with a broad beam of incoherent light. (b) The fundamental waveguide mode of the hollow core is excited with 633-nm diode-laser radiation.

displayed characteristic well-pronounced isolated peaks (Fig. 3a). Similar peaks in transmission spectra of hollow photonic-crystal fibers have been observed earlier by Cregan *et al.* [5]. The origin of these peaks is associated with the high reflectivity of a periodically structured fiber cladding within photonic band gaps, which substantially reduces radiation losses in guided modes within narrow spectral ranges. Radiation with wavelengths lying away from photonic band gaps of the cladding leaks from the hollow core. Such leaky radiation modes are characterized by high losses, giving virtually no contribution to the signal at the output of the fiber.

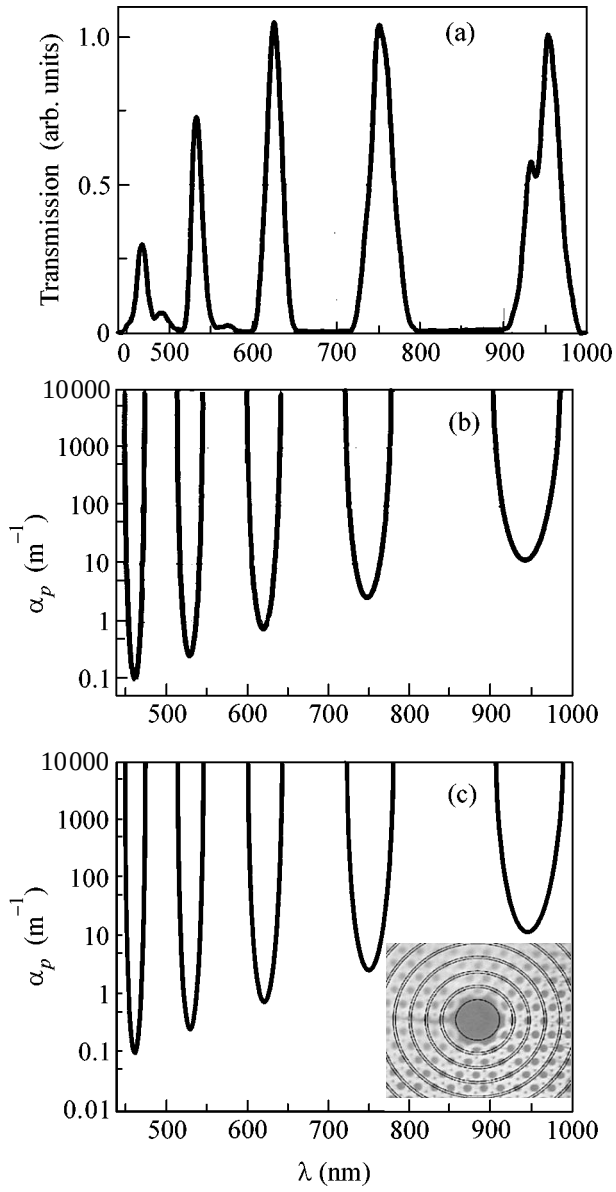

Fig. 3. (a) The spectrum of modes measured for a hollow photonic-crystal fiber with a period of the structure in the cladding of about 5 μm and the core diameter of approximately 13 μm. (b) The attenuation coefficient of the TE_{01} waveguide mode calculated as a function of the wavelength for a periodic coaxial waveguide (see the inset) with r_0 = 6.5 μm, b = 4.3 μm, and c = 0.7 μm.

To model the spectrum of guided modes and the spatial distribution of radiation intensity in a hollow photonic-crystal fiber, we employed the model of a periodic coaxial waveguide. A two-dimensional periodic structure of the fiber cladding is replaced within the framework of this model by a system of coaxial glass cylinders (see the inset in Fig. 3c) with a thickness $b \approx$ 4.3 μm and the inner radius of the ith cylinder equal to $r_i = r_0 + i(b + c)$, where r_0 is the radius of the hollow core (about 6.5 μm for our fiber) and c is the thickness

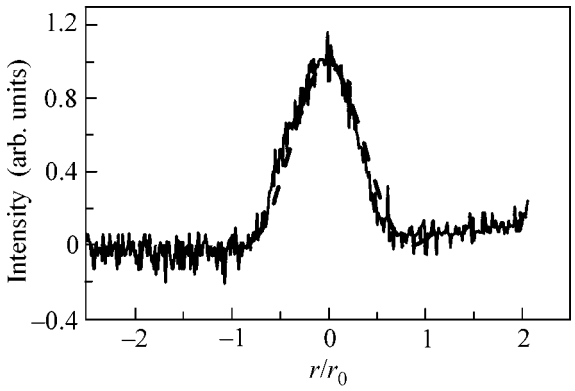

Fig. 4. Transverse intensity distribution of electromagnetic radiation (solid line) measured at the output of a hollow-core photonic-crystal fiber and (dashed line) calculated with the use of the model of a periodic coaxial waveguide.

of the air gap between the cylinders. The latter parameter was chosen in such a way as to include the air-filling fraction of the fiber cladding (about 14% in our experiments) and was set equal to approximately 0.7 μm for our calculations. In our theoretical analysis, we employed the results of earlier work [11, 12] devoted to the properties of modes in coaxial waveguides.

Figure 3b presents the attenuation coefficient for the TE_{01} mode calculated as a function of the wavelength for a periodic coaxial waveguide with the above-specified parameters. Comparing these results with the experimental data shown in Fig. 3a, we find that the model of a periodic coaxial waveguide provides qualitatively adequate predictions for the positions and the widths of spectral bands where the hollow core of a photonic-crystal fiber can guide radiation with virtually no losses. The model of a periodic coaxial waveguide, as can be seen from Figs. 4 and 5, also gives a satisfactory qualitative description for radiation-intensity distributions in the fundamental (Fig. 4) and higher order (Fig. 5) waveguide modes of a photonic-crystal fiber. Our theoretical results are consistent on a qualitative level with the predictions of simulations [13] performed with the use of a more accurate and more sophisticated model of a hollow-core photonic-crystal fiber.

The spatial distribution of 633-nm diode-laser radiation (this wavelength falls within one of the passbands in Fig. 3, corresponding to the guided modes of our fiber) at the output of an 8-cm hollow photonic-crystal fiber shown in Fig. 5b indicates the existence of multimode regimes of waveguiding around this wavelength. As shown in [6], multimode waveguiding regimes in hollow photonic-crystal fibers can be employed to enhance high-order harmonic generation in nonlinear gases filling the hollow core of photonic-crystal fibers. The waveguide contribution to the mismatch of propagation constants related to guided modes of the pump and harmonic radiation increases with a decrease in the

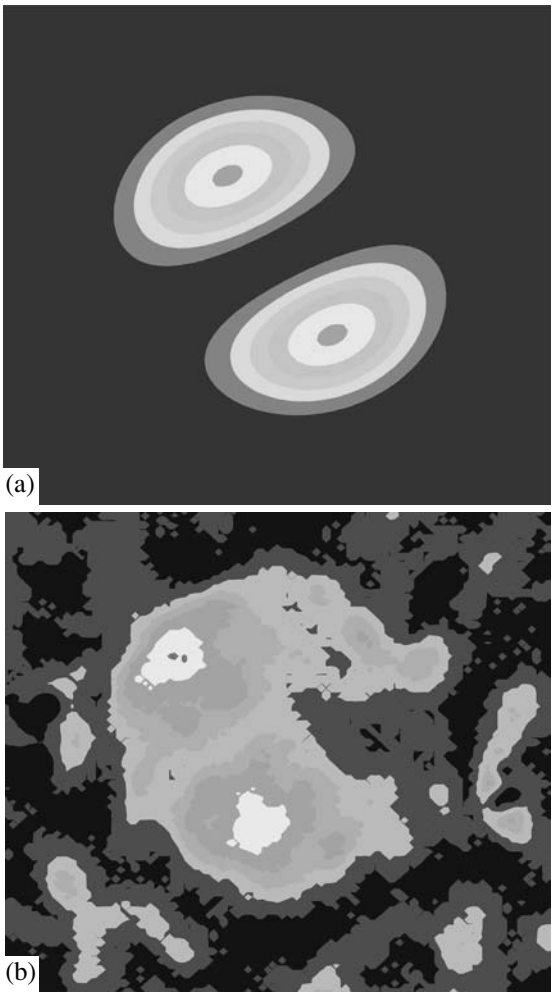

Fig. 5. (a) Transverse distribution of the electric field squared in a higher order mode of a hollow-core photonic-crystal fiber calculated with the use of the model of a periodic coaxial waveguide. (b) Transverse intensity distributions of electromagnetic radiation measured at the output of a hollow-core photonic-crystal fiber with a higher order waveguide mode of the fiber excited with 633-nm radiation of a diode laser.

core diameter of a hollow fiber [10]. Our photonic-crystal fiber with a small core diameter is, therefore, characterized by a strong dispersion of guided modes, allowing considerable phase mismatches related to the material dispersion of nonlinear gases to be compensated. This efficient phase-mismatch compensation becomes possible due to the unique properties of hollow photonic-crystal fibers, as the leaky modes guided in hollow fibers with a solid cladding and a diameter of the hollow core of about 13 μm would have, as mentioned above, unacceptably high losses.

Since hollow waveguides with a periodic cladding permit radiation losses characteristic of hollow-waveguide modes to be radically reduced, waveguides of this type seem to offer new solutions in guiding high-power laser radiation and enhancing nonlinear-optical processes, including self- and cross-phase modulation, as well as optical harmonic generation and wave mixing. The results of preliminary experiments and theoretical studies [14] suggest that polycapillary glass structures and photonic-crystal fibers can guide and focus ultrashort x-ray pulses, including ultrashort field waveforms synthesized from high-order harmonics. Strong waveguide dispersion, inherent in hollow fibers with a small core radius, can be employed to compensate for the initial chirp and, eventually, to compress short x-ray pulses.

The fibers created and studied in this work can be used for the creation of high-sensitivity gas sensors based on linear and nonlinear spectroscopic techniques. Waveguiding regimes attainable with hollow photonic-crystal fibers with a small core diameter allow the amount of gas necessary for spectral analysis to be considerably reduced and permit nonlinear-spectroscopic studies to be performed with low-power laser pulses. In particular, experiments on four-wave mixing in hollow fibers (see, e.g., [15]) are usually carried out with capillaries with a typical inner diameter on the order of 100 μm (the use of capillaries with smaller inner diameters leads to the fast growth of optical losses). The fibers considered in this paper would allow comparable levels of nonlinear signal to be achieved with laser pulses 60 times less powerful. The spectra of modes guided by these fibers seem optimal for laser frequency conversion through stimulated Raman scattering.

Thus, we have created and investigated fibers with a hollow core and a photonic-crystal cladding with a period of the structure in the cladding of about 5 μm and the core diameter of approximately 13 μm. Electromagnetic radiation is guided in the hollow core of such fibers due to the high reflectivity of the cladding within photonic band gaps. This regime of waveguiding allows optical losses of guided modes to be radically reduced as compared with waveguide modes in hollow fibers with a solid cladding. Due to their remarkable properties, hollow photonic-crystal fibers created and investigated in this work hold much promise for telecommunication applications and can be used to guide high-power laser pulses. These fibers offer a unique opportunity for implementing nonlinear-optical interactions of waveguide modes with transverse sizes of several microns in a gas medium, opening possibilities to improve the efficiency of optical frequency conversion for ultrashort pulses and enhance high-order harmonic generation. The fibers studied in this paper can be employed to produce and guide ultrashort pulses, to manipulate atoms and charged particles, and to develop highly sensitive gas sensors. We have shown that the main properties of the spectrum of modes guided in the hollow core of photonic-crystal fibers, as well as the radiation intensity distribution in the fiber core can be qualitatively explained within the framework of the model of a periodic coaxial waveguide.

This study was supported in part by the President of Russian Federation Grant no. 00-15-99304, the Russian Foundation for Basic Research (project nos. 00-02-17567 and 02-02-17098), the Volkswagen Foundation (project I/76 869), and ARL European Research Office (grant no. R&D 9375-AM-07).

REFERENCES

1. J. C. Knight, T. A. Birks, P. St. J. Russell, and D. M. Atkin, Opt. Lett. **21**, 1547 (1996).
2. Opt. Express **9** (13), Focus Issue (2001).
3. J. Opt. Soc. Am. B **19**, Special Issue (2002).
4. A. M. Zheltikov, Usp. Fiz. Nauk **170**, 1203 (2000).
5. R. F. Cregan, B. J. Mangan, J. C. Knight, *et al.*, Science **285**, 1537 (1999).
6. A. N. Naumov and A. M. Zheltikov, Laser Phys. **12**, 971 (2002).
7. F. Benabid, P. St. J. Russell, and J. C. Knight, in *Proceedings of the Conference on Lasers and Electro-Optics (CLEO'2002), Long Beach, 2002*, CMJ5.
8. A. Yariv and P. Yeh, *Optical Waves in Crystals: Propagation and Control of Laser Radiation* (Wiley, New York, 1984; Mir, Moscow, 1987).
9. E. A. J. Marcatili and R. A. Schmeltzer, Bell Syst. Tech. J. **43**, 1783 (1964).
10. A. M. Zheltikov, Usp. Fiz. Nauk **172**, 743 (2002).
11. T. Kawanishi and M. Izutsu, Opt. Express **7**, 10 (2000).
12. G. Ouyang, Yong Xu, and A. Yariv, Opt. Express **9**, 733 (2001).
13. J. Broeng, S. E. Barkou, T. Sondergaard, and A. Bjarklev, Opt. Lett. **25**, 96 (2000).
14. A. N. Naumov and A. M. Zheltikov, Laser Phys. **12** (11) (2002).
15. A. B. Fedotov, F. Giammanco, A. N. Naumov, *et al.*, Appl. Phys. B **72**, 575 (2001).

Translated by A. Zheltikov

JETP Letters, Vol. 76, No. 6, 2002, pp. 346–350. Translated from Pis'ma v Zhurnal Éksperimental'noĭ i Teoreticheskoĭ Fiziki, Vol. 76, No. 6, 2002, pp. 406–410.

Vortex Line Representation for Flows of Ideal and Viscous Fluids

E. A. Kuznetsov

Landau Institute for Theoretical Physics, Russian Academy of Sciences, Moscow, 119334 Russia
e-mail: kuznetso@itp.ac.ru

Received August 8, 2002

The Euler hydrodynamics describing the vortex flows of ideal fluids is shown to coincide with the equations of motion obtained for a charged compressible fluid moving under the effect of a self-consistent electromagnetic field. For the Euler equations, the passage to the Lagrange description in the new hydrodynamics is equivalent to a combined Lagrange–Euler description, i.e., to the vortex line representation [5]. Owing to the compressibility of the new hydrodynamics, the collapse of a vortex flow of an ideal fluid can be interpreted as a result of the breaking of vortex lines. The Navier–Stokes equation formulated in terms of the vortex line representation proves to be reduced to a diffusion-type equation for the Cauchy invariant with the diffusion tensor determined by the metric of this representation. © *2002 MAIK "Nauka/Interperiodica".*

PACS numbers: 47.15.Ki; 47.32.Cc

1. Collapse as a finite-time process of singularity formation from an initially smooth distribution plays a fundamental role in physics because it represents one of the most efficient mechanisms of energy dissipation. For incompressible fluid dynamics, the collapse must also be of great importance. It is well known that singularity formation in gas dynamics, i.e., in compressible fluid dynamics, is related to the phenomenon of breaking, which is the main factor of shock-wave formation. From the point of view of the classical theory of catastrophes [1], this process is nothing but folding. It is completely characterized by the mapping which describes the passage from the Euler representation to the Lagrange representation. The points where the Jacobian J of this mapping becomes zero correspond to the appearance of singularities in the derivatives of the gas velocity and density. In the case of an incompressible medium, the breaking is absent, because the Jacobian of the corresponding mapping is fixed (for the simplest gauge, it is equal to unity). Hence, at first glance, one can see no factors that can cause such phenomena in this case. However, our previous publications [2–4] demonstrated the possibility of breaking in an incompressible flow. This effect occurs for the vortex lines. Unlike the breaking in gas dynamics, where one Lagrangian trajectory crosses another Lagrangian trajectory, the vortex line breaking means that one vortex line overtakes another vortex line. For a smooth continuous distribution of vorticity, the breaking initially occurs when the vortex lines touch each other at a single point. At the point of contact, the vorticity becomes infinite. This is possible despite the incompressibility of the vector fields of vorticity and velocity of the fluid. To describe the breaking of vortex lines, a vortex-line representation of the latter on the basis of the combined Lagrange–Euler description was proposed in [5, 6]. In this representation, each vortex line was labeled by a two-dimensional Lagrangian marker while the other parameter defined the vortex line itself.

This paper develops this method in application to both ideal and viscous fluids. It reveals the role of the Clebsch variables, which can be used as the Lagrangian markers of the vortex lines. However, the Clebsch variables are suitable only for a local description. In a general situation, the passage to the vortex-line representation in the Euler equation is equivalent to the consideration of new hydrodynamics of a compressible charged fluid flowing under the action of self-consistent electric and magnetic fields, where the electric and magnetic fields satisfy the two corresponding Maxwell equations. The main feature of the new hydrodynamics is its compressibility, which, in the Lagrange description, means the compressibility of the mapping and, hence, the possibility of breaking. In terms of the Euler characteristics, the breaking of the vortex lines leads to an infinite value of the curl of velocity $\operatorname{curl}\mathbf{v} = \Omega$. In the new hydrodynamics of a charged fluid, the role of density is played by the reciprocal of J. This quantity should naturally be called the density of vortex lines. It originates from the Cauchy formula for the vorticity Ω. Variations of the density of the vortex lines are determined by the velocity component normal to the vorticity. As is shown below, the Cauchy formula can be obtained from the "new" Kelvin theorem on the circulation conservation, as well as from the analog of the Weber transformation. As a result, the Euler equations prove to be resolved with respect to the Cauchy invariants, which represent an infinite number of integrals of motion. Then, one can consider the Euler equations as partially integrated equations. For the numerical integration of the Euler equations, this fact is of fundamental importance.

0021-3640/02/7606-0346$22.00 © 2002 MAIK "Nauka/Interperiodica"

The vortex-line representation (VLR) can be applied not only to ideal hydrodynamics but also to describing viscous incompressible flows in terms of the Navier–Stokes equation. Below, for the viscous case, a diffusion-type equation describing the dynamics of the Cauchy invariant is obtained with the "diffusion tensor" determined by the VLR metric. The form of this equation coincides with that of the equation derived in [7]. The equations of motion of the vortex lines, when taken in their previous form, are understood as equations determining the change to a curvilinear coordinate system. The exact equations derived for describing viscous flows can be considered as a result of an exact separation of two time scales, namely, the inertial (in essence, nonlinear) scale and the viscous one.

2. It is well known (see, e.g., the reviews [8, 9]) that, for both two-dimensional and three-dimensional flows, the Euler equations describing an ideal incompressible fluid

$$\partial\mathbf{v}/\partial t + (\mathbf{v}\nabla)\mathbf{v} = -\nabla p, \quad \mathrm{div}\mathbf{v} = 0 \tag{1}$$

possess an infinite number of integrals of motion. These are the so-called Cauchy Lagrangian invariants. The expression for a Cauchy invariant can most simply be obtained from the Kelvin theorem on the conservation of the velocity circulation:

$$\Gamma = \oint(\mathbf{v}\cdot d\mathbf{l}), \tag{2}$$

where the integration contour $C[\mathbf{r}(t)]$ moves together with the fluid. Changing from the Euler coordinates $\mathbf{r}$ to Lagrange coordinates $\mathbf{a}$, we represent Eq. (2) in the form

$$\Gamma = \oint \dot{x}_i \frac{\partial x_i}{\partial a_k} da_k,$$

where the contour $C[\mathbf{a}]$ is fixed.

From the arbitrariness of the contour $C[\mathbf{a}]$ and from the Stokes formula, it follows that the quantity

$$\mathbf{I} = \mathrm{rot}_a\left(\dot{x}_i \frac{\partial x_i}{\partial \mathbf{a}}\right) \tag{3}$$

is conserved at every point $\mathbf{a}$. This quantity is the desired Cauchy Lagrangian invariant. According to Salmon [9], the conservation of these invariants is a consequence of the special (infinite) symmetry, i.e., the relabeling symmetry of the Lagrangian markers. If the Lagrange coordinates in Eq. (3) coincide with the initial positions of fluid particles, the invariant $\mathbf{I}$ coincides with the initial vorticity $\Omega_0(\mathbf{a})$. The Cauchy invariants characterize the freezing-in of the vortex lines in the fluid. This is a very important property according to which a fluid (Lagrangian) particle cannot leave the vortex line on which it lay at the initial instant of time. Thus, for Lagrangian particles, only one unfrozen degree of freedom is available, namely, the motion along the vortex line. From the equations of motion for the vorticity

$$\partial\Omega/\partial t = \mathrm{rot}[\mathbf{v}\times\Omega], \tag{4}$$

it follows that the motion along a vortex line does not affect the vorticity value. From this point of view, a vortex line is an invariant object, and, hence, it is natural to pass to some description that makes invariance evident from the very beginning. Such a description (vortex line representation) was proposed by Kuznetsov and Ruban [1, 6].

3. Let us consider a vortex flow ($\Omega \neq 0$) of an ideal fluid and determine this flow through the Clebsch variables λ and μ:

$$\Omega = [\nabla\lambda\times\nabla\mu]. \tag{5}$$

The geometric meaning of these variables is well known: the intersection of the surfaces $\lambda = \mathrm{const}$ and $\mu = \mathrm{const}$ determines a vortex line. It is also well known that, in the incompressible case, the Clebsch variables are Lagrangian invariants, which do not vary along the trajectories of the fluid particles:

$$\frac{\partial\lambda}{\partial t} + (\mathbf{v}\nabla)\lambda = 0; \quad \frac{\partial\mu}{\partial t} + (\mathbf{v}\nabla)\mu = 0. \tag{6}$$

Therefore, these variables can be used as markers of the vortex lines. In Eq. (5), we pass to the new variables

$$\lambda = \lambda(x, y, z), \quad \mu = \mu(x, y, z), \quad s = s(x, y, z), \tag{7}$$

where s is the parameter specifying a given vortex line. As a result, we arrive at the expression

$$\Omega(\mathbf{r}, t) = \frac{1}{J}\frac{\partial\mathbf{R}}{\partial s}. \tag{8}$$

Here,

$$J = \partial(x, y, z)/\partial(\lambda, \mu, s) \tag{9}$$

is the Jacobian of the transformation

$$\mathbf{r} = \mathbf{R}(\lambda, \mu, s). \tag{10}$$

Transformation (10) is inverse of transformation (7) and determines the corresponding transition to the curvilinear coordinate system connected to the vortex lines.

The equations of motion of the vortex lines, i.e., the equations for $\mathbf{R}(\lambda, \mu, s, t)$, can be immediately obtained from equation of motion (4) for the vorticity. However, the simplest way of deriving these equations is to use the combination of Eqs. (6):

$$\nabla\mu\left[\frac{\partial\lambda}{\partial\tau} + (\mathbf{v}\nabla)\lambda\right] - \nabla\lambda\left[\frac{\partial\mu}{\partial t} + (\mathbf{v}\nabla)\mu\right] = 0, \tag{11}$$

which is identical to Eqs. (6), because the vectors $\nabla\lambda$ and $\nabla\mu$ are linearly independent.

Applying transformation (7) to Eq. (11), we arrive at the equation of motion of a vortex line [1]:

$$\left[\frac{\partial \mathbf{R}}{\partial s}\times\left(\frac{\partial \mathbf{R}}{\partial t}-\mathbf{v}(\mathbf{R},t)\right)\right] = 0. \quad (12)$$

The important feature of this equation is its "transversality": any motion along a vortex line does not affect the vortex line itself. One can easily see that Eq. (12) is equivalent to the equation

$$\partial \mathbf{R}/\partial t = \mathbf{v}_n(\mathbf{R}, t), \quad (13)$$

where $\mathbf{v}_n$ is the velocity component normal to the vorticity vector.

According to the Darboux theorem, the Clebsch variables can always be introduced locally but not globally. It is well known that the flows parametrized through the Clebsch variables are characterized by the zero value of the helicity invariant $\int(\mathbf{v}\cdot\mathrm{rot}\mathbf{v})d\mathbf{r}$, i.e., the topological invariant characterizing the degree of linking of the vortex lines. Therefore, to introduce the vortex line representation for flows with a nontrivial topology, it is necessary to go back to the initial equations of motion, i.e., to Eqs. (1) and (4) for the velocity and vorticity.

4. According to Eq. (4), the velocity component $\mathbf{v}_\tau$ tangential to the vector Ω does not directly affect the vorticity; i.e., in Eq. (4), the velocity $\mathbf{v}$ should be replaced by its transverse component $\mathbf{v}_n$.

The equation of motion for the transverse velocity $\mathbf{v}_n$ follows from Eq. (1). It has the form of the equation of motion of a particle in an electromagnetic field:

$$\partial \mathbf{v}_n/\partial t + (\mathbf{v}_n\nabla)\mathbf{v}_n = \mathbf{E} + [\mathbf{v}_n\times\mathbf{H}], \quad (14)$$

where the electric and magnetic effective fields are determined by the expressions

$$\mathbf{E} = -\nabla\left(p+\frac{v_\tau^2}{2}\right)-\frac{\partial \mathbf{v}_\tau}{\partial t}, \quad (15)$$

$$\mathbf{H} = \mathrm{rot}\mathbf{v}_\tau. \quad (16)$$

It should be noted that the electric and magnetic fields introduced in this way are expressed through the scalar φ and vector $\mathbf{A}$ potentials according to the standard formulas

$$\varphi = p + \mathbf{v}_\tau^2/2, \quad \mathbf{A} = \mathbf{v}_\tau, \quad (17)$$

so that the two Maxwell equations

$$\mathrm{div}\mathbf{H} = 0, \quad \partial\mathbf{H}/\partial t = -\mathrm{rot}\mathbf{E}$$

are automatically satisfied. In this case, the vector potential $\mathbf{A}$ has the gauge

$$\mathrm{div}\mathbf{A} = -\mathrm{div}\mathbf{v}_n,$$

which is equivalent to the condition $\mathrm{div}\mathbf{v} = 0$.

The other two Maxwell equations can also be considered, but they carry no additional information, because the charge density ρ and the current $\mathbf{j}$ are formally determined from Eqs. (15) and (16). The basic relationship in this case is equation of motion (14) for the normal velocity component, which is the equation of motion for a nonrelativistic particle with unit charge and unit mass, with the velocity of light being also equal to unity.

Equation of motion (14) is written in the Eulerian representation. To pass to the Lagrangian representation, it is necessary to consider the equations for the "trajectories" determined by the velocity $\mathbf{v}_n$:

$$d\mathbf{R}/dt = \mathbf{v}_n(\mathbf{R}, t) \quad (18)$$

with the initial conditions

$$\mathbf{R}|_{t=0} = \mathbf{a}.$$

The solution to Eq. (18) defines the mapping

$$\mathbf{r} = \mathbf{R}(\mathbf{a}, t), \quad (19)$$

which determines the passage from the Eulerian description to a new Lagrangian description.

The equations of motion represented in terms of the new variables are essentially the Hamilton equations

$$\dot{\mathbf{P}} = -\frac{\partial h}{\partial \mathbf{R}}, \quad \dot{\mathbf{R}} = \frac{\partial h}{\partial \mathbf{P}}, \quad (20)$$

where the dots indicate the differentiation with respect to time at a fixed $\mathbf{a}$, $\mathbf{P} = \mathbf{v}_n + \mathbf{A} \equiv \mathbf{v}$ is the generalized momentum, and the particle Hamiltonian h is determined by the standard expression as a function of the momentum $\mathbf{P}$ and the coordinate $\mathbf{R}$:

$$h = \frac{1}{2}(\mathbf{P}-\mathbf{A})^2 + \varphi \equiv p + \frac{\mathbf{v}^2}{2}.$$

In Eqs. (20), the first equation is equation of motion (14) written in terms of the variables $\mathbf{a}$ and t while the second equation coincides with Eq. (18).

For the "new" hydrodynamics (14) or for its Hamiltonian formulation (20), the Kelvin theorem (which is the same as the Liouville theorem) is satisfied:

$$\Gamma = \oint(\mathbf{P}\cdot d\mathbf{R}), \quad (21)$$

where the integration goes along a closed contour moving together with the "fluid." As in the above derivation of Eq. (3), this leads to an expression for the "new" Cauchy invariant:

$$\mathbf{I} = \mathrm{rot}_a\left(P_i\frac{\partial x_i}{\partial \mathbf{a}}\right). \quad (22)$$

The latter differs from the original Cauchy invariant given by Eq. (3) in that the velocity $\mathbf{v}$ is replaced in Eq. (18) by the normal velocity component $\mathbf{v}_n$. As a result, the "new" hydrodynamics proves to be com-

pressible: $\mathrm{div}\mathbf{v}_n \neq 0$. Therefore, no restrictions are imposed on the Jacobian J of transformation (19).

From Eq. (22), one can easily obtain the expression for the vorticity Ω (compare with [1, 6]):

$$\Omega(\mathbf{r}, t) = \frac{(\Omega(\mathbf{a}) \cdot \nabla_a)\mathbf{R}(a, t)}{J}, \quad (23)$$

where J is the Jacobian of transformation (19),

$$J = \frac{\partial(x_1, x_2, x_3)}{\partial(a_1, a_2, a_3)}.$$

Above, it was taken into account that the generalized momentum $\mathbf{P}$ coincides with the velocity $\mathbf{v}$, including the instant $t = 0$: $\mathbf{P}_0(\mathbf{a}) \equiv \mathbf{v}_0(\mathbf{a})$. The quantity $\Omega_0(\mathbf{a})$ in this expression is the new Cauchy invariant (coincident with the initial vorticity) characterized by zero divergence: $\mathrm{div}_a\Omega_0(a) = 0$.

Representation (23) generalizes Eq. (5) to an arbitrary topology of vortex lines. The variables $\mathbf{a}$ in this expression can locally be interpreted as a set of λ, μ, and s.

As known (see, e.g. [6]), the expression for the Cauchy invariant can be obtained using the Weber transformation. This is the velocity representation in terms of the initial data, and it can be obtained, in particular, after the integration of the Cauchy invariant given by Eq. (23).

Consider a one-form $\omega = (\mathbf{P} \cdot d\mathbf{R})$ and calculate its time derivative. Using equations of motion (20), we obtain

$$\dot{\omega} = d[-h + (\mathbf{P}\dot{\mathbf{R}})].$$

From this expression, it follows that the vector function

$$u_k = \frac{\partial x_i}{\partial a_k} P_i,$$

which depends on t and $\mathbf{a}$, satisfies the following equation of motion:

$$\dot{u}_k = \frac{\partial}{\partial a_k}\left(-p + \frac{v_n^2}{2} - \frac{v_\tau^2}{2}\right).$$

The integration of this equation with respect to time yields the Weber transformation

$$u_k(\mathbf{a}, t) = u_{k0}(\mathbf{a}) + \partial\Phi/\partial a_k, \quad (24)$$

where the potential Φ satisfies the nonstationary Bernoulli equation

$$\dot{\Phi} = -p + v_n^2/2 - v_\tau^2/2.$$

If $\Phi|_{t=0} = 0$, the time-independent vector $\mathbf{u}_0(\mathbf{a})$ coincides with the initial velocity $\mathbf{v}_0(\mathbf{a})$. Taking the curl of Eq. (24), we again arrive at Cauchy invariant (22).

Thus, in the general situation, the equation of motion of the vortex lines has the form of Eq. (18) supplemented by Eq. (23) and by the equation

$$\Omega(\mathbf{r}, t) = \mathrm{rot}_r\mathbf{v}(\mathbf{r}, t) \quad (25)$$

with the condition $\mathrm{div}_r\mathbf{v}(\mathbf{r}, t) = 0$.

Equations of motion (18) and (25) together with Eq. (23) can be considered as the result of the partial integration of Euler equation (1). These equations are resolved with respect to the Cauchy invariants, i.e., to an infinite number of integrals of motion, which is of fundamental importance for the numerical integration (see [4, 5]). In this system, the Cauchy invariants are conserved automatically, while in the case of the direct integration of the Euler equations, it is necessary to keep track of the degree of the conservation of the Cauchy invariants. Presumably, this is one of the main limitations governing the accuracy of the discrete numerical schemes used for the direct integration of the Euler equations.

Another important property of the vortex line representation is the absence of any restrictions on the Jacobian J, whise, e.g., occur in the case of the passage from the Eulerian description to the Lagrangian description in Euler equation (1), where the Jacobian is equal to unity. The quantity $1/J$ has the meaning of the density n of the vortex lines. According to Eq. (18), this quantity, being a function of $\mathbf{r}$ and t, satisfies the continuity equation

$$\partial n/\partial t + \mathrm{div}_r(n\mathbf{v}_n) = 0. \quad (26)$$

In this equation, $\mathrm{div}_r\mathbf{v}(\mathbf{r}, t) \neq 0$, because only the full velocity $\mathbf{v}$ has a zero divergence.

5. Now, let us consider the application of the VLR to describing viscous flows.

We write the Navier–Stokes equation for the vorticity Ω in the form

$$\partial\Omega/\partial t = \mathrm{rot}[\mathbf{v} \times \Omega] - \nu\mathrm{rotrot}\Omega \quad (27)$$

and change to the variables $\mathbf{a}$ and t with the use of Eq. (18) supplemented by Cauchy relation (23) in which Ω_0 is assumed to be a function of not only coordinates $\mathbf{a}$ but also time t: $\Omega_0 = \Omega_0(\mathbf{a}, t)$.

Then, the substitution of Eq. (23) in Eq. (27) cancels the first term on the right-hand side of Eq. (27) owing to Eq. (18). As a result, Eq. (27) takes the form

$$\frac{1}{J}\left(\frac{\partial\Omega_0}{\partial t}\nabla_a\right)\mathbf{R} = -\nu\mathrm{rotrot}\left\{\frac{1}{J}(\Omega_0\nabla_a)\mathbf{R}\right\}. \quad (28)$$

Next, on the right-hand side of Eq. (28), we replace the differentiation with respect to $\mathbf{r}$ by the differentiation with respect to the variables $\mathbf{a}$. As a result of simple but time-consuming calculations, Eq. (28) is reduced to the equation for $\Omega_0(\mathbf{a}, t)$:

$$\frac{\partial\Omega_0}{\partial t} = -\nu\mathrm{rot}_a\left(\frac{\hat{g}}{J}\mathrm{rot}_a\left(\frac{\hat{g}}{J}\Omega_0\right)\right). \quad (29)$$

This equation is linear in Ω_0, and the quantity $\hat{g}$ is a metric tensor determined as

$$g_{\alpha\beta} = \frac{\partial x_i}{\partial a_\alpha}\frac{\partial x_i}{\partial a_\beta}.$$

Equation (29) for the Cauchy invariant is coincident in its form with the equation obtained by Zenkovich and Yakubovich [7] for incompressible fluid dynamics where the variables **a** have the meaning of the Lagrangian markers of fluid particles. In the Zenkovich–Yakubovich equation, the Jacobian J is assumed to be time-independent, and in the simplest case it is equal to unity. This fact determines the fundamental difference between the Zenkovich–Yakubovich equation and Eq. (29).

The remarkable feature of the system obtained above is the exact separation of the two different time scales that are responsible for the inertial (in essence, nonlinear) and viscous processes. The inertial processes are described by Eq. (18), while the viscous processes are described by the diffusion-type equation (29) in which the diffusion "coefficient" proportional to the viscosity ν has a complex tensor structure determined by the metric of the mapping $\mathbf{r} = \mathbf{R}(\mathbf{a}, t)$.

I am grateful to E.I. Yakubovich for allowing me to read the cited paper [7] before its publication.

This work was supported by the Russian Foundation for Basic Research (project no. 00-01-00929), the Program of Supporting the Leading Scientific Schools of the Russian Federation (project no. 00-15-96007), and INTAS (project no. 00-00292).

REFERENCES

1. V. I. Arnold, *Catastrophe Theory* (Znanie, Moscow, 1981; Springer-Verlag, Berlin, 1986); V. I. Arnold, *Mathematical Methods of Classical Mechanics* (Nauka, Moscow, 1984; Springer-Verlag, Berlin, 1989).
2. E. A. Kuznetsov and V. P. Ruban, Zh. Éksp. Teor. Fiz. **118**, 893 (2000) [JETP **91**, 775 (2000)].
3. V. A. Zheligovsky, E. A. Kuznetsov, and O. N. Podvigina, Pis'ma Zh. Éksp. Teor. Fiz. **74**, 402 (2001) [JETP Lett. **74**, 367 (2001)].
4. E. A. Kuznetsov, O. N. Podvigina, and V. A. Zheligovsky, in *Proceedings of IUTAH Symposium "Tubes, Sheets, and Singularities in Fluid Dynamics," Zakopane, 2002* (in press).
5. E. A. Kuznetsov and V. P. Ruban, Pis'ma Zh. Éksp. Teor. Fiz. **67**, 1015 (1998) [JETP Lett. **67**, 1076 (1998)].
6. E. A. Kuznetsov and V. P. Ruban, Phys. Rev. E **61**, 831 (2000).
7. E. I. Yakubovich and D. A. Zenkovich, in *Proceedings of the International Conference "Progress in Nonlinear Science," Nizhni Novgorod, Russia, 2001*, Ed. by A. G. Litvak (Nizhni Novgorod, 2002), p. 282; physics/0110004.
8. V. E. Zakharov and E. A. Kuznetsov, Usp. Fiz. Nauk **137**, 1137 (1977).
9. R. Salmon, Annu. Rev. Fluid Mech. **20**, 225 (1988).

Translated by E. Golyamina

JETP Letters, Vol. 76, No. 6, 2002, pp. 351–354. From Pis'ma v Zhurnal Éksperimental'noĭ i Teoreticheskoĭ Fiziki, Vol. 76, No. 6, 2002, pp. 411–414.

Formation of Two-Dimensional Crystal-Like Structures from Inclusions in Smectic C Films¶

P. Cluzeau[1], G. Joly[2], H. T. Nguyen[2], and V. K. Dolganov[3]

[1] *Laboratoire de Dynamique et de Structure des Matériaux Moleculaires, ESA CNRS 8024, Universite de Lille I 59655 Villeneuve d'Ascq Cedex, France*

[2] *Centre de Recherche Paul Pascal, CNRS, Universite de Bordeaux I, F-33600 Pessac, France*

[3] *Institute of Solid State Physics, Russian Academy of Sciences, Chernogolovka, Moscow region, 142432 Russia*

Received July 18, 2002

The structures formed by inclusions in smectic C (SmC) free-standing films are investigated using polarized light microscopy. The domains confined in these two-dimensional (2D) systems induce distortion of the in-plane orientational order, which governs the elastic interaction between the inclusions. The balance between long-range quadrupolar attraction and short-range repulsion gives rise to a nontrivial collective behavior of domains. Various 2D structures are created as a function of the concentration and size of inclusions. We observe the formation of chains and then a 2D square lattice when the concentration of domains increases. Further increase in the domain size leads to the transition from square to hexagonal close-packed structure. © *2002 MAIK "Nauka/Interperiodica"*.

PACS numbers: 61.30.Eb; 61.30.Jf

The study of dispersions of foreign particles in a liquid crystal host phase has attracted considerable interest in recent years [1–6]. Most of the investigations were performed in nematic (N) liquid crystals, in which the molecules exhibit only an orientational order. The average direction of the long molecular axis is specified by the unit-vector field *n* called the director. The orientational elasticity of the nematic host phase gives rise to long-range interaction between the particles. At long distances with respect to the inclusions size, this interaction can be expanded in multipoles. Recent theoretical and experimental studies [1–7] have shown that the effective pair interaction exhibits dipolar or quadrupolar character, depending on the boundary condition around the inclusion. In both cases, attraction between inclusions induces the formation of chain structures. More recently, interaction between inclusions was evidenced in smectic C (SmC) free-standing films [8, 9]. Such films appear as two-dimensional systems convenient for the investigation of the collective behavior of inclusions. These films consist of an integer number of molecular smectic layers oriented parallel to the free interface bounded by air. In the SmC phase, each layer is a two-dimensional anisotropic liquid with the long molecular axis tilted in a preferential direction with respect to the layer normal. The projections of the mean direction of the long molecular axis onto the layer plane define the two-dimensional (2D) field $\mathbf{c}(x, y)$ of molecular ordering called **c**-director. Long-range attraction between inclusions results from in-plane elastic deformation of the **c**-director near inclusions [10]. The first experiments have shown [8, 9] that in 2D films the inclusions organize themselves in long chains as in 3D nematic emulsion. Most of the investigations were carried out with spherical droplets in nematic or with circular inclusion at relatively low concentration of inclusions in srnectic film. But it appears quickly that anisotropic particles at high concentration should give rise to other interesting structures. For instance, it was predicted that the formation of various cellular structures depends on the shape and the concentration of inclusions [11, 12]. Recently, two-dimentional structures formed by inclusions were observed in nematic host phase [13] and in SmC films [14].

This paper deals with anisotropic inclusions nucleated in relatively thick film just below the SmC–N transition temperature. Both the concentration and the size of the inclusions can be modified over a wide range. This interesting feature allows the generation of 2D structures built with the inclusions and the study of the evolution of their organization versus the inclusion size. The periodicity of the structures is governed by the balance between the long-range attraction and the short-range repulsive interaction. If the distance between domains is on the order of or larger than their size, the pair quadrupolar interaction potential leads to a cellular structure with square lattice. A decrease of the domain–domain distance induces an overlap of the **c**-director field distortions. In this case, short-range repulsive interaction between domains plays the dominant role in the formation of cellular structure and leads to the transition into a close-packed structure exhibiting hexagonal symmetry.

¶This article was submitted by the authors in English.

0021-3640/02/7606-0351$22.00 © 2002 MAIK "Nauka/Interperiodica"

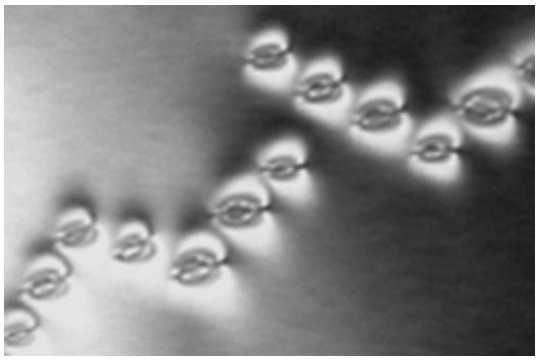

Fig. 1. Image of small domains in reflected light under crossed polarizers. At low concentration, the domains organize in a chain structure. The horizontal dimension of the image is about 195 μm, $T_0 - T = 2.1°C$.

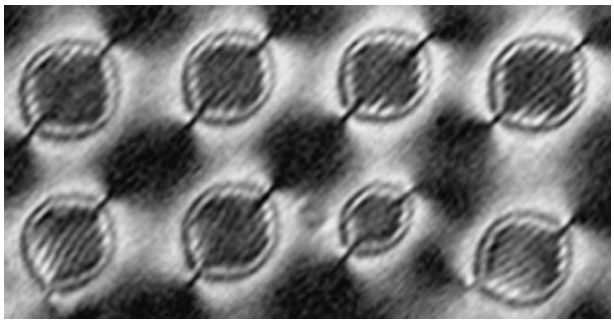

Fig. 2. Image of a square lattice of inclusions in the SmC free-standing film observed in transmission between crossed polarizers. Polarizer is oriented at 45° with respect to the horizontal axis. $T_0 - T = 1.3°C$. The horizontal size of the image is about 160 μm.

Liquid crystal used in our experiments is decyl oxybenzoic acid (DOBA), which exhibits the following phase sequence: Crystal–SmC–N–Isotropic [15]. This material is slightly doped with ethyl decyl oxybenzoate. In a bulk sample of this mixture, the SmC–N phase transition ranges from 114°C to 117°C. Impurities favor the nucleation of domains in the SmC film. The temperature of the transition of the whole film in nematic (T_0) in this case occurs at 117°C. A weak decrease of T_0 is observed with time. This decrease may result from a degradation of the material. The films are achieved by spreading the material in the SmC phase across a circular hole (4-mm diameter) in a thin glass plate. The sample temperature is controlled with an accuracy of ±20 mK. In our experiments, we used films ranging from 4 to 10 μm. Both the nucleation process and the organization of the domains are observed using polarized light reflection and transmission microscopy. The images are recorded using a CCD camera.

The inclusions consist of domains confined in the uniform background SmC free-standing films. The domains nucleate on heating approximately 3°C below the SmC–N transition temperature in the film. Figure 1 shows the first stage of organization of the domains. At low concentration they form chains. The domains exhibit a slightly elliptical shape. Note that a weak deformation of the smectic film is generally induced by the inclusion along the normal to the layer (*z* direction). Such a deformation of the film is visible by observing the thickness interference fringes in monochromatic light.

Interaction energy between inclusions can be expanded in multipoles [2] that include the dipolar and quadrupolar terms. Dipolar attraction between inelusions is anisotropic and maximum in one direction. Consequently, dipolar interaction would induce a chaining of the inclusions along only one direction. In the present case, we observed chain formation in two directions with an angle of about 110° between them (Fig. 1). The observed two orientations of chains are the signature of nondipolar interaction. Quadrupolar interaction should be repulsive for directions parallel and perpendicular to the **c**-director and becomes attractive in the intermediate directions [16]. The organization of the chains in Fig. 1 indicates that quadrupolar interaction is larger than the dipolar one. As a consequence, the final structure should be mainly determined by the quadrupolar interaction.

Figure 2 shows the film with domains of larger size and with a higher concentration. The increase of both size and density of domains leads to a 2D structure with square lattice. The large size of the domains enables us to distinguish line defects that seem to fill the domains. Such lines have been observed in free-standing film [17–19] and on the free surface of the smectic droplets [20–22]. These lines should correspond to narrow variations of the director orientation, but we cannot infer from our observations whether these lines are connected with SmC order inside the domains or only at their surface (i.e., in the smectic layers surrounding the inclusion). Actually, the type of order inside the domains remains unclear to us.

Interaction between inclusions depends on orientation of the **c**-director near their boundary. In the immediate vicinity from line defects forming domain boundary, strong director deformation takes place, and we cannot speak about an anchoring condition for the **c**-director on the boundary. However, the joined action of line defects determines the orientation of **c**-director at a short distance from the domain boundary (about a few micrometers). The strong **c**-director deformations are confined in a region close to the boundary that can be called the coat of the inclusion [23]. Inside the coat, the elastic theory is not valid. We should consider the orientation of the **c**-director outside the coat instead of the anchoring condition on the inclusion boundary. The symmetry of the distortion visible in Fig. 2 is the source of quadrupolar interaction [16, 24].

The texture observed in Fig. 2 is characterized by positional ordering of the domain centers and also ori-

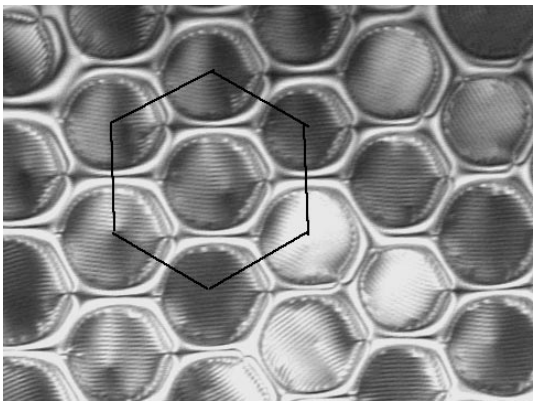

Fig. 3. Hexagonal lattice formed by close compact domains, $T_0 - T = 0.3°C$. The horizontal dimension of the image is about 260 μm.

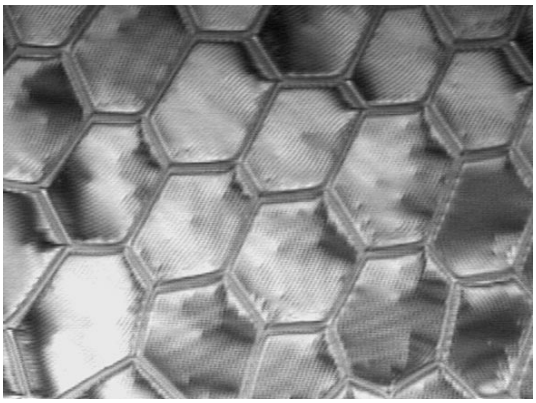

Fig. 4. 2D hexagonal structure formed by hexagonal-like domains near the temperature of the film transition to nematic phase, $T_0 - T = 0.1°C$. Horizontal dimension of image is about 260 μm.

entational ordering of their long axis. Those long axes are all oriented in the same direction. It should be noted that the periodic structure can only be achieved when the domains exhibit approximately the same size and line defects in the domains are parallel to their long axis. A change of domain size induces a defect in the periodicity (Fig. 2). So, the observed chains and square structure can be qualitatively explained by pair quadrupolar interaction.

The above-described square lattice is observed only if the ratio between the domain–domain distance and the square lattice parameter is higher than about 0.3. The heating of the film leads to an increase of domain size and, as a result, to an evolution of the structure. As the domain mobility is low, the distances between them decrease. So, increasing the domain size should be similar to an increase of pressure. At short distances, the domain shape tends to become nearly circular. In such case, the square lattice becomes unstable and a reorganization of the structure occurs. Domains change their positions and form a close-packed hexagonal structure (Fig. 3). Different domains are separated by a coat with strong distortion of the director field. Elastic theory with binary deformation interaction does not explain the domain ordering. However, it is clear that a repulsive interaction exists between the coats. In film with high domain density, there are no free regions without domain structure. As a result, the domains cannot move in order to increase the interdomain space. Even if the domains are close compact, the boundary between domains does not disappear, and we do not observe coalescence. So, the repulsive interaction resulting from the large distortion of the **c**-director in the coat is high enough to allow the formation of close-packed hexagonal structure.

Finally, further heating leads to a filling of the whole area of the film by the domains (Fig. 4). During the growth of the domains, their shape becomes hexagonal-like. The boundary between domains appears as thick strain lines. These walls are a few microns thick and should include strong distortions of the **c**-director orientation which insure the stability of the structure. This structure with compact hexagonal-like arrangement is achieved close to the temperature of the SmC–N transition. Such a film can also be considered as a 2D smectic foam.

So, in SmC film of DOB A we observed the organization of domains in three types of structure. At low concentration, domains form chains. At intermediate concentration, a two-dimensional lattice with square cell is formed. These structures result from pair quadrupolar interaction. The disappearance of the square structure occurs above some critical domain size. This structure is replaced by a regular hexagonal lattice in which the inclusions are close compact. Further increase of the domain size decreases the free area between domains and induces the change of their shape. Thus, the increase of the compactness of the structure leads to the filling of the whole SmC film by hexagonal-like domains.

The essential feature of this system is that the anchoring conditions at the boundary of the domains do not seem well defined. Thus, the interdomain interaction is probably mainly governed by the coat of different molecular orientations near the domain boundary. Such a situation is probably typical for inclusions with complicated shape and molecular orientation on the boundary.

This experimental study underlines the influence of both the breaking of the symmetry of the **c**-director field in the vicinity of the inclusion and the anisotropic shape of the domain on the structural organization of the inclusions confined in a membrane. Previous experimental studies both in film and in 3D systems have established that the boundary conditions determine the type of interactions and lead to different organizations

of inclusions. The present results demonstrate that the 2D structural organization can also be varied by the change of density and inclusion size. A comparison of the average size of domains and film thickness in order to classify the successive observed structures is under investigation. We expect that similar self-organization should be observed in other systems.

We thank the region nord-pas-de-calais and FEDER for funding of the image setup. V.D. would like to thank the University of Lille I and Laboratoire de Dynamique et de Structure des Matériaux Moleculaires for hospitality. This work was supported be the Russian Foundation for Basic Research, project no. 01-02-16507 (V.D.).

REFERENCES

1. P. Poulin, H. Stark, T. C. Lubensky, and D. A. Weitz, Science **275**, 1770 (1997).
2. T. C. Lubensky, D. Pettey, N. Currier, and H. Stark, Phys. Rev. E **57**, 610 (1998).
3. P. Poulin and D. A. Weitz, Phys. Rev. E **57**, 623 (1998).
4. H. Stark, Eur. Phys. J. B **10**, 311 (1999).
5. O. Mondain-Monval, J. C. Dedieu, T. Gulik-Krywicki, and P. Poulin, Eur. Phys. J. B **12**, 167 (1999).
6. J-C. Loudet, P. Barois, and P. Poulin, Nature **407**, 611 (2000).
7. D. Andrienko, G. Germano, and M. P. Allen, Phys. Rev. E **63**, 041701 (2001).
8. P. Cluzeau, P. Poulin, G. Joly, and H. T. Nguyen, Phys. Rev. E **63**, 031702 (2001).
9. P. Cluzeau, V. Dolganov, P. Poulin, *et al.*, Mol. Cryst. Liq. Cryst. **364**, 381 (2001).
10. D. Pettey, T. C. Lubensky, and D. Link, Liq. Cryst. **25**, 5 (1998).
11. B. I. Lev and P. M. Tomchuk, Phys. Rev. E **59**, 591 (1999).
12. K. M. Aoki, B. I. Lev, and H. Yokoyama, Mol. Cryst. Liq. Cryst. Sci. Technol., Sect. A **367**, 537 (2001).
13. V. G. Nazarenko, A. V. Nych, and B. I. Lev, Phys. Rev. Lett. **87**, 075504 (2001).
14. P. Cluzeau, G. Joly, H. T. Nguyen, and V. K. Dolganov, Pis'ma Zh. Éksp. Teor. Fiz. **75**, 573 (2002) [JETP Lett. **75**, 482 (2002)].
15. D. Demus, *Flüssige Kristalle in Tabellen* (VEB Deutscher fur Grundstoff Industrie, Leipzig, 1974); M. Petrov, A. Braslou, A. M. Levelut, and G. Durand, J. Phys. II **2**, 1159 (1992).
16. S. Ramaswamy, R. Nityananda, V. A. Raghunatha, and J. Prost, Mol. Cryst. Liq. Cryst. Sci. Technol., Sect. A **288**, 175 (1996).
17. J. Pang, C. D. Muzny, and N. A. Clark, Phys. Rev. Lett. **69**, 2783 (1992).
18. J. Pang and N. A. Clark, Phys. Rev. Lett. **73**, 2332 (1994).
19. P. Cluzeau, G. Joly, H. T. Nguyen, *et al.*, Liq. Cryst. **29** (4), 505 (2002).
20. T. J. Scheffer, H. Gruler, and G. Meier, Solid State Commun. **11**, 253 (1972).
21. C. Aller, M. Kleman, and P. Vidal, J. Phys. (Paris) **39**, 181 (1978).
22. R. Najjar and Y. Galerne, Mol. Cryst. Liq. Cryst. **367**, 395 (2001); Europhys. Lett. **55**, 355 (2001).
23. B. I. Lev, S. B. Chernyshuk, P. M. Tomchuk, and H. Yokoyama, Phys. Rev. E **65**, 021709 (2002).
24. S. P. Meeker, W. C. K. Poon, J. Grain, and E. M. Terentjev, Phys. Rev. E **61**, R6083 (2000).

JETP Letters, Vol. 76, No. 6, 2002, pp. 355–359. Translated from Pis'ma v Zhurnal Éksperimental'noĭ i Teoreticheskoĭ Fiziki, Vol. 76, No. 6, 2002, pp. 415–419.

Mobility of Electrons on a Liquid-Helium Film with a Rough Substrate

V. Shikin

Institute of Solid State Physics, Russian Academy of Sciences, Chernogolovka, Moscow region, 142432 Russia

Received June 20, 2002; in final form, July 19, 2002

The origin of the specific activation-type behavior of the mobility of electrons on liquid-helium films with different kinds of substrates is discussed. The characteristic feature of the activation energy E_a observed in the experiment is its dependence on the effective film thickness d in the form $E_a \propto d^{-2}$. A scenario of this effect is proposed with consideration for the roughness of the substrate underlying the liquid-helium film. © *2002 MAIK "Nauka/Interperiodica".*

PACS numbers: 67.70.+n; 77.84.Nh

The variety of interesting experimental results that have not yet found any appropriate interpretation include the data on the mobility of electrons on thin liquid-helium films overlying different kinds of substrates. These data demonstrate the activation behavior of the liquid-helium films, and the activation energy E_a is found to be inversely proportional to the square of the effective film thickness [1–4].

An explanation of this effect on the basis of the polaron hypothesis was proposed by Platzman [2]. It was assumed that an electron on a thin liquid-helium film overlying an ideal substrate forms a bound state (a single-electron dip). The main parameters of the dip can be calculated in terms of the Feynman approximation [5]. Specifically, its effective mass M is expressed as [6, 7]

$$M \propto \exp(\sqrt{\alpha}), \quad \alpha = \frac{mF_*^2}{4\pi\sigma(\hbar k_c)^2}, \tag{1}$$

$$F_* = eE_\perp + \Lambda/d^2, \quad \Lambda = \frac{e^2(\epsilon_d - \epsilon)}{(1+\epsilon)^2(\epsilon_d + \epsilon)}, \tag{2}$$

where k_c is the characteristic cutoff factor of the order of the inverse size of the electron wave function in the dip; ϵ and ϵ_d are the dielectric constants of the liquid helium and the solid substrate, respectively; and d is the local thickness of the liquid-helium film.

Assuming that the dip mobility is $\mu \propto M^{-1}$ and taking into account definitions (1) and (2), Platzman [2] derived the formula $\mu \propto \exp(-\beta/d^2)$, which explains the experimental data [1–4]. However, the same formalism leads to a rather low probability of the dip formation on the surface of a liquid-helium film in the temperature range $T \leq 1$ K [8].

In other versions of the theory of single-electron dips [9], the effective mass M proves to be only a power function of d:

$$M \equiv \frac{\rho F_*^2}{8\pi\sigma^2\kappa_*^2 d}, \quad \kappa_*^2 = \rho g_*/\sigma, \quad \kappa_* d < 1, \tag{3}$$

where ρ and σ are the density and the surface tension of liquid helium and g_* is the effective acceleration of gravity [for details, see Eq. (23) given below]. In addition, the hypothesis of $\mu \propto M^{-1}$ is questionable. According to [9], the mobility is expressed as

$$\mu \equiv \frac{4\pi\sigma^2 e(\kappa_* d)^2 d}{3\eta_l F_*^2}, \tag{4}$$

where η_l is the viscosity of liquid helium and F_* is defined by Eq. (2). Evidently, the quantity M^{-1} determined from Eq. (3) is not identical with the quantity μ given by Eq. (4) in terms of its dependence on the film thickness.

Thus, the experimental data [1–4] that provide the dependence $\mu \equiv \exp(-\beta/d^2)$ for different solid substrates and for a wide range of film thickness values d may be of nonpolaron origin. The issue remains open to discussion.

The present paper considers an alternative scenario for the specific behavior of the electron mobility on a liquid-helium film with allowance for the roughness of the solid substrate. Such a roughness is practically inevitable in real experiments with thin liquid films.

1. The equation for the profile $d(x, y)$ of a liquid-helium film on a rough substrate has the form

$$\sigma\frac{\Delta_2 d}{\sqrt{1+(\nabla d)^2}} - \rho g d(x,y) + \frac{f}{(d-\delta)^3} = -\rho g h. \tag{5}$$

0021-3640/02/7606-0355$22.00

The thickness $d(x, y)$ is measured relative to the zero point $\delta(x, y)$, g is the acceleration of gravity, f is the Van der Waals constant (usually, about several tens of degrees), and h is the height of the pedestal above the bulk liquid helium level (measured relative to the zero point $\delta(x, y)$). In the absence of roughness, Eq. (5) is reduced to the definition of the equilibrium thickness $\bar{d}$ of a film on a flat substrate:

$$f/\bar{d}^3 = \rho g(\bar{d} - h). \tag{6}$$

When $h > 0$, the solution of Eq. (6) is possible for $\bar{d} \geq h$. At $h = 0$, the quantity $\bar{d}$ from Eq. (6) remains finite. Finally, when h is negative, Eq. (6) takes the form that is conventional for the determination of the saturation film:

$$f/\bar{d}^3 = \rho g h_m, \quad h_m \equiv |h| \gg \bar{d}. \tag{6a}$$

Note that definitions (5) and (6) contain no delay effects, which complicate the behavior of the Van der Waals forces for small values of h. This simplification does not affect the qualitative picture given by Eqs. (6) and (6a) for $d(h)$ when h passes through zero, and it is justified in the limit of small film thickness (large values of h_m), which is the case of our interest.

Now, let us consider the function $\delta(x, y) \neq 0$ and assume that it is characterized by the normal amplitude distribution

$$D(\delta) = \frac{1}{(2\pi\Delta^2)^{1/2}}\exp(-\delta^2/2\Delta^2), \quad \int_{-\infty}^{+\infty}\delta(x, y)dxdy = 0, \tag{7}$$

where $\Delta^2 = \langle\delta^2\rangle$ is the mean square variance of the distribution, and by the correlation functions

$$\langle\delta(x, y)\delta(x - x', y)\rangle = \Delta^2\exp(-x'^2/2\eta^2), \quad \langle\delta(x, y)\delta(x, y - y')\rangle = \Delta^2\exp(-y'^2/2\eta^2), \tag{8}$$

where $\langle\eta^2\rangle$ is the characteristic correlation radius. For simplicity, the latter is assumed to be the same in both horizontal directions.

In the conditions $\delta(x, y) \neq 0$, the problem on the profile $d(x, y)$ is approximately reduced to the problem of the effective height at which the sphere (cylinder) of radius R moving downward is stopped by a forest of vertices with stochastic properties (7) and (8). As the height h monotonically varies, the role of the effective screening radius R is sequentially played by the quantities

$$R_o^2 = \sigma/\rho g, \tag{9a}$$

$$R = \sigma/\rho g h_m, \tag{9b}$$

$$R_*^2 = \sigma/\rho g_*, \tag{9c}$$

where

$$g_* = 3f/(\sigma\bar{d}^4), \quad h_m = |h|.$$

These quantities follow from the analysis of the properties of Eq. (5): the radius R_o given by Eq. (9a) is known from the classical theory of meniscus [10], the quantity R given by Eq. (9b) follows from Eq. (5) when the Van der Waals forces can be neglected in the interval between the edge points of the meniscus, and the appearance of the radius R_* given by Eq. (9c) will be demonstrated below [see Eqs. (23) and (24)].

Using the general determination of the number of peaks of $\delta(x, y) \neq 0$ that rise above a given height (see, e.g., [11]) and applying Eq. (5), for which these peaks (the so-called active peaks) participate in the formation of the effective boundary conditions, we can trace different limiting cases in the behavior of $d(x, y)$.

The exotic case (9a) is realized in the region $h > 0$. The role of roughness in this region is minor.

Variant (9b) represents a more actual case realized for small negative values of h. In this case, liquid menisci of radius R "hang" on the active peaks of height δ_a with a distance b_a between them. The quantities δ_a and b_a are related to the parameters of the problem R, Δ, and η by the expressions

$$R = \frac{b_a}{2}\sqrt{1 + \frac{b_a^2}{2\Delta^2}\ln\frac{b_a}{s\eta}}, \quad \frac{\delta_a^2}{2\Delta^2} = \ln\frac{b_a}{s\eta}, \quad b_a/s\eta \gg 1, \quad s^2 = 2\pi, \tag{10}$$

where Δ and η are taken from Eqs. (7) and (8).

The minimal film thickness $d_{\min}$ in the central part of a meniscus of radius R is determined as

$$d_{\min} = \Delta_m[\sqrt{2}(\ln(\Delta^{1/2}R^{1/2}/s\eta)) - 1/2], \quad \Delta_m = |\Delta|. \tag{11}$$

For the meniscus not to be considerably affected by the Van der Waals forces, the minimal thickness should exceed Δ_m. This requirement formulated in terms of h as

$$h_m < h_m^{\rm cr}, \quad [\sqrt{2}(\ln(\Delta^{1/2}R_{\rm cr}^{1/2}/s\eta)) - 1/2] = 1, \quad R_{\rm cr} = 2\sigma/\rho g h_m^{\rm cr}, \tag{12}$$

determines the domain of validity of case (9b).

Scenario (9b) corresponds to the initial stage of the effect of roughness on the properties of 2D electrons. Here, it is expedient to separate the electron density into two components:

$$n_s = n_e + n_l, \tag{13}$$

where n_e represents the free electrons retaining a good mobility along the menisci of radius R and n_l represents the localized electrons confined to the active peaks of the profile $d(x, y)$. To calculate the mobility of quasi-

free electrons on a rough substrate, one can use perturbation theory: the Born approximation, the kinetic equation, etc. However, the limiting case under discussion is unlikely to lead to the activation behavior of the electron mobility as a function of roughness and thickness of the film, although such attempts can be found in the literature [12–14].

In the conditions $h_m < h_m^{cr}$, the Laplace screening radius R_* becomes comparable with η [scenario (9c)] and the characteristic quantity d_{min} decreases to the region $d_{min} \le 0$, so that the Van der Waals forces can no more be ignored in the intervals between the peaks δ_a. Separation (13) of the electron density into two subsystems becomes invalid, because, in this case, all electrons strongly interact with the substrate. As will be shown below, in scenario (9c), the electron mobility is governed by the two following characteristics: the effective positions of the saddle points of the relief $\delta(x, y) \neq 0$ and the degree of screening of the deep valleys of this relief by the liquid-helium film. For the regime corresponding to Eq. (9c), the central problem is the determination of these characteristics.

Answers to the stated questions can be obtained by using the mutual probability W_n of different quantities in the problem with a normal randomness given by Eqs. (7) and (8) (see [11]). In the case under study, we deal with the combined probability of $\delta(x, y)$ and its second derivatives. Introducing the simplifying notations

$$\xi_1 = \delta, \quad \xi_2 = \delta''_x, \quad \xi_3 = \delta''_y,$$

we obtain an expression for W_3:

$$W_3(\xi_1, \xi_2, \xi_3) = \frac{1}{(2\pi)^{3/2}\sigma_1\sigma_2\sigma_3 D^{1/2}} \times \exp\left[-\frac{1}{2D}\sum_{i,j=1}^{3} D_{ij}\frac{(\xi_i - m_i)(\xi_j - m_j)}{\sigma_i\sigma_j}\right]. \quad (14)$$

Here, $m_i = \langle\xi_i\rangle$ (in our case, all m_i are equal to zero), $\sigma_i^2 = \langle(\xi_i - m_i)^2\rangle$ is the variance of the random quantity ξ_i, D is the third-order determinant

$$D = \begin{pmatrix} 1 & Q_{12} & Q_{13} \\ Q_{21} & 1 & Q_{23} \\ Q_{31} & Q_{32} & 1 \end{pmatrix},$$

composed of the correlation coefficients

$$Q_{ij} = \langle(\xi_i - m_i)(\xi_j - m_j)\rangle/\sigma_i\sigma_j,$$

and D_{ij} is the cofactor of the element Q_{ij} of the determinant D.

Using W_3, we determine the position $\delta = \delta_c$ of the effective percolation plane for the relief $\delta(x, y)$. By definition, it is the plane near which the second derivatives δ_i'' are equal in magnitude [the consequence of the isotropy of the adopted model (8)] and opposite in sign. Then, the optimal value of δ_c is determined from the condition

$$\partial W_3/\partial\delta|_{\delta''_y = -\delta''_x} = 0. \quad (15)$$

Differentiating W_3 from Eq. (14) with respect to ξ_1 at fixed derivatives δ_i'', we obtain

$$\frac{D_{11}}{\sigma_1^2}\xi_1 + \frac{D_{12}}{\sigma_1\sigma_2}(\xi_2 + \xi_3) = 0, \quad D_{12} = D_{21}, \quad \sigma_2 = \sigma_3. \quad (16)$$

If, according to Eq. (15), we set $\xi_2 = -\xi_3$, we have

$$\xi_1^c \equiv \delta_c = 0. \quad (17)$$

In other words, the percolation plane lies at the zero level in the coordinate system related to the symmetry plane of the function $\delta(x, y)$ (this result seems to be reasonable by intuition, even without justification).

Relation (16) also is the key equation for the problem on the optimal value of the amplitude δ_* of the valleys in the relief $\delta(x, y)$. The valleys are assumed to be characterized by a given positive curvature R_*^{-1} (the peaks of $\delta(x, y)$ have a negative curvature and the valleys have a positive curvature):

$$\delta''_y = \delta''_x = R_*^{-1}. \quad (18)$$

From Eq. (16), we obtain the following relation for $\delta_* \equiv \xi_1^*$:

$$\frac{D_{11}}{\sigma_1^2}\xi_1^* + \frac{D_{12}}{\sigma_1\sigma_2}2R_*^{-1} = 0. \quad (19)$$

Using Eqs. (7) and (8) and the general rules for calculating the correlation functions, which allow one to determine the explicit form of the combinations

$$\sigma_1^2 = \Delta^2, \quad \sigma_2 = \sigma_3^2 = 3\Delta^2/\eta^4,$$

$$\langle\xi_1\xi_2\rangle = \langle\xi_1\xi_3\rangle = -\Delta^2/\eta^2, \quad \langle\xi_2\xi_3\rangle = 0$$

arising in Eq. (19), from Eqs. (18) and (19) we obtain

$$\delta_* = -2\eta^2/3R_*. \quad (20)$$

The quantity δ_* has a simple physical meaning. All valleys of the relief $\delta(x, y)$ that have a depth $\delta_\downarrow$ smaller in magnitude than δ_* are covered with the liquid-helium film, which practically reproduces the details of the surface roughness. The valleys whose depth is $|\delta_\downarrow| > |\delta_*|$ are filled with liquid helium to the level δ_* with a meniscus radius R_*.

Here, it is appropriate to demonstrate how the radius R_* appears in the problem. Assuming that inside a given valley we have

$$\begin{aligned} d(x, y) &= -d_\downarrow + \zeta(x, y), \quad |\zeta| \ll |d_\downarrow|, \\ \delta(x) &= -\delta_\downarrow + \xi(x, y), \quad |\xi| \ll |d_\downarrow|, \end{aligned} \tag{21}$$

from Eq. (5) in the zero approximation we obtain

$$\frac{f}{(-d_\downarrow + \delta_\downarrow)^3} = -\rho g h, \tag{22}$$

i.e., the effective thickness of the film coincides with the flat definition of $\bar{d}$ given by Eq. (6a):

$$(-d_\downarrow + \delta_\downarrow) \simeq \bar{d}.$$

The next approximation yields

$$\begin{aligned} \sigma\frac{\Delta_2\zeta}{\sqrt{1 + (\nabla\zeta)^2}} - \rho g_*\zeta(x, y) + F_f\xi(x, y) &= 0, \\ F_f = 3f/\bar{d}^4, \quad g_* &= g + F_f/\rho. \end{aligned} \tag{23}$$

Equation (23) involves the characteristic length

$$R_*^2 \simeq \sigma/\rho g^*, \tag{24}$$

which determines the properties of the liquid meniscus in the conditions opposite to conditions (12) [scenario (9c)].

2. An electron on a liquid-helium film interacts with the substrate through several channels. One of them is the direct interaction of the electron with the partially screened pressing field $E_\perp^*$. For a plane boundary, the internal field suppressing the disturbance $E_\perp$ in the region occupied by the substrate is completely localized inside the substrate and does not affect the dynamics of the 2D electrons over its surface. If the boundary (for simplicity, a metal boundary) is curved, the requirement that it be equipotential in the external field leads to the appearance of a screening electric potential $\tilde{\varphi}$ that is nonzero in vacuum above the boundary. This potential is harmonic and satisfies the boundary conditions

$$\begin{aligned} eE_\perp\delta(x) + e\tilde{\varphi}(x, 0) &= \text{const} \equiv 0, \\ \tilde{\varphi}(x, z \longrightarrow +\infty) &\longrightarrow 0, \end{aligned} \tag{25}$$

so that

$$\tilde{\varphi}(x, z) = \int_{-\infty}^{+\infty} dq\varphi_q e^{-iqx}e^{-qz}, \quad \varphi_q = -E_\perp\delta_q, \tag{26}$$

where δ_q is the Fourier component of the function $\delta(x)$.

Taking into account Eq. (25), we arrive at the following renormalization of the pressing field:

$$\tilde{E}_\perp = E_\perp + \partial\tilde{\varphi}(x, d)/\partial z. \tag{27}$$

In addition, a "horizontal" fluctuating component of the electron energy in the external field comes into play:

$$U_\parallel = eE_\perp(x) + e\tilde{\varphi}(x, d). \tag{28}$$

In the long-wave limit $qd \ll 1$, we have

$$U_\parallel \simeq eE_\perp[d(x) - \delta(x)], \tag{29}$$

and, as in the case of the pressing field, the polarization attraction to the rough substrate requires a modification of the "plane" formulas determining this interaction. It is possible to develop the "quasi-plane" approximation [a formula of the type of Eq. (2) with a varying film thickness following the profile $\delta(x, y)$]. However, the formalism arising in this case is fairly cumbersome and yields foreseeable results only in the region $h_m > h_m^{\text{cr}}$ [h_m^{cr} is from Eq. (12)], i.e., where the linearization of the initial equation (5) is possible. In the case $h_m > h_m^{\text{cr}}$, it is more convenient to replace the real profile of the substrate by some horizontally uniform density distribution $n(z)$ smoothly increasing from zero to the bulk value n_o with a characteristic size of the transition region of the order of Δ. In this case, the force F_p of the electron attraction to the dielectric medium with a smooth profile $n(z)$ is represented in the form

$$\begin{aligned} F_p(z) &= \int f(r)n(z - z_1)dx_1dy_1dz_1, \\ f(r) &= 2\alpha_o e^2/r^5, \quad r > a. \end{aligned} \tag{30}$$

Here, $f(r)$ is the force of the polarization interaction of a single atom of the substrate with an electron, α_o is the polarizability of a single atom, r is the distance between an electron and a given atom of the substrate, and a is the interatomic distance.

Formula (30) has the necessary asymptotic properties: the interaction is small for small values of $n(z)$ and in the region $n(z) \longrightarrow n_o$. The maximum of F_p is reached in the middle part of the transition region. In this zone, the density gradient is estimated by the expression (the origin $z = 0$ coincides with the maximum of dn/dz)

$$dn/dz \simeq n_o/\Delta. \tag{31}$$

Then, integral (30) can be calculated to obtain

$$F_p(0) \simeq \pi n_o\alpha_o e^2/a\Delta. \tag{32}$$

The integral characteristic $F_p(0)$ given by Eq. (32) adequately describes the character of the polarization attraction of an electron to a rough substrate. Using Eq. (32), the corresponding interaction energy can be represented as

$$U_p \simeq F_p(0)\delta(x), \quad \delta > \delta_*, \tag{33}$$

where δ_* is determined by Eq. (20).

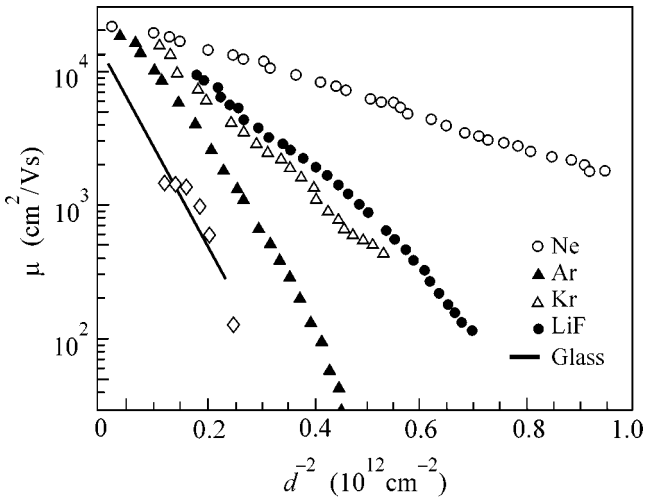

Logarithm of the 2D electron mobility on thin liquid-helium films with different substrates as a function of the square of the inverse film thickness d. The circles and the triangles represent the data from [2], the diamonds show the data from [3], and the solid line shows the data from [4] reduced by a factor of ten.

3. The results described above are sufficient to estimate the activation energy for the electron motion along a thin liquid-helium film on a rough substrate. In the general case, the solution of the problem on the activation mobility is an independent problem that requires considerable effort in every specific case (see, e.g., [15]). However, for estimating the exponent, it is sufficient to use only the energy considerations.

First of all, from the expressions for the effective energy of an electron on a rough substrate [see Eqs. (29) and (33)],

$$U_* \simeq F_*\delta(x), \quad F_* = eE_\perp + F_p(0), \tag{34}$$

it follows that, in the low-temperature limit $T \ll E_a$, all 2D electrons must be in the liquid-helium dips screening the valleys with $\delta \le \delta_*$ [δ_* is from Eq. (20)] (on condition that the number of such places is sufficient, which is assumed to be the case under consideration).

By definition, the activation energy E_a is the difference between the values of the electron energy at the percolation level and in the dips [Eq. (34)]. Using the result obtained above for the position of the percolation level [according to Eq. (17), $\delta_c = 0$], we obtain

$$E_a = -F_*\delta_*, \text{ or } E_a = \frac{2\pi n_o \alpha_o e^2 \eta^2 f^{1/2}}{a\Delta d^2\sqrt{3\sigma}}. \tag{35}$$

This energy is proportional to d^{-2}, which is the desired result.

The experimental data on the mobility of electrons on thin liquid-helium films with different substrates are shown in the figure. The dependence $E_a \propto d^{-2}$ is clearly visible, although the slopes of the lines d^{-2} vary considerably. According to Eq. (35), in addition to the known quantities, the proportionality coefficient in the definition of E_a contains the roughness parameters Δ and η. In a real 2D case, the horizontal correlations η_x and η_y may be different. Therefore, the knowledge of only one value (the slope of the line $\ln\mu(d^{-2})$ in the figure) is insufficient for obtaining a detailed information on the roughness parameters of the substrate.

Thus, in this paper, we determined different variants (9) possible for the screening of the roughness of a solid substrate by a liquid-helium film. Each variant corresponds to a specific type of the electron mobility over liquid helium. In regime (9c), this mobility proves to be of the activation character. In this case, without special limitations, the hopping mechanism of the electron motion leads to the dependence $E_a \propto d^{-2}$ observed in the experiment. The proposed alternative with consideration for the roughness seems to be more credible than the polaronic version [2] of this effect.

REFERENCES

1. F. Mende, Yu. Kovdria, and V. Nikolaenko, Fiz. Nizk. Temp. **11**, 646 (1985) [Sov. J. Low Temp. Phys. **11**, 355 (1985)].
2. P. Platzman, Surf. Sci. **170**, 55 (1986).
3. H. Jiang and A. Dahm, Surf. Sci. **229**, 352 (1990).
4. X. Hu and A. Dahm, Cryogenics **32**, 681 (1990).
5. R. P. Feynman and A. R. Hibbs, *Quantum Mechanics and Path Integrals* (McGraw-Hill, New York, 1965; Mir, Moscow, 1968).
6. S. Jackson and P. Platzman, Phys. Rev. B **24**, 499 (1981).
7. S. Jackson and P. Platzman, Phys. Rev. B **25**, 4886 (1982).
8. F. Peeters and S. Jackson, Phys. Rev. B **34**, 1539 (1986).
9. V. B. Shikin and Yu. P. Monarkha, *Two-Dimensional Charged Systems in Helium* (Nauka, Moscow, 1989).
10. L. D. Landau and E. M. Lifshitz, *Course of Theoretical Physics*, Vol. 6: *Fluid Mechanics* (Nauka, Moscow, 1986; Pergamon, New York, 1987).
11. V. Tikhonov, *Spike of Random Processes* (Nauka, Moscow, 1970).
12. Yu. Monarkha, U. Albrecht, K. Kono, and P. Leiderer, Phys. Rev. B **47**, 13812 (1993).
13. S. Sokolov, J. P. Rino, and N. Studart, Phys. Rev. B **51**, 11068 (1995).
14. D. Coimbra, S. Sokolov, J. P. Rino, and N. Studart, J. Low Temp. Phys. **126**, 505 (2002).
15. S. Chandrasekhar, Rev. Mod. Phys. **15**, 1 (1943).

Translated by E. Golyamina

JETP Letters, Vol. 76, No. 6, 2002, pp. 360–364. Translated from Pis'ma v Zhurnal Éksperimental'noĭ i Teoreticheskoĭ Fiziki, Vol. 76, No. 6, 2002, pp. 420–424.

Manifestation of Coulomb Gap in Two-Dimensional *p*-GaAs–AlGaAs Structures with Filled Upper Hubbard Band

N. V. Agrinskaya*, V. I. Kozub, V. M. Ustinov, A. V. Chernyaev, and D. V. Shamshur

Ioffe Physicotechnical Institute, Russian Academy of Sciences, Politekhnicheskaya ul. 26, St. Petersburg, 194021 Russia

** e-mail: nina.agrins@pop.ioffe.rssi.ru*

Received July 24, 2002

The transport properties of multilayer GaAs/AlGaAs structures doped modulationally with Be so as to fill, in equilibrium, the states of upper Hubbard band (A^+ centers) with holes were studied. For the concentration of dopants on the order of 5×10^{11} cm^{-2}, the hopping conduction over the states in the Coulomb gap was observed in the temperature range 0.4–4 K. The characteristic temperature (T_1) was determined from the temperature dependence of conductance and found to be appreciably lower (by 30 times) than its theoretically predicted value. This discrepancy is assumed to be due to the correlated hopping effect. In the temperature dependence of magnetoresistance, the suppression of negative magnetoresistance was observed with lowering temperature. This is explained by the weakness of underbarrier scattering in the transport via the upper Hubbard band.

PACS numbers: 73.40.Kp; 73.21.Ac; 72.20.Ee; 75.70.Cn

INTRODUCTION

In recent years, much interest has been shown in studying two-dimensional structures. This is largely caused by the observation of the transition from the insulator type of conduction to the metallic type in such structures [1]. We have recently proposed an explanation of the experimental data assuming that the "tail" of localized states in a system with potential disorder and, in particular, the states of upper Hubbard band play an important role in transport [2].

In our earlier study [3] of multilayer Be-doped *p*-type GaAs/AlGaAs structures with 15-nm-thick wells, the low-temperature two-dimensional variable-range hopping conduction over the states of upper Hubbard band was studied in detail. By doping the well and a nearby barrier layer, a situation was realized where the upper Hubbard band (A^+ centers) was filled, in equilibrium, with holes and the conduction was over its states. It was established that the conductance in weakly doped samples followed Mott's hopping law over the whole temperature interval studied (4–0.4 K). The magnetoresistance in weak fields was negative (i.e., involved quantum interference). The temperature dependence of the positive quadratic magnetoresistance (which was observed in higher fields) was used to determine the localization radius of A^+ centers (10 nm).

It should be emphasized once more that the observed hopping conduction had Mott's character. At the same time, it is well known that the conduction via the states in the Coulomb gap is more typical for semiconductors; in the three-dimensional case, the corresponding law should invariably prevail with lowering temperature (even if Mott's law is observed at high temperatures). Therefore, it was of interest to find out how Mott's hopping conduction in the structures studied in this work transforms into the conduction over the Coulomb-gap states upon lowering temperature, which are the parameters of Coulomb gap, and what the character of magnetoresistance in the Coulomb-gap regime is. Note that Mott's conduction, both in our case and in the experiments of other authors with similar structures, was observed at a sufficiently low impurity concentration. However, one can easily see that, as the crossover from the hopping conduction to the Drude conduction in 2D structures is approached at low temperatures, the hopping conduction via the Coulomb-gap states should be observed. Indeed, the crossover temperature from Mott's conduction to the Coulomb-gap conduction can be expressed in the 2D case as

$$T_c = \frac{T_1^3}{T_0^2} \approx \frac{e^6}{\kappa^3} N(\varepsilon_f)^2 a, \quad (1)$$

where κ is the dielectric constant, a is the localization radius, $N(\varepsilon_f)$ is the density of states at the Fermi level, and T_1 and T_0 are the exponential factors in the temperature dependences of the conductivity in the Coulomb-gap and Mott's law, respectively:

$$\rho = \rho_0 \exp\left(\frac{T_1}{T}\right)^{1/2}, \quad T_1 = C_2 \frac{e^2}{\kappa a}; \quad (2)$$

$$\rho = \rho_0 \exp\left(\frac{T_1}{T}\right)^{1/3}, \quad T_0 = C_1 (N_{E_f} a^2)^{-1}. \quad (3)$$

Let us consider the dependence of T_c on the dopant concentration in the region close to its critical value for the

metal–insulator transition. Considering that the dielectric constant for 2D systems is independent of (or depends only weakly on) the impurity concentration in the vicinity of the transition [4], one finds that T_c must increase as the transition is approached (due to the divergence of the localization radius and increase in the density of states). Therefore, in the 2D samples (in which the carrier concentration changes because of changing dopant concentration) close to the transition, the Coulomb gap should be observed at low temperatures. Such a behavior is opposite to that observed for 3D samples, where the samples close to the transition obey Mott's law over the whole range of attainable temperatures [5].

Note that the estimation of the pre-exponential factor in Eq. (2) is of fundamental importance. In the case of hopping induced by the electron–electron interaction, it should have a universal form $\rho_0 = h/2e^2$, while for the phonon-assisted hopping it may depend on temperature as $\rho_0 \approx AT$, where the factor A is not universal and depends on the parameters of a material [6]. It was assumed by Alenier *et al.* [7] that the pre-exponential factor may be observed in the samples close to metals, where $T_1 \approx T$.

Most of the known observations of the Coulomb gap in 2D samples are related to samples with a gate [8]. In the presence of a gate, the Coulomb interaction is screened at distances larger than the distance from the 2D layer to the gate. Accordingly, as the temperature tends to zero, i.e., as the hopping distance increases, the Coulomb gap becomes irrelevant and Mott's law prevails, despite the fact that, in the absence of a gate, the Coulomb gap should manifest itself precisely in the low-temperature region. In this respect, the system under study is of considerable interest, because it does not contain a gate. Note that such systems have not been considered until now. The sole exception is provided by work [9], where the 2D impurity conduction was also studied for the doped wells but in a temperature range not sufficiently wide for the crossover from one law to the other be observed.

In the GaAs/AlGaAs system of interest, the well width was $d \sim 15$ nm and the localization radius of the acceptor Be impurity was 2 nm, i.e., much smaller than d. By selectively doping the central areas of wells and barriers, a situation was realized where the upper acceptor (A^+-center) Hubbard band was filled in equilibrium. This case is of interest because the transport via the upper Hubbard band may exhibit some special features that are caused by a large radius of the states. Moreover, this situation is more suitable for the experiment, because the binding energy of A^+ centers is lower than for the A^0 centers, so that the samples are low-ohmic at low temperatures.

In this work, we demonstrate that the Coulomb gap manifests itself in the low-temperature hopping conduction of heavily doped samples. In contrast to the weakly doped samples, the weak-field magnetoresistance is positive. The observed behavior is discussed within the framework of the correlated-hopping and weak-underbarrier-scattering models.

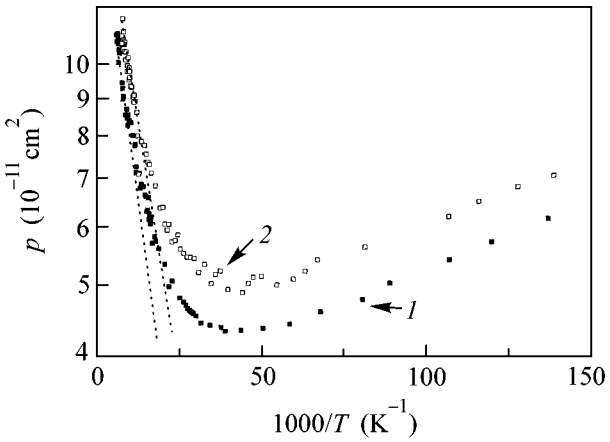

Fig. 1. Temperature dependence of the hole concentration in wells, as calculated from the Hall coefficient for samples (■) 1 and (□) 2.

EXPERIMENTAL

The method of growing multilayer structures by molecular-beam epitaxy was described in our work [3]. The structures contained ten 15-nm-thick GaAs quantum wells separated by 15-nm-thick $Al_{0.3}Ga_{0.7}As$ barriers. In the samples, 5-nm-thick middle areas of quantum wells and $Al_{0.3}Ga_{0.7}As$ barriers were doped. Therefore, the thickness of the undoped spacer layers on both sides of the barrier was 5 nm. Beryllium (with a volume concentration of 5×10^{17} cm^3) served as a p-type dopant. The contacts to the samples were produced by firing indium with a low zinc concentration for 2 min at a temperature of 450°C.

The temperature dependences of hole concentration are shown in Fig. 1. At temperature near 40 K, a maximum was observed in the temperature curves for the Hall coefficient, flagging the transition to hopping conduction. Close to room temperatures, the curves show activation behavior caused by the transition of holes from the A^+ centers to the band of delocalized states. These portions of the curves were used to estimate the binding energy of the A^+ centers at 5.5 meV. This value is slightly smaller than the values obtained by us in [3] for the similar structures because of the higher impurity concentration and width of the upper Hubbard band. At low temperatures (10–0.4 K) and sufficiently low voltages (0.1–0.01 V) and currents (10–100 nA), the conductance is ohmic and its temperature dependence corresponds to the variable-range hopping conduction (VRHC) in the Coulomb-gap regime given by Eq. (2). We have attempted to describe the observed temperature dependence using a universal (Fig. 2a) and temperature-dependent (Fig. 2b) pre-exponential factors. The

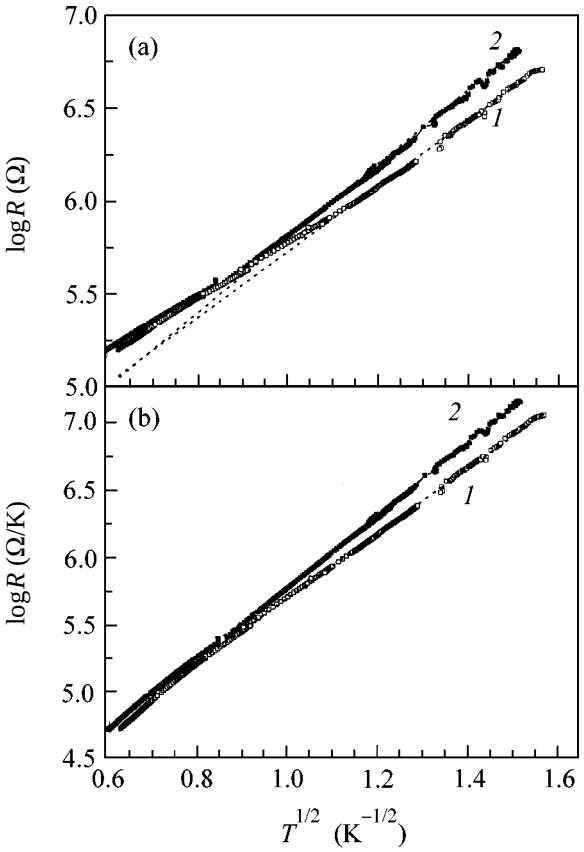

Fig. 2. Temperature dependence of the resistance (per one well) of the *p*-GaAs/AlGaAs structure in the range 0.4–4 K at the scale (a) not taking into account and (b) taking into account the temperature dependence of the pre-exponential factor. Curves *1* and *2* are for samples 1 and 2, respectively.

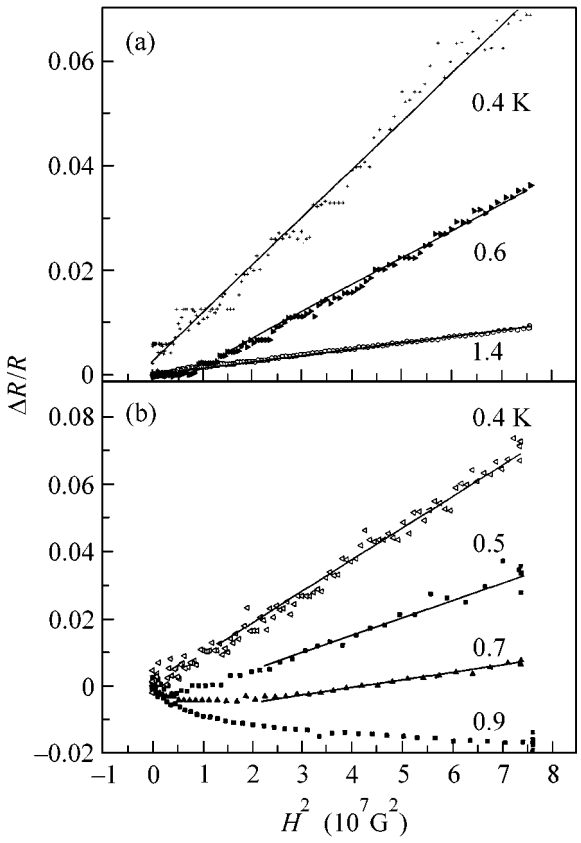

Fig. 3. Quadratic positive magnetoresistance at different temperatures for samples (a) 1 and (b) 2.

parameters T_1 estimated from Fig. 1a (16 and 19 K) and Fig. 1b (37 and 43 K) for two samples differ from one another almost by a factor of two.

The pre-exponential factor estimated for two samples from Fig. 1a was found to be close to $\rho_0 = h/2e^2 \sim 10^4\ \Omega$. At the same time, with a temperature-dependent pre-exponential factor, the curves straighten out in a larger temperature interval (Fig. 2b). The corresponding pre-exponential factor A ($\rho_0 \approx AT$), when extrapolated to the temperatures on the order of T_1, proves to be smaller than or on the order of h/e^2, which cannot be true for the phonon-assisted hopping. Therefore, the situation with the temperature-independent pre-exponential factor seems to be more realistic.

The magnetoresistance (MR) was measured in static magnetic fields perpendicular to the structure plane up to 1 T (note that for the fields parallel to the structure, the MR was virtually absent). The typical low-field MR curves are shown in Fig. 3 for two samples at several temperatures. A portion of negative MR is seen in the curves for sample 1; on further decrease in temperature, it disappears and the quadratic positive MR prevails. In the other sample, only positive MR is observed from low fields and on. This behavior is opposite to the behavior of MR in more isolating samples (in Mott's regime). Recall that the MR in this case was always negative in low fields and its amplitude increased with lowering temperature.

Let us now discuss the positive MR due to the shrinkage of wave functions in a magnetic field. The experimental temperature dependences of the corresponding positive MR are shown for two samples in Fig. 3. According to [10], the contribution in the case of variable-range hopping conduction over the Coulomb-gap states is given by

$$\ln\left(\frac{R(H)}{R(0)}\right) = K\left(\frac{T_1}{T}\right)^{3/2}\left(\frac{eHa}{ch}\right),$$

where $K = 0.002$ is a numerical factor.

Figure 4 presents the temperature dependences of the curve slopes for the quadratic positive MRs of two samples; the dashed lines correspond to the $T^{-3/2}$ and T^{-1} laws (corresponding to the positive MR in the Mott's regime). One can see that the experimental behavior is closer to the $T^{-3/2}$ law rather than to T^{-1} (as was the case for the conductance in the Mott's law). This fact con-

firms once more that the conduction occurs over the Coulomb-gap states. The radius a of the states between which hopping occurs was estimated from the slope of this curve and found to be 16 and 17 nm for samples 1 and 2, respectively. Note that $a \sim T_1^{-3/8}$; i.e., the dependence on T_1 is rather weak.

DISCUSSION

Thus, measurements of the temperature dependences of conductance and positive quadratic magnetoresistance have demonstrated that, as the impurity (in our case, A^+-center) concentration increases, the transition occurs from Mott's hopping conduction to conduction over the Coulomb-gap states. This is caused both by an increase in the density of states at the Fermi level and by an increase in the localization radius [see Eq. (1)]. The calculated pre-exponential factor is close to its universal value that was observed in a number of works [8].

The localization radius a can be estimated directly from Eq. (2) by determining T_1 from the temperature dependences and assuming that κ = const = 12 and C = 6.2. This yields a = 500 nm. A comparison of the localization radii estimated from the T_1 values and from the quadratic magnetoresistance, on the assumption that the dielectric constant is equal to its value beyond the metal–insulator transition region, shows that the agreement between the two values is achieved if the coefficient C is taken to be smaller by a factor of 30 than its theoretical estimate.

This fact can be caused by two reasons. First, a decrease in C may be due to the contribution from the correlated hopping. The corresponding behavior was discussed in a number of works [6]. Second, the fact that the dielectric constant in the vicinity of metal–insulator transition is the same as beyond it is questionable for the systems studied. The point is that the corresponding conclusion was formulated for purely 2D systems. In our case, we deal with the quantum well structures. Estimates show that, at least at low temperatures, the hopping distance is comparable with the structure thickness. In other words, one can expect that almost all wells in the structure can be involved in the screening of electron–electron interaction in each of the wells, so that the system is close to three-dimensional in this respect.

Let us now discuss the above-mentioned suppression of negative magnetoresistance in our structures. We first note that similar effect in the hopping conduction over the Coulomb-gap states in 3D samples was observed by us earlier. It is well known that the respective contribution to the magnetoresistance is caused by the interference of different hopping trajectories including underbarrier scattering events. We have proposed a model that explains the observed behavior by a decrease in the concentration of scatterers upon the transition to the Coulomb-gap regime [11]. It is worth noting that our model assumes that the scattering is weak, whereas the model with purely coulombic scattering [12] leads to a universal law for the negative magnetoresistance, in conflict with our experimental data. It should be emphasized that the noncoulombic scattering character in our situation can be explained by the fact that the potential of a neutral center with respect to the hopping hole is by no means coulombic.

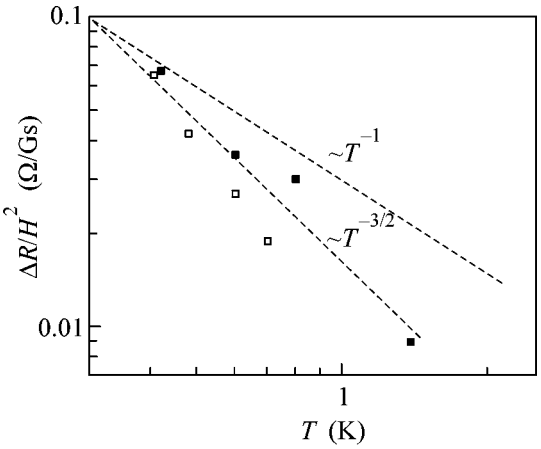

Fig. 4. Temperature dependence of the slope of a linear portion in the curve of quadratic positive magnetoresistance.

CONCLUSION

Summarizing the obtained results, we note that the conduction in the systems with high impurity concentration (close to the metal–insulator transition) proceeds over the states in the Coulomb gap. Furthermore, the coefficient in the Efros–Shklovskiĭ law proves to be 30 times smaller than follows from the Efros–Shklovskiĭ theory. This may be due both to the correlated hopping and to the contribution from the Coulomb interaction between wells. Finally, the suppression of negative magnetoresistance has been observed in the Efros–Shklovskiĭ conduction regime. Such a behavior may be caused by the weakness of underbarrier scattering in the hopping over the states of the upper Hubbard band.

This work was supported by the Russian Foundation for Basic Research, project no. 00-02-16992.

REFERENCES

1. E. Abrahams, S. V. Kravchenko, and M. P. Sarachik, Rev. Mod. Phys. **73**, 251 (2001).
2. V. I. Kozub and N. V. Agrinskaya, Phys. Rev. B **64**, 245103 (2001).
3. N. V. Agrinskaya, Yu. L. Ivanov, V. M. Ustinov, and D. A. Poloskin, Fiz. Tekh. Poluprovodn. (St. Petersburg) **35**, 571 (2001) [Semiconductors **35**, 550 (2001)]; N. V. Agrinskaya, V. I. Kozub, Yu. L. Ivanov, *et al.*, Zh. Éksp. Teor. Fiz. **120**, 480 (2001) [JETP **93**, 424 (2001)].

4. D. G. Polyakov and B. I. Shklovskii, Phys. Rev. B **48**, 11167 (1993).
5. T. G. Castner, *Hopping Transport in Solids*, Ed. by M. Pollak and B. Shklovskii (North-Holland, Amsterdam, 1991), p. 1.
6. F. W. van Keuls, X. L. Hu, H. W. Jiang, and A. J. Dahm, Phys. Rev. B **56**, 1161 (1997).
7. I. L. Alenier, D. G. Polyakov, and B. I. Shklovskii, in *Proceedings of the 22nd International Conference on the Physics of Semiconductors, Vancuver, 1994* (World Scientific, Singapore, 1994), p. 787.
8. I. Shlimak and M. Pepper, Philos. Mag. B **81**, 1093 (2001).
9. A. V. Buyanov, A. C. Ferreira, E. Soderstrom, *et al.*, Phys. Rev. B **53**, 1357 (1996).
10. Ngyen Van Lien, Phys. Lett. A **207**, 379 (1995).
11. N. V. Agrinskaya, V. I. Kozub, and D. V. Shamshur, Zh. Éksp. Teor. Fiz. **107**, 2063 (1995) [JETP **80**, 1142 (1995)].
12. M. E. Raikh and G. F. Wessels, Phys. Rev. B **47**, 15609 (1993).

Translated by V. Sakun

JETP Letters, Vol. 76, No. 6, 2002, pp. 365–369. Translated from Pis'ma v Zhurnal Éksperimental'noĭ i Teoreticheskoĭ Fiziki, Vol. 76, No. 6, 2002, pp. 425–429.

Low-Energy Photoluminescence of Structures with GeSi/Si(001) Self-Assembled Nanoislands

N. V. Vostokov, Yu. N. Drozdov, Z. F. Krasil'nik, D. N. Lobanov, A. V. Novikov, and A. N. Yablonskiĭ

Institute for the Physics of Microstructures, Russian Academy of Sciences, Nizhni Novgorod, 603950 Russia

dima@ipm.sci-nnov.ru

Received July 29, 2002

The photoluminescence spectra of structures with self-assembled GeSi/Si(001) islands are investigated as functions of the growth temperature. It is shown that the shift of the peak of photoluminescence from islands toward lower energies on decreasing the growth temperature is due to the suppression of Si diffusion into islands and an increase in the fraction of Ge in islands. A photoluminescence signal from the GeSi islands is found in the region of energies down to 0.6 eV, which is considerably smaller than the band-gap width in bulk Ge. The position of the peak of photoluminescence from islands is described well by the model of a real-space indirect optical transition with account of the real composition and elastic strains of the islands. Mono- and multilayer structures are obtained with self-assembled GeSi/Si(001) nanoislands exhibiting a photoluminescence signal in the region 1.3–2 μm at room temperature. © *2002 MAIK "Nauka/Interperiodica".*

PACS numbers: 78.55.Ap; 78.67.Hc

In the last few years, interest has considerably increased in various kinds of low-dimensional systems on silicon substrates. This interest is associated with the possibility of creating light-emitting devices and photodetectors based on these systems. One of the lines actively developed in this area is $Si_{1-x}Ge_x$/Si(001) heterostructures with self-assembled nanoislands and quantum dots. An intense photoluminescence (PL) band is observed in such structures in the region of wavelengths λ = 1.3–1.6 μm (0.75–0.95 eV) [1], which is of great practical importance for information transfer and reception with the use of optical-fiber transmission lines.

One of the theoretical models [2] relates the appearance of the given signal of PL from islands with the real-space indirect radiative recombination of holes localized in islands and electrons located in Si at the II kind heteroboundary with an island. According to the model [2], the indirect optical transition must be observed in structures with Ge/Si(001) self-assembled islands down to energies of ~0.4 eV (~3 μm), which is considerably lower than the band gap width of not only bulk Si but also bulk Ge. However, so far, the PL line from islands has been observed in the region of energies 0.75–0.95 eV [3], which is smaller than the band gap of Si but larger than the band gap of Ge. One of the reasons for the given discrepancy between the theory and experiment for the structures grown at germanium deposition temperatures above 550°C is the formation of a GeSi alloy in islands due to Si diffusion into islands accelerated by elastic stresses [4]. The formation of a GeSi alloy in the islands is often disregarded in the description of optical and electrophysical properties of structures with nanoislands, which leads to an incorrect interpretation of experimental data.

In this work, the PL spectra of mono- and multilayer structures with GeSi/Si(001) self-assembled nanoislands grown at various Ge deposition temperatures are analyzed with account of the real island parameters, namely, sizes, composition, and elastic strains.

The structures to be studied were grown on Si(001) substrates by molecular-beam epitaxy from solid sources. The structures with self-assembled nanoislands comprised a buffer Si layer and a Ge layer with an equivalent thickness of from five to ten monolayers (ML, 1 ML ≈ 0.14 nm). The deposition of Ge was carried out at temperatures T_g = 600, 700, and 750°C. The structures for photoluminescence measurements had a capping Si layer, whose growth was carried out at the same temperatures as the deposition of Ge. Multilayer structures were grown at T_g = 600 and 700°C and consisted of five periods of Ge layers with an equivalent thickness of 7.5 ML separated by spacing silicon layers 30 and 60 nm thick, respectively. The morphology of the structure surfaces was studied on a Solver P4 atomic force microscope (AFM) and x-ray diffraction (XRD) studies were carried out on a DRON-4 diffractometer. The PL spectra of GeSi heterostructures were recorded by a BOMEM DA3.36 Fourier spectrometer. Cooled Ge and InSb detectors were used for measuring the spectra. An Ar^+ laser (line 514.5 nm) was used for PL excitation.

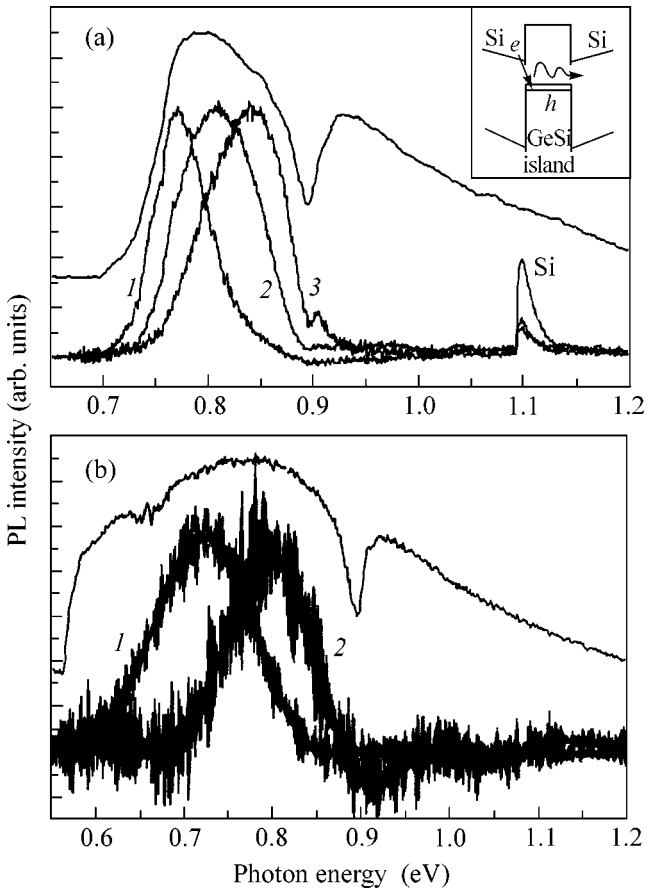

Fig. 1. PL spectra of structures grown at (*1*) 600°C, (*2*) 700°C, and (*3*) 750°C recorded at 77 K with the use of (a) Ge and (b) InSb detectors. The upper curves in the figures correspond to the spectral characteristics of the detectors. The dip at 0.9 eV is associated with absorption in the fused-silica window of the Fourier spectrometer. All the spectra are normalized to the maximum of the PL signal from the islands. The model of an indirect optical transition in the GeSi islands is schematically depicted in the inset (see text).

Studies of the growth of GeSi nanoislands performed previously at various Ge deposition temperatures showed [4, 5] that a GeSi alloy forms in nanoislands at $T_g \geq 600$°C immediately in the process of Ge deposition. On decreasing T_g from 750 down to 600°C, the fraction of Ge in the islands increases, which leads to a decrease in the size of islands [4, 5]. According to AFM studies, the size of dome islands in the growth plane decreases from 200–250 nm down to 60–80 nm and their height decreases from 30–35 nm down to 10–12 nm as T_g decreases from 750 down to 600°C [4, 5]. At the same time, according to x-ray diffraction and Raman spectroscopy data, the fraction of Ge in nonovergrown dome islands increased from x = 40–50% for T_g = 750°C to x = 70–75% for T_g = 600°C [4, 5]. The formation of a GeSi solution in the islands is associated with Si diffusion accelerated by nonuniform fields of elastic strains (RES) from the islands [6]. The magnitude of the residual elastic strains of nonovergrown dome islands was in the range RES = 50 ± 10% and was independent of the growth temperature. The absence of the dependence of RES on T_g is due to the fact that the shape of dome islands (the ratio of height to lateral size), which in many respects determines the extent of the relaxation of elastic strains in these islands, is independent of the Ge deposition temperature. When the islands are overgrown at high temperatures (T_g > 500°C), the height of the islands decreases [7] and the fraction of Si in the islands increases [4]. According to the data of an x-ray diffraction analysis of the reciprocal space in the vicinity of (004) and (404) reflections from the Si substrate, the mean Ge concentration in the islands in multilayer structures decreases from x = 48 ± 5% to x = 36 ± 5% on increasing the growth temperature from T_g = 600 to 700°C. The obtained fractions of Ge in the overgrown islands in multilayer structures are significantly lower than the fraction of Ge in nonovergrown islands. The magnitude of residual elastic strains in islands, regardless of the growth temperature, comprises RES = 80 ± 20%. An increase in RES in islands during overgrowth is due to the fact that the free island surface, on which the relaxation of a significant part of elastic strains in nonovergrown structures occurs, disappears as the cover layer of Si grows.

The variation of the island composition as the Ge deposition temperature increases are revealed in PL spectra (Fig. 1). In the PL spectra of structures with nanoislands measured at 77 K using a Ge detector (Fig. 1a), a wide PL band is observed in the region 0.7–0.9 eV in addition to the PL line at 1.1 eV associated with the radiative recombination of a free exciton in Si. The appearance of the given PL band is due to a real-space indirect optical transition between holes localized in islands and electrons that occur in Si at the II type heterojunction with an island [2]. This indirect optical transition is depicted schematically in the inset in Fig. 1a, in which the positions of 2Δ valleys of the conduction band and the level of heavy holes in the vicinity of a GeSi island are shown. It is evident from the PL spectra (Fig. 1a) that the PL peak maximum shifts toward the region of lower energies on decreasing the growth temperature. This shift of the PL peak from the islands is due to an increase in the fraction of Ge in the islands on decreasing the growth temperature [4, 5]. As the fraction of Ge in the islands increases, the discontinuity of valence bands at the silicon–island heterojunction increases and, as a consequence, the indirect optical transition energy in the islands decreases (see inset in Fig. 1a).

The PL spectra recorded with the use of a Ge detector (Fig. 1a) indicate that the low-energy edge of the PL signal from the islands grown at T_g = 600°C is determined by the limit of the spectral characteristic of the given detector. The PL spectra of structures measured at 77 K with the use of a InSb detector (Fig. 1b) showed

that a significant part of the PL signal from the islands grown at T_g = 600°C is located in the region of energies that are significantly smaller than the band gap width of bulk Ge (E = 0.735 eV at 77 K). The existence of the PL signal from islands in the region of energies that are smaller than the band-gap width of bulk Ge can serve as a corroboration of the model [2], which relates the peak of PL from islands with a real-space indirect optical transition. It should be noted that the maximum sensitivity of the InSb detector is more than two orders of magnitude lower than the sensitivity of the Ge detector.

A comparative analysis of the PL spectra of mono- and multilayer structures with islands grown at T_g = 600 and 700°C showed (Fig. 2) that, in addition to significant enhancement of the PL signal from the islands, the peak of PL from the islands in multilayer structures shifts by 15–25 meV toward higher energies. This shift of the peak of PL from the islands is associated with the decrease in the mean concentration of Ge in the islands due to Si diffusion from the barrier layers into the islands during the growth of the multilayer structures, whose duration is longer as compared to the growth of monolayer structures. In the study of multilayer structures with GeSi/Si(001) islands by electron microscopy [8], it was shown that the concentration of Ge in the islands decreases with increasing depth of the layer of islands. This is connected with the fact that the time it takes for the interdiffusion of atoms in lower layers of multilayer structures is longer than that for upper layers. It may be suggested that the composition of islands in monolayer structures corresponds to the composition of islands in the upper layers of multilayer structures, because the growth conditions (temperature and growth time of the capping Si layer) for these layers are similar. The concentration of Ge in the islands of the upper layers of multilayer structures is higher than that averaged over all layers [8]; therefore, the fraction of Ge in the islands of monolayer structures is higher than that in multilayer structures. It is the decrease in the mean concentration of Ge in the islands of multilayer structures compared to the concentration in monolayer structures that leads to the shift of the peak of PL from islands toward the region of higher energies found experimentally. The dependence of the composition of islands on their depth is also responsible for the broadening of the peak of PL from the islands in multilayer structures (Fig. 2). The line width of PL from the islands in multilayer structures increases in spite of the decrease in the size spread of the islands and their spatial ordering observed in multilayer structures [9]. It is evident that the peak width of PL from the islands in the structures under study is determined by the difference in the composition of islands located in different layers rather than the size spread of the islands.

As mentioned above, the mean concentration of Ge and the extent of relaxation of elastic strains have been determined in the islands of multilayer structures. According to the results of x-ray diffraction analysis,

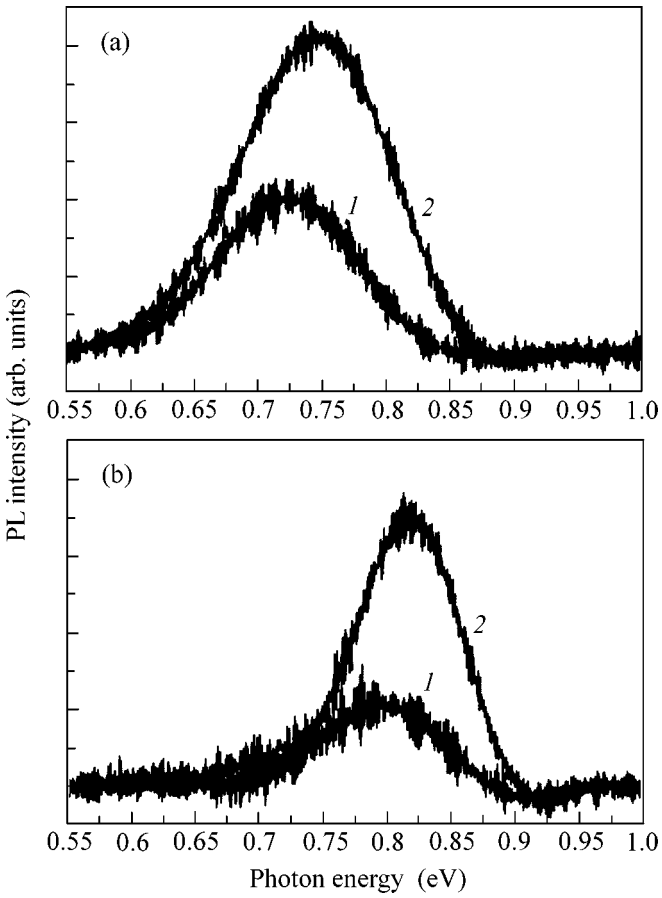

Fig. 2. PL spectra of (*1*) mono- and (*2*) multilayer structures with nanoislands grown at (a) 600°C and (b) 700°C. The spectra were recorded at 77 K using an InSb detector.

the mean concentration of Ge in the islands decreases from $x = 48 \pm 5\%$ down to $x = 36 \pm 5\%$ on increasing the growth temperature from T_g = 600 up to 700°C. Given the composition and elastic strain of the islands, the position of energy bands can be estimated in the vicinity of the islands. In the calculations, the layer of islands was considered as a uniformly strained layer whose thickness and composition corresponded to the height and composition of the islands. This approximation is possible, because according to AFM data the lowest size of the dome islands in the growth plane of the structures under study was >50 nm and exceeded their height by a factor of five. The change in the position of the energy bands of Si in the vicinity of an island due to the propagation of the fields of elastic strains from the islands to the Si layers (see inset in Fig. 1a) was taken into account in the calculations. According to the calculations, the energy of the real-space direct optical transition associated with the recombination of electrons and holes localized in the islands must comprise $E = 0.83 \pm 0.05$ eV for T_g = 600°C and $E = 0.89 \pm 0.04$ eV for T_g = 700°C. The energies obtained are

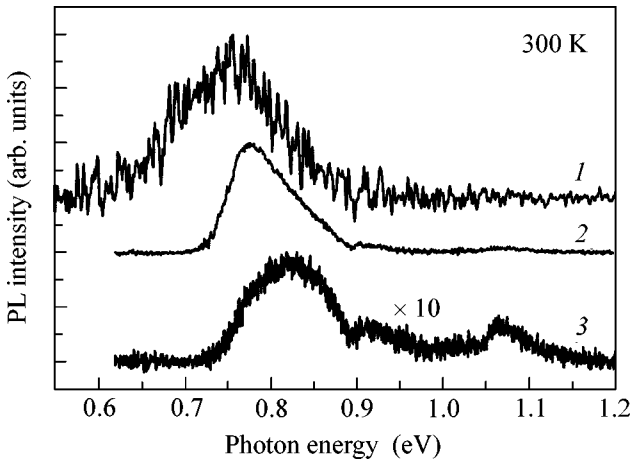

Fig. 3. PL spectra of multilayer structures with nanoislands grown at (*1* and *2*) 600°C and (*3*) 700°C measured at room temperature using (*1*) InSb and (*2* and *3*) Ge detectors. The spectra were recorded at an optical pump power of 50 W/cm^2.

higher than the energies at which the photoluminescence signal from the islands is observed. At the same time, the calculated energies of the real-space indirect optical transition between holes localized in the islands and electrons located in Si (see inset in Fig. 1a) comprise $E = 0.76 \pm 0.05$ eV for $T_g = 600$°C and $E = 0.86 \pm 0.04$ eV for $T_g = 700$°C. These energy values agree well with the position of the peaks of PL from the islands in multilayer structures (Fig. 2), which corroborates the model [2], which relates the PL signal from islands with the real-space indirect optical recombination of charge carriers.

The calculations of the band diagram of structures with islands showed that the discontinuity of the valence bands at the Si–island heterojunction, depending on the growth temperature, comprises from 250 meV (for $T_g = 700$°C) up to 350 meV (for $T_g = 600$°C). These energy values by more than an order of magnitude exceed the thermal energy that the charge carriers possess at room temperature (25 meV). Because of this, a significant part of holes remain localized in the islands even at room temperature. In the structures studied, the PL signal from the islands was observed down to room temperature (Fig. 3). For a multilayer structure grown at $T_g = 600$°C, a significant part of the PL signal from islands is arranged in the region of energies lower than the band gap width of bulk Ge (curve *1* in Fig. 3). The intensity of the PL signal from the islands formed at $T_g = 600$°C is approximately an order of magnitude higher than the intensity of the PL signal from the islands grown at $T_g = 700$°C (Fig. 3). The higher intensity of the PL signal from the islands grown at $T_g = 600$°C is due to the better localization of holes in the islands grown at a lower temperature and, hence, having smaller sizes, a higher concentration of Ge, and a larger discontinuity of valence bands at the heterojunction with Si. A decrease in the concentration of Ge in the islands on increasing the growth temperature also leads to a decrease in the potential well for electrons, which is located in Si at the heterojunction with an island (see inset in Fig. 1a). The potential well for electrons is due to the penetration of elastic strains from the islands into the Si layers, and its depth increases with increasing mismatch between the crystal lattices of Si and of the island. Because, according to x-ray diffraction data, the magnitude of the residual elastic strains is independent of the growth temperature, the mismatch between the Si and island crystal lattices will be higher for the islands that have a larger Ge concentration. Hence, the potential well for electrons will also be higher at the islands containing a larger fraction of Ge.

A comparison of the PL spectra of structures recorded at 77 and 300 K (Figs. 1 and 3) indicate that the position of the line of PL from islands exhibits a weaker dependence on the growth temperature than the position of the PL line associated with the optical recombination of a free exciton in Si. This is associated with the fact that the decrease in the width of the band gap on increasing the measurement temperature is compensated by an increase in the hole populations of the excited states in the islands. The high-energy optical recombination of holes from these levels leads to a weak temperature dependence of the position of the PL signal due to islands.

Studies of the PL spectra of mono- and multilayer GeSi structures with nanoislands have been carried out in this work, depending on the growth temperature. It is shown that the peak of PL from the islands shifts toward the region of lower energies on decreasing the growth temperature. This shift is due to the suppression of Si diffusion into the islands and an increase in the fraction of Ge in the islands on decreasing the growth temperature. For structures with nanoislands grown at 600°C, a signal of PL from the islands has been found at energies smaller than the band gap width of bulk Ge. The shift of the peak of PL from the islands to the region of higher energies in multilayer structures as compared to monolayer ones is related to the decrease in the mean concentration of Ge in the islands in the case of longer growth of multilayer structures. With regard to the real composition and elastic strains of the overgrown islands, the position of the peak of PL from the islands is described well by the model of a real-space indirect optical transition between holes localized in the islands and electrons located in Si at the II type heterojunction with an island. Structures with GeSi/Si(001) self-assembled nanoislands have been obtained that have a PL signal in the region 1.3–2 μm up to room temperature, which open a way of creating light-emitting diode structures based on silicon technology in the wavelength region ~1.55 μm of practical interest.

This work was supported by the Russian Foundation for Basic Research (project nos. 00-02-16141 and 02-02-16792), the Program of Support of the Leading Scientific Schools of the Russian Federation (project no. 00-15-966118), and programs of the Ministry of Science and Technology of the Russian Federation.

REFERENCES

1. H. Sunamura, N. Usami, Y. Shiraki, and S. Fukatsu, Appl. Phys. Lett. **66**, 3024 (1995).
2. V. Ya. Aleshkin, N. A. Bekin, N. G. Kalugin, *et al.*, Pis'ma Zh. Éksp. Teor. Fiz. **67**, 46 (1998) [JETP Lett. **67**, 48 (1998)].
3. K. Eberl, M. O. Lipinski, Y. M. Manz, *et al.*, Physica E (Amsterdam) **9**, 164 (2001).
4. A. V. Novikov, B. A. Andreev, N. V. Vostokov, *et al.*, Mater. Sci. Eng. B **89**, 62 (2002).
5. M. Ya. Valakh, N. V. Vostokov, S. A. Gusev, *et al.*, Izv. Akad. Nauk, Ser. Fiz. **66** (2), 160 (2002).
6. S. A. Chaparro, J. Drucker, Y. Zhang, *et al.*, Phys. Rev. Lett. **83**, 1199 (1999).
7. P. Sutter, E. Mateeva, J. S. Sullivan, and M. G. Lagally, Thin Solid Films **336**, 262 (1998).
8. X. Z. Liao, J. Zou, D. J. H. Cockayne, *et al.*, Appl. Phys. Lett. **79**, 1258 (2001).
9. J. Tersoff, C. Teichert, and M. C. Lagally, Phys. Rev. Lett. **76**, 1675 (1996).

Translated by A. Bagatur'yants

JETP Letters, Vol. 76, No. 6, 2002, pp. 370–373. Translated from Pis'ma v Zhurnal Éksperimental'noĭ i Teoreticheskoĭ Fiziki, Vol. 76, No. 6, 2002, pp. 430–433.

Quantum Frequency Standards Based on the Soliton State of a Bose–Einstein Condensate

Yu. V. Rozhdestvenskii, N. N. Rozanov*, and V. A. Smirnov

Research Institute of Laser Physics, St. Petersburg, 199034 Russia

** e-mail: rosanov@ilph.spb.su*

Received July 29, 2002

A method for stabilizing frequency based on using the soliton state of the Bose–Einstein condensate of alkali metal atoms as an atomic source was suggested. The critical total number of lithium condensate particles at which the existence of a quasi-one-dimensional soliton in the condensate was possible and the lifetime of such a soliton were estimated. The attainable accuracy of measuring reference transition frequencies in the suggested standard was shown to be substantially higher than with the known quantum frequency standards. © *2002 MAIK "Nauka/Interperiodica".*

PACS numbers: 03.75.Fi; 06.30.Ft; 06.20.Fn

Recent observations of the soliton states of ^{7}Li atoms in a cylindrical optical trap [1, 2] (also see the theoretical analysis in [3–5]) open up new possibilities of controlling the spatial movement of the Bose–Einstein condensate and substantially broaden the range of possible physical applications of this macroscopic quantum object.

One of the most important uses of such soliton states is frequency stabilization and the development of the corresponding fundamentally new quantum standards. The obvious advantage of using Bose–Einstein condensate soliton states as an atomic source in quantum frequency standards is a substantial increase in measurement time τ and the ensuing decrease in the error of frequency measurements $\delta\omega \approx 1/\tau$ at comparatively small linear device dimensions. For instance, in experiments performed in [1], the lifetime of stable one-dimensional Bose–Einstein condensate soliton states of lithium atoms was longer than 3 s. At a ~1 cm/s velocity of such a soliton and an $L_i \approx 10$ cm size of the region of interactions between atoms and a radiofrequency field, the error in frequency measurements would $\delta\omega \sim 0.05$ Hz, which is almost two orders of magnitude lower than the measured reference transition widths. For instance, the modern primary cesium standard is characterized by a $\delta\omega \approx 3$ Hz error in frequency measurements at typical flight velocity $\langle V\rangle \approx 10^4$ cm/s and path length $L < 5 \times 10^2$ cm [6].

A schematic diagram of a quantum frequency standard using the stable soliton state of the Bose–Einstein condensate of lithium atoms as an atomic source is shown in the figure. Initially, the Bose–Einstein condensate is formed in a magnetic trap [in the (2, 2) state, where the first number is the total atomic spin and the second, its projection]. The condensate is then injected into a magnetic waveguide (which can, for instance, consist of two current-carrying conductors [7]) at a 1–5 mm/s velocity. The spatial extension of such a soliton along the waveguide axis is determined by the total number of atoms in the Bose–Einstein condensate, and its cross section, by the frequencies of oscillations in the magnetic potentials of the current-carrying conductors. At the initial concentration of atoms in the condensate above some critical value and a negative scattering length, the soliton state of the Bose–Einstein condensate of lithium atoms is formed. The lifetime of this state is determined by two main factors: two-particle collisions of condensate atoms and residual gas pressure.

Further, while the soliton moves along the magnetic waveguide, Bose–Einstein condensate atoms interact with a radiofrequency field tuned to the reference transition frequency (for alkali metal atoms, the transition between the hyperfine structure sublevels is used). Because, initially, atoms in the condensate are in the (2, 2) state, the interaction with the radiofrequency field causes the transition of some part of atoms to the lower hyperfine structure state with a change in the magnetic moment projection. As a result, these atoms are no longer confined with the magnetic field and leave the condensate region. All atoms that shift to the lower state under field action and leave the magnetic waveguide fall straight down and are recorded, for instance, by a surface ionization detector of the usual cesium standard. The number of atoms that leave the condensate can be used to determine the probability of the radiofrequency transition, which, in turn, depends on the frequency difference between the applied radiofrequency field and the reference transition. The detector is, however, reached not only by the atoms that change spins as a result of absorbtion of radiofrequency quanta, but also by the atoms whose spins change because of pair colli-

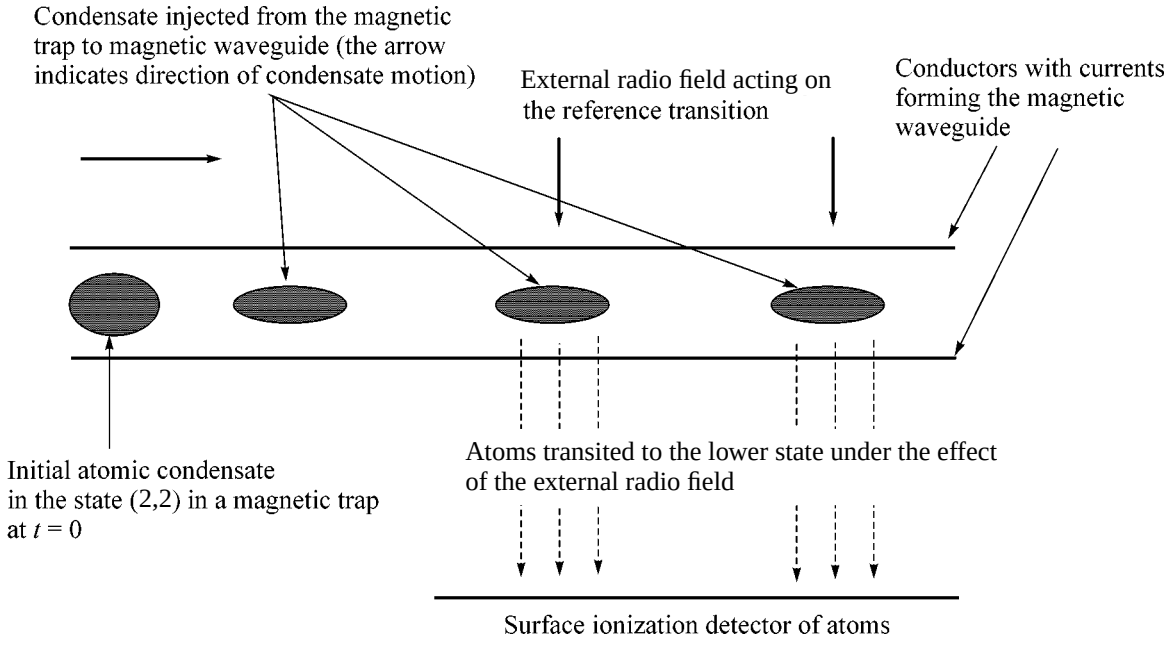

Schematic diagram of a quantum frequency standard based on the soliton state of a Bose–Einstein condensate.

sions, which is an important factor directly influencing the accuracy of frequency measurements. This difficulty can be overcome by calibrating the measuring system (against the data obtained in the absence of a radiofrequency field).

The construction of a quantum standard based on Bose–Einstein condensate soliton states requires considering the conditions of formation and propagation of such quasi-one-dimensional soliton states in a magnetic waveguide [7]. Such a soliton distribution of a Bose–Einstein condensate is formed along waveguide z axis, whereas, in the transverse direction, the condensate is confined in the two-dimensional potential well

$$U = \frac{M}{2}(\alpha_x\omega_x^2x^2 + \alpha_y\omega_y^2y^2), \quad (1)$$

where M is the mass of the atom, x and y are the transverse coordinates of the particle in the potential well, $\alpha_{x,y}$ are the coupling constants along the x and y axes, and $\omega_{x,y}$ are the oscillation frequencies.

The Gross–Pitaevski equation for a one-particle wave function of atoms with a negative scattering length in a directing (along z axis) magnetic waveguide with the transverse confinement potential U has the form

$$i\hbar\frac{\partial\Psi}{\partial t} = -\frac{\hbar^2}{2M}\Delta\Psi + U\Psi - \frac{4\pi\hbar^2a}{M}N|\Psi|^2\Psi, \quad (2)$$

where a is the absolute scattering length value and N is the total number of atoms in the condensate. An approximate normalized wave function of the condensate in the normal state has the form [8]

$$\Psi_0 = \frac{\sqrt{B/2}}{\cosh(Bz)}\chi_0(x)\chi_0(y)\exp(-i\gamma t), \quad (3)$$

where χ_0 is the wave function of the normal state of the harmonic oscillator corresponding to potential (1) and the B and γ constants are determined by the equations

$$\gamma = \frac{\hbar}{2M}B^2, \quad B = a\frac{M\sqrt{\omega_x\omega_y}}{\hbar}N. \quad (4)$$

The natural spreading of the wave function of Bose–Einstein condensate atoms is balanced by effective nonlinear contraction in the soliton state [the last term in the right-hand side of (2)]. In the absence of such balancing [if the nonlinear term in (2) is small], the wave function spreads with the characteristic time

$$\tau_d = M/2\hbar B^2. \quad (5)$$

Note that one-dimensional solitons are stable with respect to perturbations of their profiles. Such perturbations can be caused, for instance, by nonuniformities of the magnetic waveguide confinement field, and the decay time of these perturbations is also determined by (5). Because of the loss of atoms as a result of spin–spin interactions in pair collisions and in collisions with background atoms, the concentration of atoms in Bose–Einstein condensates decreases as time passes. This eventually results in soliton decay. A maximum concentration of atoms is reached in the soliton center,

$$N_c^m = N|\Psi(x, y, z = 0)|^2 = B^2/2\pi a. \quad (6)$$

This value also determines soliton length $L = 2/B$.

The condensate can only exist at fairly high concentrations of atoms. The most stringent restrictions on the soliton length and, accordingly, the concentration of atoms in it arise from the requirement $T < T_c$, where T_c is the critical temperature [9],

$$kT_c = \frac{\sqrt{2}\hbar}{M}\left(\frac{N}{1.2}\right)^{1/3}\left(\frac{2\hbar B^4}{M}\right)^{1/6}\left(\frac{M\omega^2}{2}\right)^{1/3} = 1.1\sqrt{\pi}a^{1/6}\left(\frac{2\hbar}{M\omega}\right)^{2/3}\hbar\omega\sqrt{N_c^m}. \quad (7)$$

In (7), the transverse frequencies are assumed to be equal to each other ($\omega_x \approx \omega_y = \omega$), and the oscillation frequency along the z axis in our problem is determined by soliton length L. For the lithium condensate with $a = 1.43 \times 10^{-7}$ cm [9] and the transverse oscillation frequency $\omega = 1.6 \times 10^2$ Hz [7], the condition $T < T_c$ gives $N_c^m > 10^{13}$ cm^{-3}. We then have $B > 3 \times 10^3$ cm^{-1}; that is, the maximum soliton length is $L_m = 7$ μm, and the total number of atoms in the condensate is $N > N_{\min} = 2 \times 10^3$. These values determine the limiting soliton parameters.

The soliton lifetime is determined by the rate at which the number of particles in the Bose–Einstein condensate decreases. In the absence of external actions, the main reason for this decrease is interactions of electron spins in pair collisions of atoms. These interactions cause simultaneous spin flip and the falling out of atoms from the condensate. The rate of this process is $\langle\sigma V\rangle = 5 \times 10^{-15}$ cm^3/s (σ is the cross section and V, the velocity of atoms) [10]. Atomic concentration changes in a Bose–Einstein condensate are described by the equation

$$\partial n/\partial t = -2n^2\langle\sigma V\rangle, \quad (8)$$

where $n = N|\Psi_0|^2$. According to estimate (5), wave function perturbations decay fairly rapidly ($\tau_d \sim 10^{-2}$ s). The soliton then broadens adiabatically, which allows the ratio between the B and N functions to be conserved [see (4)] at an arbitrary instant of time. The integration of (8) in spatial coordinates yields the equation for the total number of atoms in the Bose–Einstein condensate

$$\frac{1}{N^3}\frac{dN}{dt} = -\frac{2}{3}\left(\frac{M\omega}{\hbar}\right)^2 a\langle\sigma V\rangle. \quad (9)$$

The solution to (9) describes a decrease in concentration N in time,

$$t = \frac{3}{4}\left(\frac{1}{N^2} - \frac{1}{N_i^2}\right)\left[\left(\frac{M\omega}{\hbar}\right)^2 a\langle\sigma V\rangle\right]^{-1}, \quad (10)$$

where N_i is the initial number of atoms. Estimating the lifetime of the soliton t_m as the time of decreasing the number of atoms to the critical value $N_{\min} = 2 \times 10^3$ (see above), we obtain $t_m \approx 50$ s for the lithium condensate on the condition that $N_i \gg N_{\min}$. It follows that the time during which the soliton state of the Bose–Einstein condensate of Li atoms can be observed can reach ~50 s, which corresponds to a $\delta\omega \approx 0.003$ Hz error in reference transition frequency measurements.

At the same time, because of the peculiar "Mössbauer effect," the absorption of light by condensate atoms becomes collective [11] if the recoil velocity in the absorption of a quantum is much lower than the velocity of sound in the condensate, and it certainly is for transitions between hyperfine structure levels. As a result, the absorption line shifts by a value that depends on the number of particles in the condensate. Let us estimate this shift by (4) from the γ value, which determines the initial soliton state of the Bose–Einstein condensate. At the parameters used above, $\gamma > 400$ s^{-1}, and the rate of frequency variations amounts to $\dot{\gamma} \approx 10^{-2}$ s. To use the device under consideration as a primary frequency standard, the drift of the reference transition frequency during ~50 s of measurements should not exceed $\delta\omega \approx 1/50$ s^{-1} = 0.003 Hz, which corresponds to the rate of frequency variations $\dot{\gamma} \leq 10^{-3}$ s^{-2}. Such frequency stabilization can be attained in a Bose–Einstein condensate of ^{7}Li atoms in the (2, 2) state by decreasing the temperature of the condensate to $T = 10^{-8}$ K. Using (4), (6), and (7), we can also show that such a decrease in temperature decreases the number of atoms in the condensate to $N = 300$.

A modification of the method for frequency stabilization described above is the formation of soliton structures in Bose–Einstein condensates of ^{7}Li atoms in the (1, 1) state by means of the Feshbach resonance [1, 2]. The advantage of forming soliton structures in such a state stems from the virtual impossibility of the transition to the excited state. The lifetime of atoms in the condensate is therefore only determined by their loss as a result of three-particle collisions. Suppose that each collision of atoms in a sphere of radius r_c, which is determined from the elastic scattering cross section, causes two atoms to fall out of the condensate. According to [12], the decay rate is then given by the equation

$$dN_c^m/dt = -1.44Vr_c^5N_c^{m^3}. \quad (11)$$

With the atomic scattering length $-a = -1.6 \times 10^{-8}$ cm [1], we then obtain the rate of reference transition frequency shifting $\dot{\gamma} = \hbar\pi|a|\dot{N}_c^m/M = 10^{-3}$ s^{-2}, which corresponds to a ~50 s time of frequency measurements.

The measuring scheme shown in the figure should be modified to use the (1, 1) state of the Bose–Einstein condensate of lithium atoms as a frequency standard. Lithium atoms in the (1, 1) state cannot be confined with a magnetic trap; therefore, an optical trap similar to that described in [1, 2] should be used. After the formation of a condensate of atoms in the (2, 2) state in a magnetic trap, the condensate can be transferred to an

optical trap formed by a laser beam. In this trap, the condensate in the (2, 2) state quickly and virtually completely transforms into the condensate in the (1, 1) state under the action of a strong radiofrequency field, and, by means of the Feshbach resonance, a Bose–Einstein condensate soliton state is formed. After interacting with a fairly weak measuring radiofrequency field, which excites some part of atoms to the (2, 2) state, the condensate returns to the magnetic trap, where atoms in the (1, 1) state are sifted out, and (2, 2) atoms excited to the higher state only remain. The number of these atoms constitutes the measurement signal.

Above, our estimates were made for the characteristics of Li atoms. The use of the Feshbach resonance [1], however, allows the magnitude and sign of the scattering lengths of some other alkali metal atoms (Na, Rb, and Cs) to be controlled. The suggested frequency standard can be optimized by studying the possibility of the existence of stable soliton states in these gases.

To summarize, we showed the possibility in principle of using the atomic reference transition of the Bose–Einstein condensate soliton states for measuring frequencies, which makes it possible to substantially improve the characteristics of quantum frequency standards with the use of the available instrumentation.

We thank A.N. Oraevskiĭ for useful discussions. This work was supported by INTAS (grant no. 01-0855) and the Russian Foundation for Basic Research (project no. 02-02-17686).

REFERENCES

1. K. E. Strecker, G. B. Partridge, A. G. Truscott, and R. G. Hulet, Nature **417**, 150 (2002).
2. T. Bourdel, L. Khaykovich, F. Schreck, *et al.*, in *Technical Digest of International Quantum Electronics Conference, IQEC'2002, Moscow, 2002*, p. 54.
3. A. E. Muryshev, H. B. van Linden, van den Heuvell, and G. V. Shlyapnicov, Phys. Rev. A **60**, R2665 (1999).
4. Y. S. Kivshar, T. J. Alexander, and S. K. Turitsyn, Phys. Lett. A **278**, 225 (2001).
5. N. N. Rosanov, A. G. Vladimirov, D. V. Skryabin, and W. J. Firth, Phys. Lett. A **293**, 45 (2002).
6. V. V. Grigor'yants, M. E. Zhabotinskiĭ, and V. F. Zolin, *Quantum Frequency Standards* (Nauka, Moscow, 1968), p. 94.
7. J. A. Sauer, M. D. Barrett, and M. S. Chapman, Phys. Rev. Lett. **87**, 270401 (2001).
8. L. D. Landau and E. M. Lifshitz, *Course of Theoretical Physics*, Vol. 8: *Electrodynamics of Continua* (Fizmatlit, Moscow, 2001; Pergamon, New York, 1984).
9. E. R. I. Abraham, W. I. McAlexander, C. A. Sackett, and R. G. Hulet, Phys. Rev. Lett. **74**, 1315 (1995).
10. A. J. Moerdijk and B. J. Verhaar, Phys. Rev. A **53**, R19 (1996).
11. W. Ketterle, Phys. Today **52** (12), 30 (1999).
12. F. T. Smith, J. Chem. Phys. **36**, 248 (1962).

Translated by V. Sipachev

JETP Letters, Vol. 76, No. 6, 2002, pp. 374–376. From Pis'ma v Zhurnal Éksperimental'noĭ i Teoreticheskoĭ Fiziki, Vol. 76, No. 6, 2002, pp. 434–436.

Quadrupolar Glass State in Para-Hydrogen and Ortho-Deuterium under Pressure¶

T. I. Schelkacheva

Institute for High Pressure Physics, Russian Academy of Sciences, Troitsk, Moscow region, 142092 Russia
e-mail: schelk@hppi.troitsk.ru

Received August 8, 2002

The main features of the possible quadrupolar glass state in ortho-deuterium and para-hydrogen under high pressure are predicted and considered in replica-symmetric approximation in analogy with glassy behavior of diluted ortho-hydrogen at low pressures. The quadrupolar model with $J = 2$ is suggested. The orientational order and glass regime grow continuously on cooling, as is the case with ortho-para hydrogen mixtures at zero pressure. © *2002 MAIK "Nauka/Interperiodica".*

PACS numbers: 64.70.Kb; 62.50.+p; 61.43.Fs

The structure of high-pressure phases of solid hydrogen has been widely investigated recently (e.g. [1, 2]). At low pressures, the centers of para-hydrogen and ortho-deuterium molecules occupy lattice sites of the hcp structure. The molecules are in spherically symmetric phase (I or SP). Between 28 GPa for *o*-D_2 and 110 GPa for *p*-H_2 and ~150 GPa, the molecules become orientationally ordered in broken-symmetry phase II (BS).

High pressure breaks the rotational symmetry of the $J = 0$ solids. The ordering occurs even in the systems of para-hydrogen and ortho-deuterium molecules because of the mixing of higher order J levels with the ground state $J = 0$ as a result of the increase of the intermolecular interactions at high pressures [1, 2]. The anisotropic interaction between two molecules is dominated at low pressures [3] by electrostatic quadrupole–quadrupole (EQQ) interaction, which plays a major role below 100 GPa [1, 4]. However, it is necessary to take into account other anisotropic interactions to understand the results of precise experiments (e.g., Raman scattering [1]).

The purpose of this article is to show the possibility of an orientational glass state in solid *p*-H_2 and *o*-D_2 under pressure. Only the main features of this phenomenon will be taken into account. The $J = 0 \longrightarrow J = 2$ transitions take place as a result of pressure increase. In this case, the $J = 2$ molecules may be randomly distributed on a close-packed lattice. It was indicated in [2, 5] that rotational disorder under pressure may be frozen. The molecules with $J = 0$ are spherically symmetric, have no electric quadrupole moment, and play the role of dilutant.

So we can consider the quadrupolar glass state in analogy with glassy behavior of diluted *o*-H_2 and *p*-D_2 at low temperatures and pressures. In this case, only the molecular species are orientable. They have orbital angular momentum $J = 1$. The ordered state is characterized by a long-range orientational order at high ortho-H_2 and para-D_2 concentrations [3]. However, for concentrations less than approximately 55%, measurements show no evidence of orientational phase transition. Instead, NMR experiments have been interpreted in terms of freezing of the orientational degrees of freedom [3, 6]. This state is so-called quadrupolar glass.

The EQQ interaction can bring about the orientational glass state at high pressure in *p*-H_2 and *o*-D_2. The rough estimation of the $0 \longrightarrow 2$ transition probability α can be done [4, 5] using quantum mechanical perturbation theory, because the main anisotropic part (EQQ) of the intermolecular interaction is small [3]. We have $\alpha = 4 \times 10^{-4}$ for D_2 and $\alpha = 6 \times 10^{-5}$ for H_2 at zero pressure. The probability to find a $J = 2$ molecule increases strongly with pressure; $\alpha = 0.1$ at 40 GPa for D_2 and 150 GPa for H_2 and $\alpha = 0.4$ for D_2 at 150 GPa. It is possible that an intermediate range of α exists where a quadrupolar glass occurs.

Let us consider the system of particles on lattice sites i, j with the truncated EQQ Hamiltonian

$$H = -\frac{1}{2}\sum_{i \neq j} J_{ij} Q_i Q_j, \qquad (1)$$

where the quadrupole component $Q = \frac{1}{2}[3(z/r)^2 - 1]$ can be replaced by an equivalent operator with the same matrix elements $\hat{Q} \sim [3J_z^2 - J(J+1)]$ in the space $J = \text{const}$, $\text{Tr}\,\hat{Q} = 0$.

Quadrupolar glass freezing in mixtures of ortho- and para-hydrogen was considered in [7] with

$$Q = 3J_z^2 - 2, \qquad (2)$$

¶This article was submitted by the author in English.

0021-3640/02/7606-0374$22.00 © 2002 MAIK "Nauka/Interperiodica"

where $J_z = 1, 0, -1$ and $J = 1$.

This model describes well the zero-pressure experiments on ortho–para mixtures even in a replica-symmetric approach.

Now, the Hamiltonian (1) will be examined on the condition $J = 2$ and $J_z = 0, 1, -1, 2, -2$:

$$Q = \frac{1}{3}[3J_z^2 - 6], \tag{3}$$

where J_{ij} are random exchange interactions with Gaussian probability distribution

$$P(J_{ij}) = \frac{1}{\sqrt{2\pi}J}\exp\left[-\frac{(J_{ij} - J_0)^2}{2J^2}\right].$$

The scaling $J = \tilde{J}/\sqrt{N}$, $J_0 = \tilde{J}_0/N$ ensures, as usual, a sensible thermodynamic limit. The multiplier 1/3 in Eq. (3) is used for simplicity.

Using the replica method, the free energy is obtained in the form

$$\langle F\rangle_J/NkT = -\lim_{n\to 0}\frac{1}{n}\max\left\{-\sum_\alpha\frac{(x^\alpha)^2}{2} - \sum_\alpha\frac{(w^\alpha)^2}{2} - \sum_{\alpha>\beta}\frac{(y^{\alpha,\beta})^2}{2} + \ln \mathrm{Tr}_{\{Q^\alpha\}}\exp\left[\sum_\alpha x^\alpha\sqrt{\frac{\tilde{J}_0}{kT}}Q^\alpha + \sum_\alpha w^\alpha\frac{1}{\sqrt{2}}t(Q^\alpha)^2 + \sum_{\alpha>\beta}y^{\alpha,\beta}tQ^\alpha Q^\beta\right]\right\},$$

where $t = \tilde{J}/kT$.

Extreme conditions for the free energy give the equations for order parameters

$$\begin{aligned} m^\alpha &= (x^\alpha)^{\mathrm{extr}}/\sqrt{\frac{\tilde{J}_0}{kT}} = \langle Q^\alpha\rangle_{\mathrm{eff}},\\ q^{\alpha,\beta} &= (y^{\alpha,\beta})^{\mathrm{extr}}/t = \langle Q^\alpha Q^\beta\rangle_{\mathrm{eff}},\\ p^\alpha &= (w^\alpha)^{\mathrm{extr}}\sqrt{2}/t = \langle (Q^\alpha)^2\rangle_{\mathrm{eff}}, \end{aligned} \tag{4}$$

where averaging is performed with the effective Hamiltonian

$$-H_{\mathrm{eff}} = \sum_\alpha\frac{\tilde{J}_0}{kT}m^\alpha Q^\alpha + \sum_\alpha\frac{t^2}{2}p^\alpha(Q^\alpha)^2 + \sum_{\alpha>\beta}t^2q^{\alpha,\beta}Q^\alpha Q^\beta.$$

Free energy and order parameters in the replica-symmetric [8] case become

$$F = -NkT\left\{-\left(\frac{\tilde{J}_0}{kT}\right)\frac{m^2}{2} + t^2\frac{q^2}{4} - t^2\frac{p^2}{4} + \int_{-\infty}^{\infty}\frac{dz}{\sqrt{2\pi}}\exp\left(-\frac{z^2}{2}\right)\ln \mathrm{Tr}[\exp(\theta_2 Q + \theta_1 Q^2)]\right\}. \tag{5}$$

Here,

$$\theta_1 = t^2\frac{p-q}{2} \text{ and } \theta_2 = zt\sqrt{q} + m\left(\frac{\tilde{J}_0}{kT}\right).$$

Order parameters are m quadrupolar order parameter (analog of magnetic moment in spin glasses), q glass order parameter, and p auxiliary order parameter:

$$m = \int_{-\infty}^{\infty}\frac{dz}{\sqrt{2\pi}}\exp\left(-\frac{z^2}{2}\right)\frac{\mathrm{Tr}[Q\exp(\theta_2 Q + \theta_1 Q^2)]}{\mathrm{Tr}[\exp(\theta_2 Q + \theta_1 Q^2)]} = \int_{-\infty}^{\infty}\frac{dz}{\sqrt{2\pi}}\exp\left(-\frac{z^2}{2}\right)2\left\{\frac{\exp(4\theta_1)[-\exp(-2\theta_2) + \exp(2\theta_2)] - \exp(-\theta_2\theta_1)}{\exp(4\theta_1)[\exp(-2\theta_2) + 2\exp(2\theta_2)] + 2\exp(-\theta_2\theta_1)}\right\}, \tag{6}$$

$$q = \int_{-\infty}^{\infty}\frac{dz}{\sqrt{2\pi}}e^{-z^2/2}\left\{\frac{\mathrm{Tr}[Q\exp(\theta_2 Q + \theta_1 Q^2)]}{\mathrm{Tr}[\exp(\theta_2 Q + \theta_1 Q^2)]}\right\}^2 = \int_{-\infty}^{\infty}\frac{dz}{\sqrt{2\pi}}\exp\left(-\frac{z^2}{2}\right)4\left\{\frac{\exp(4\theta_1)[-\exp(-2\theta_2) + \exp(2\theta_2)] - \exp(-\theta_2\theta_1)}{\exp(4\theta_1)[\exp(-2\theta_2) + 2\exp(2\theta_2)] + 2\exp(-\theta_2\theta_1)}\right\}^2, \tag{7}$$

$$p = \int_{-\infty}^{\infty}\frac{dz}{\sqrt{2\pi}}e^{-z^2/2}\frac{\mathrm{Tr}[Q^2\exp(\theta_2 Q + \theta_1 Q^2)]}{\mathrm{Tr}[\exp(\theta_2 Q + \theta_1 Q^2)]} = \int_{-\infty}^{\infty}\frac{dz}{\sqrt{2\pi}}\exp\left(-\frac{z^2}{2}\right)2\left\{\frac{2\exp(4\theta_1)[-\exp(-2\theta_2) + 2\exp(2\theta_2)] - \exp(-\theta_2\theta_1)}{\exp(4\theta_1)[\exp(-2\theta_2) + 2\exp(2\theta_2)] + 2\exp(-\theta_2\theta_1)}\right\}. \tag{8}$$

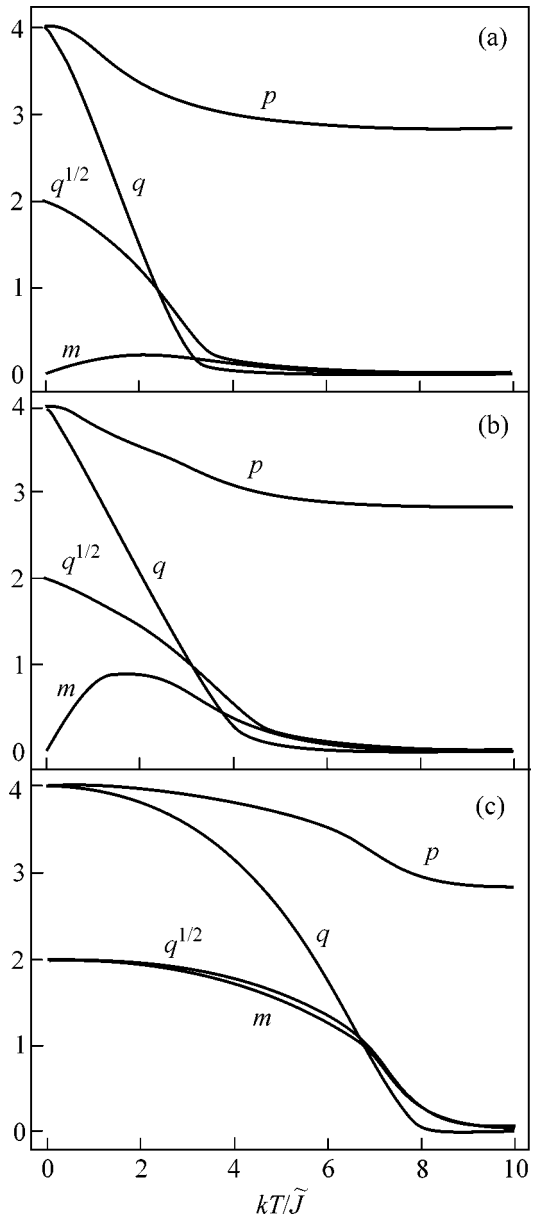

Fig. 1. Order parameters for the case (a) $\tilde{J}_0/\tilde{J} = 0$, (b) $\tilde{J}_0/\tilde{J} = 1$, and (c) $\tilde{J}_0/\tilde{J} = 2.5$.

The temperature dependence of the order parameters obtained from Eqs. (6)–(8) is represented in Fig. 1. There is no trivial solution $m = 0$, $q = 0$ at a finite temperature, because $\mathrm{Tr}Q^3 \neq 0$. The orientational order and glass regime grow continuously on cooling, just as in the case of Hamiltonian (1)–(2) describing the ortho–para hydrogen mixtures at zero pressure [7]. The quadrupolar long-range order is present for $T > 0$ even if $\tilde{J}_0 = 0$. In the pure case ($\tilde{J} = 0$, $\tilde{J}_0 \neq 0$), we have from Eqs. (6)–(7) $q^{1/2} = m$.

It is easy to see from Eq. (2) that $Q^2 = 2 - Q$. So the equation for p is not independent, and $p = 2 - m$. There is no similar expression for Q^2 from Eq. (3) and for order parameter p.

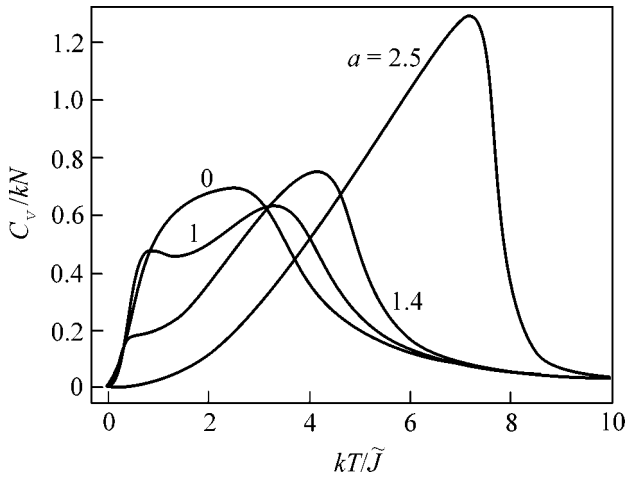

Fig. 2. Specific heat as a function of $(kT/\tilde{J})$ for $a = \tilde{J}_0/\tilde{J} = \{0; 1; 1.4; 2.5\}$.

Using Eq. (5) for free energy, the heat capacity can be written in the form

$$\frac{C_v}{kN} = \frac{d}{d(kN/\tilde{J})}\left\{\left(\frac{\tilde{J}}{kT}\right)\frac{q^2 - p^2}{2}\right\} - \left(\frac{\tilde{J}_0}{\tilde{J}}\right)m\frac{dm}{d(kT/\tilde{J})}. \quad (9)$$

Specific heat as a function of (kT/J) calculated from Eq. (9) for four cases of $(\tilde{J}_0/\tilde{J})$ is shown in Fig. 2. The temperature dependence of C_v is smooth, as in ortho–para mixtures at zero pressure.

In conclusion, the main features of the random quadrupolar system (1), (3) are considered in the replica-symmetric mean-field approximation. This system with $J = 2$ was not considered earlier. The possible realization of the quadrupolar glass state under high pressure in ortho-deuterium and para-hydrogen is predicted.

I am grateful to E.E. Tareyeva and V.N. Ryzhov for useful and stimulating discussions. This work was supported by the Russian Foundation for Basic Research, project no. 02-02-16622a.

REFERENCES

1. A. F. Goncharov, M. A. Strzhemechny, H. K. Mao, and R. J. Hemly, Phys. Rev. B **63**, 064304 (2001).
2. H. K. Mao and R. J. Hemley, Rev. Mod. Phys. **66**, 671 (1994).
3. I. F. Silvera, Rev. Mod. Phys. **52**, 393 (1980).
4. T. I. Schelkacheva, Phys. Lett. A **239**, 397 (1998).
5. E. A. Lutchinskaia and E. E. Tareyeva, in *The High Pressure Effects in Materials: Collection of Scientific Works* (Naukova Dumka, Kiev, 1986), p. 21.
6. N. S. Sullivan, M. Devoret, B. P. Cowan, and C. Urbina, Phys. Rev. B **17**, 5016 (1978).
7. E. A. Lutchinskaia, V. N. Ryzhov, and E. E. Tareyeva, J. Phys. C **17**, L665 (1984).
8. S. Kirkpatrick and D. Sherrington, Phys. Rev. B **17**, 4384 (1978).

JETP Letters, Vol. 76, No. 6, 2002, pp. 377–379. Translated from Pis'ma v Zhurnal Éksperimental'noĭ i Teoreticheskoĭ Fiziki, Vol. 76, No. 6, 2002, pp. 437–439.

On Effective Electron Mass of Silicon Field Structures at Low Electron Densities

V. T. Dolgopolov

Institute of Solid-State Physics, Russian Academy of Sciences, Chernogolovka, Moscow region, 142432 Russia

Received August 22, 2002

The trial wave function method developed in [10, 11] for the case of a narrow *s* band in a perfect crystal is adapted for the calculation of the concentration dependence of the effective mass and the Landé factor in a two-dimensional electron system of low density. It has been found that the effective mass has a tendency to divergence at a certain critical concentration, whereas the *g* factor remains finite. © *2002 MAIK "Nauka/Interperiodica"*.

PACS numbers: 73.20.-r; 71.30.+h; 71.10.Ca

As the temperature decreases, a dilute electron gas in highly mobile silicon field structures exhibits a strong drop in the resistance if the electron concentration n_s is higher than a certain critical one $n_s > n_c$ and an increase in the resistance when $n_s < n_c$ [1]. In the vicinity of n_c, the resistance possesses scaling properties as a function of temperature and electron density. This instance from the very first caused researchers to consider the observed transition as a disorder-controlled quantum phase metal–insulator transition (MIT) and gave rise to a tide of similar investigations of other objects in which any change in the sign of the derivative $(dR/dT)(n_s)$ was taken as an evidence of the occurrence of a quantum phase MIT.

In the recent experimental study [2] of the variation of the screening properties of a two-dimensional electron system, temperature [3] was interpreted in terms of the work [4], and a strong increase in the effective mass was observed in silicon metal–oxide–semiconductor (MOS) structures as the electron density approached a value of $\sim 0.8 \times 10^{11}$ cm^{-2}, which virtually coincided with n_c in the best of the investigated samples. A similar behavior of the cyclotron mass was observed in independent experiments [5] on the measurement of the temperature dependence of Shubnikov–de Haas oscillations. An analysis of the experimental data similar to that made in [2] but performed in the opposite limit in the ratio of valley-splitting energy to temperature with the use of data of other experimental groups and samples from other sources [6, 7] confirmed the versatility of the $m^*(n_s)$ curve.

The conclusion that should be made from the recent experimental data is that the quantum phase transition observed in the most perfect MOS structures is rather the property of a pure disorder-free two-dimensional electron system. A qualitative theory of two-dimensional electron Fermi liquid in a state close to crystallization was presented in [8, 9]. Below, I propose a quantitative description of a two-dimensional paramagnetic electron liquid in a precrystalline regime, adapting the trial wave function approach developed in [10, 11] for the case of a narrow *s* band in a perfect crystal.

I will assume that the ground state of an electron system with strong interaction in a regime close to crystallization can be described as an electron crystal with a great number of charge-carrying mobile defects. The real two-dimensional electron system will be replaced by a grid of lattice sites with a density of n_s. An electronic wave function of the Wannier type $\phi[(\mathbf{r}-\mathbf{g})n_s^{1/2}]$, where the vector $\mathbf{g}$ specifies the position of a lattice site, will be associated with each site. The corresponding creation operator is $a_\mathbf{g}^\dagger$. If each site were occupied by only one electron, the system would represent a perfect electron crystal. In fact, there is a certain probability depending on n_s that in the ground state, a site can be occupied by two electrons with opposite spins. The number of such sites eventually determines the number of mobile excitations and, hence, the transport properties of the system.

I will construct Bloch wave functions based on lattice sites

$$\psi_\mathbf{k}(\mathbf{r}) = n_s^{-1/2}\sum_\mathbf{g} \exp(i\mathbf{kg})\phi(\mathbf{r}-\mathbf{g}), \quad (1)$$

$$a_\mathbf{k}^\dagger = n_s^{-1/2}\sum_\mathbf{g} \exp(i\mathbf{kg})a_\mathbf{g}^\dagger. \quad (2)$$

The Hamiltonian of the system contains the electron kinetic energy and the electron interaction at one site

$$H = \sum_\mathbf{k} \varepsilon_\mathbf{k}(a_{\mathbf{k}\uparrow}^\dagger a_{\mathbf{k}\uparrow} + a_{\mathbf{k}\downarrow}^\dagger a_{\mathbf{k}\downarrow}) + \frac{\alpha e^2}{\varepsilon_0 n_s^{1/2}}\sum_\mathbf{g} a_{\mathbf{g}\uparrow}^\dagger a_{\mathbf{g}\downarrow}^\dagger a_{\mathbf{g}\downarrow} a_{\mathbf{g}\uparrow}. \quad (3)$$

0021-3640/02/7606-0377$22.00

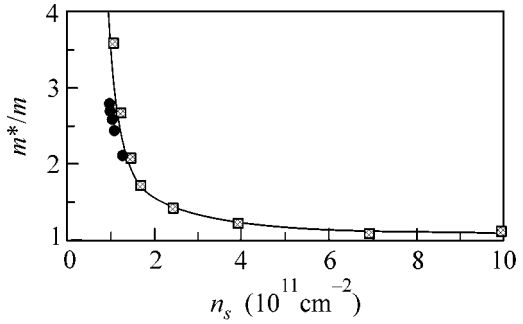

Fig. 1. Effective mass as a function of electron concentration. The solid line corresponds to Eq. (9) with $n_{c2} = 0.78 \times 10^{11}$ cm^{-2}. Squares and circles correspond to the experimental data from [2] and [13], respectively.

Here, $\varepsilon_{\mathbf{k}} = \hbar^2 k^2/2m$, and ε_0 is the static permittivity. We introduced a coefficient α into the interaction energy determined by the exact form of the wave function on the site and completely neglected the electron interaction on the neighboring sites. Proceeding to the limit of the gas on noninteracting electrons requires that the modulation in Eq. (1) disappear and the coefficient α be a slowly varying function of n_s vanishing at $n_s^{-1} \longrightarrow 0$. We will neglect this weak dependence in the region of low electron densities.

In [10], it was proposed that a many-body trial function be used for the ground state in the form

$$\psi = \sum_{G\Gamma} A_{G\Gamma} \prod_{G} a^{\dagger}_{\mathbf{g}\uparrow} \prod_{\Gamma} a^{\dagger}_{\mathbf{g}\downarrow} \Phi_0, \qquad (4)$$

where G and Γ are the sets of sites occupied by electrons with spins up and down, respectively; and Φ_0 is a vacuum state. It is convenient to express the function ψ through operators of creation and annihilation of Bloch waves and to take into account electron correlation by decreasing the coefficient $A_{G\Gamma}$ in Eq. (4) by a factor of η^{ν} if the corresponding product implies the occurrence of doubly occupied sites whose fraction equals ν ($0 < \eta < 0$). The relation between ν and η in the ground state was obtained in [10]. For our case,

$$\eta = \nu\left(\frac{1}{2} - \nu\right)^{-1}. \qquad (5)$$

The probability that a one-particle state with a wave vector $\mathbf{k}$ is occupied undergoes a jump at $k = k_F$ by the value

$$q = 16\nu\left(\frac{1}{2} - \nu\right). \qquad (6)$$

Thus, the trial wave function describes a mixture of functions that corresponds to a fully occupied band (solid spin-ordered phase) and a paramagnetic electron liquid. The transition to the solid phase is continuous and is characterized by the parameter q ($0 \le q \le 1$): $q = 1$ in the paramagnetic electron liquid with weak interaction, and $q = 0$ in the electron crystal.

The mean value of the Hamiltonian given by Eq. (3) in the state with given ν equals

$$\langle H\rangle_{\nu} = \frac{1}{2} n_s q \varepsilon_F + \nu \frac{\alpha e^2}{\varepsilon_0} n^{3/2}, \qquad (7)$$

where ε_F is the Fermi energy of an equivalent number of electrons in the absence of interaction. According to [11], the expression in Eq. (7) is minimized with respect to ν with regard to Eq. (6). A minimum of the Hamiltonian is attained at

$$\nu = \frac{1}{4}\left(1 - \left(\frac{n_{c1}}{n_s}\right)^{1/2}\right); \quad n_{c1} = \left(\frac{\alpha e^2 m}{2\varepsilon_0 \pi \hbar^2}\right)^2, \qquad (8)$$

which, according to Eq. (6), corresponds to

$$q^{-1} = \frac{m^*}{m} = \frac{n_s}{n_s - n_{c1}}. \qquad (9)$$

Here, m^* is the renormalized effective mass. In the same way, following [11], the Landé factor can be found as

$$\frac{g^*}{g} = \left[1 - \left(\frac{n_{c1}}{n_s}\right)^{1/2} \frac{1 + \frac{1}{2}(n_{c1}/n_s)^{1/2}}{(1 + (n_{c1}/n_s)^{1/2})^2}\right]^{-1}. \qquad (10)$$

The simplest of way of generalization to the case of two valleys is in considering two parallel sublattices where in each of them the number of electrons equals $n_s/2$ and the characteristic cell size is diminished compared to the one-valley case by a factor of β. The coefficient β is determined by the ratio of Coulomb energies of inter- and intravalley interactions. In the limit of two sublattices in one plane, $\beta = \sqrt{2}$. In the case of two valleys, n_{c1} in Eqs. (9) and (10) should be changed for $n_{c2} = 2\beta^2 n_{c1}$.

A comparison of the curves obtained in this way with experimental results is shown in Figs. 1 and 2. One fitting parameter $n_{c2} = 0.78 \times 10^{11}$ cm^{-2} has been used, which corresponds to $\alpha = 0.15$. It is evident from the figures that the behavior of both the effective mass and the g factor is reasonably described within the framework of the proposed model, though the coefficient α is approximately twice as large as the value expected according to numerical calculations [12].

It should be specially noted that the above considerations give no way of judging the spin state of the solid phase, because it is determined by the exchange interaction of electrons on neighboring sites. Moreover, in the immediate vicinity of the transition point, in the region where $(\langle H(n_s)\rangle_{\nu} - \langle H(n_{c2})\rangle_{\nu}) n_s^{-1}$ turns out to be smaller than the exchange energy of electrons on neigh-

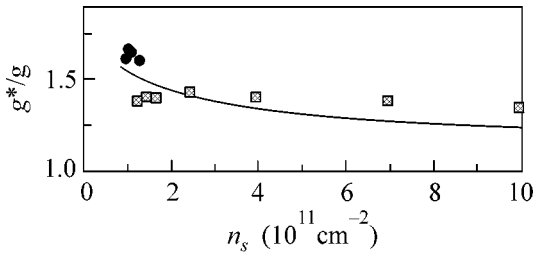

Fig. 2. Effective g factor as a function of electron density. The designations of experimental points are the same as in Fig. 1.

boring sites, the proposed description does not work in the paramagnetic electron liquid as well. Thus, the issues of the phase diagram in the immediate vicinity of the transition point and those of the spin structure of the solid phase remain out of the scope of this consideration. In general, the approximation used is poorly controlled, and the rather good description of experiment still remains its only justification.

It is well known that the concentration n_c that corresponds to a change of the sign of the derivative dR/dT strongly varies from sample to sample, depending on the disorder in the electron system under study. An impression is gained from experimental data that the transition point n_{c2} measured for different samples also somewhat varies. This fact can also be related to the effect of disorder, as was discussed in [8, 9]. In strongly disordered electron systems, $n_c \gg n_{c2}$ and the effect considered above, namely, the dramatic increase in the effective mass is not observed. In the most perfect of the electron systems studied, $n_c \simeq n_{c2}$.

The author is grateful to V.F. Gantmakher, A. Gol'd, S.V. Iordanskiĭ, B. Spivak, D.E. Khmel'nitskiĭ, and A.A. Shashkin for useful discussions. A significant part of this work was carried out at the University of Munich, and the author is grateful to J.P. Kotthaus and researchers from his institute for help and discussions.

This work was supported by the Russian Foundation for Basic Research, the Ministry for Science and Technology of the Russian Federation, and Alexander Von Humboldt Fellowship.

REFERENCES

1. E. Abrahams, S. V. Kravchenko, and M. P. Sarachik, Rev. Mod. Phys. **73**, 251 (2001).
2. A. A. Shashkin, S. V. Kravchenko, V. T. Dolgopolov, and T. M. Klapwijk, Phys. Rev. B **66**, 073303 (2002).
3. A. Gold and V. T. Dolgopolov, Phys. Rev. B **33**, 1076 (1986).
4. Gabor Zala, B. N. Narozhny, and I. L. Aleiner, Phys. Rev. B **64**, 214204 (2001).
5. V. M. Pudalov, M. E. Gershenson, H. Kojima, *et al.*, Phys. Rev. Lett. **88**, 196404 (2002).
6. S. A. Vitkalov, K. James, B. N. Narozhny, *et al.*, cond-mat/0204566.
7. V. M. Pudalov, M. E. Gershenson, H. Kojima, *et al.*, cond-mat/0205449.
8. B. Spivak, Phys. Rev. B **64**, 085317 (2001).
9. B. Spivak, cond-mat/0205127.
10. M. C. Gutzwiller, Phys. Rev. **137**, A1726 (1965).
11. W. E. Brinkman and T. M. Rice, Phys. Rev. B **2**, 4302 (1970).
12. B. Tanatar and D. M. Ceperley, Phys. Rev. B **39**, 5005 (1989).
13. V. M. Pudalov, M. E. Gershenson, and H. Kojima, cond-mat/0110160.

Translated by A. Bagatur'yants

JETP Letters, Vol. 76, No. 6, 2002, pp. 380–393. Translated from Pis'ma v Zhurnal Éksperimental'noĭ i Teoreticheskoĭ Fiziki, Vol. 76, No. 6, 2002, pp. 440–454.

SUMMARY OF THE STUDIES SUPPORTED BY THE RUSSIAN FOUNDATION FOR BASIC RESEARCH PROJECT NO. 99-02-16238

Generation of Strong Langmuir Fields during Optical Breakdown of a Dense Gas

N. V. Vvedenskii and V. B. Gildenburg

Institute of Applied Physics, Russian Academy of Sciences, ul. Ul'yanova 46, Nizhni Novgorod, 603950 Russia
e-mail: gil@appl.sci-nnov.ru

Received August 1, 2002

Results are presented from theoretical studies and computer simulations of the resonant excitation of Langmuir waves during the ionization of a homogeneous gas by high-intensity laser radiation. Two mechanisms for the formation of nonuniform resonant structures in the discharge are examined: plasma-resonance ionization instability, resulting in the density modulation along the electric field vector, and gas breakdown in the field of a transversely inhomogeneous laser beam (a Bessel beam produced by an axicon lens). In both cases, the transition of the plasma density through the critical value is accompanied by the generation of intense Langmuir waves, the formation of fast ionization fronts, and the appearance of long-lived quasi-turbulent states. © *2002 MAIK "Nauka/Interperiodica".*

PACS numbers: 52.50.Jm; 52.35.–g

1. INTRODUCTION

The dynamics and structure of discharges created by electromagnetic waves in various frequency ranges (from RF to optical) have been actively investigated for more than three decades. Interest in these studies stems from both their fundamental theoretical importance and a number of various practical applications (the increase in the energy capacity of the working media of gas lasers and plasmochemical reactors, the development of new technologies for material processing, the propagation of high-power radiation through ionizable media, the creation of artificial radio-reflecting and ozone-restoring ionized regions in the Earth's atmosphere, etc.). In recent years, due to rapid progress in microwave electronics and laser technology, which resulted in the development of the methods for generating ultraintense microwave and optical pulses, great interest has been attracted to a number of new, previously uninvestigated aspects of the physics of the ionization interaction of radiation with matter and new prospects have been opened for various important applications of microwave and laser plasmas. Among these applications are, in the microwave range, the creation of high-speed plasma switches and the accumulators and transformers of the radiation energy and, in the optical range, the development of X-ray and UV lasers and laser–plasma methods for accelerating charge particles, radiation self-channeling, frequency upshifting, and the achievement of high energy density in small spatial regions during laser breakdowns of dense gaseous and condensed media and small-size atomic clusters.

An important physical factor governing the self-consistent evolution of high-intensity electromagnetic radiation and the plasma produced by it is the ionization nonlinearity [1–16]. In strong fields, the ionization nonlinearity, which is essentially inertialess, manifests itself (in contrast to other nonlinearities) as early as in the initial stage of breakdown and, in many cases, determines the type of the field–plasma structure that is formed in the final stage. A remarkable and unique property of the ionization nonlinearity (that is atypical of other nonlinearities, such as ponderomotive, thermal, and relativistic nonlinearities) is that it provides the mutual concentration (joint localization) of the field and plasma. These effects lead to the formation of localized field–plasma structures with large peak amplitudes of the electric field (substantially larger than the amplitude of the incident wave). A large group of these effects is related to the phenomenon of plasma resonance, i.e., the sharp increase in the oscillation amplitudes of the plasma particles and the longitudinal (parallel to the plasma density gradient) electric field in the regions where the plasma density is close to the critical density.

Previous theoretical and experimental investigations showed that the phenomenon of plasma resonance can play an important role in the dynamics of both microwave and optical discharges, resulting, in particular, in the development of small-scale ionization–field insta-

0021-3640/02/7606-0380$22.00

bility [3, 4, 6, 12, 17, 18] and in the formation of various types of self-sharpening structures in the nonlinear stage of this instability [12, 17, 19–21]. However, a number of important questions concerning the spatiotemporal discharge evolution under plasma resonance conditions still remain unanswered. First of all, this concerns one-, two-, and three-dimensional small-size active zones that appear due to the onset of the ionization–field instability or to ionization self-channeling in a quasi-uniform discharge; this also concerns discharges that are initially localized in small spatial regions (such as strata that are formed during breakdown of thin films [22], filamentary discharge in a dense gas or condensed medium on the axis of an axicon lens [23], and breakdown of atomic clusters [24]).

In the dynamics of this type of field–plasma structures, an important role is played by the processes of the resonant (transition) excitation and subsequent evolution of intense plasma (Langmuir) oscillations. Recent investigations showed that these processes (which were in fact ignored in the first studies on the theory of microwave and optical discharges) can strongly affect the spatial structure of the field and plasma, the generation of fast particles, and the frequency spectra of the reflected and scattered radiation. Although the problems of the resonant field–plasma interaction (in particular, the problem of the generation of Langmuir oscillations at the pumping frequency in the plasma corona of laser microexplosion) were discussed in many papers, all the publications on this subject were in fact devoted to the excitation of Langmuir oscillations in a beforehand prepared plasma. This also concerns the current investigations on the laser generation of Langmuir waves for the purpose of creating charged-particle accelerators (obviously, these studies are dealing with a nonresonant excitation of Langmuir oscillations at a frequency much lower than the pumping frequency). However, under the conditions that are of interest to us, the processes of Langmuir wave generation cannot be separated from the processes of plasma production. The theoretical description of these processes requires the development of new approaches based on the solution of self-consistent equations for the field and ionization kinetics.

To a great extent, the character of the resonant phenomena under study is determined by the shape and dimensions of the regions in which the plasma density in a certain stage of breakdown passes through the critical value. In this review, we present the results from theoretical studies of various dynamical models of optical discharge, which demonstrate the role of the main factors governing the formation and structure of these regions. Here, we do not consider breakdowns in small-size objects in which the structure of both the resonance region and the excited Langmuir oscillations are determined by the geometry of the ionized object itself. The dynamics of Langmuir oscillations in such objects possesses a number of interesting features that were demonstrated in [25, 26] by using a simple model of the ionization of a thin gas slab. However, theoretical investigations in this field have only gotten under way; therefore, in this review (which also includes a number of new, previously unpublished results), the main attention is given to other models that are examined in more detail and in which localized plasma resonance regions appear during breakdown of an unbounded uniform medium. As factors governing the appearance of these regions, in Section 2, we consider small-scale ionization instability, which results in the formation of a state with a developed Langmuir turbulence in the nonlinear stage, and, in Section 3, the strong spatial inhomogeneity of the incident ionizing radiation (breakdown in the axial region of a Bessel wave beam produced by an axicon lens).

In the subsequent theoretical analysis, numerical estimates, and computer simulations, we are oriented to the following ranges of the optical discharge parameters: the radiation wavelength in a vacuum is $\lambda_0 \sim 1$–$10\ \mu$m, the radiation intensity is $S \sim 10^{14}$–10^{15} W/cm^2, the pulse duration is $\tau \sim 50$–500 fs, and the gas pressure required to produce a plasma with the density on the order of the critical one (under the assumption of complete single ionization) is $p \sim 0.5$–50 atm. The electron–ion collisions frequency in the above radiation intensity range (i.e., at the corresponding oscillatory and thermal electron velocities) is two to three orders of magnitude lower than the field frequency, which allows one, as a rule, either to ignore collisions at all or to take them into account only when calculating the damping rate of the excited Langmuir oscillations in the late stage of the process.

2. PLASMA-RESONANCE INSTABILITY OF A HOMOGENEOUS DISCHARGE

Plasma-resonance ionization instability (PRII) belongs to a class of ionization–field instabilities that are caused by the mutual enhancement of the small initial perturbations of the field and plasma density [3, 12, 17]. In contrast to the other instabilities of this type that are associated with the ionization-induced scattering of a transverse wave [3, 13], this instability is related to small-scale density modulation along the electric field vector and can be regarded as an ionization analogue of the well-known modulational instability of a homogeneous ac field in a fully ionized plasma with a positive (focusing) nonlinearity [27]. The onset of PRII in an initially uniform discharge leads to its separation into thin dense layers (which are then disintegrate into two- or three-dimensional plasma objects), the formation of fast internal ionization fronts, and the generation of intense Langmuir oscillations [17, 20].

Various types of small-scale disintegration of a free localized discharge during the onset of PRII where observed in experiments on microwave gas discharges in focused wave beams [6, 18]. The results of these experiments are in good agreement with both the linear

theory of PRII [3, 6] and computer simulations of its nonlinear stage [17]. In optical discharges, direct observations of PRII are hampered due to its small spatial scale (the perturbation period is shorter than the field wavelength). To reveal the macroscopic effects of PRII (strong absorption, scattering, and a specific transformation of the radiation spectrum [12]) requires special experiments on optical breakdowns in dense gases (or condensed media) at relatively low electron-collision frequencies. At present, performing such experiments seems to be of great importance in view of the opportunity of achieving in them very high plasma densities (higher than the critical density) and high electromagnetic energy densities in the plasma resonance regions.

The first investigations of ionization instabilities in an ac field were performed within an elementary theory of the plasma polarization response. In this theory, both the time delay in the establishment of the steady-state forced electron oscillations with respect to plasma density variations and the spatial dispersion caused by electron thermal motion were ignored. This theory is applicable under the conditions $|\epsilon| \gg (kr_D)^2$ and $|\epsilon| \gg \omega\tau_E$, where

$$\epsilon = 1 - \frac{\omega_p^2}{\omega(\omega + i\nu)} = 1 - \frac{N}{N_c(1 + i\nu/\omega)} \qquad (1)$$

is the complex permittivity of a cold plasma, ω is the circular frequency of the field, $\omega_p = \sqrt{4\pi e^2 N/m}$ is the electron plasma (Langmuir) frequency, $r_D = \sqrt{T_e/4\pi e^2 N}$ is the electron Debye radius, k is the perturbation wavenumber, e and m are the charge and mass of an electron, ν is the electron collisions frequency, T_e is the electron temperature, N is the electron density averaged over the field period (this density is assumed to be equal to the ion density), $N_c = m\omega^2/4\pi e^2$ is the critical plasma density, and $\tau_E = |E(\partial E/\partial t)^{-1}|$ is the characteristics time scale of variations in the complex amplitude of the electric field E. The resonant excitation of plasma (Langmuir) oscillations can only be described by using an approach that goes beyond the scope of the above assumptions. An example of such an approach is described in [17]; below, we mainly follow this approach (which is somewhat refined and generalized).

2.1. Basic Equations and Assumptions. One-Dimensional Model

We represent the space- and time-dependent electric field vector $\tilde{\mathbf{E}}(\mathbf{r}, t)$ in the form $\tilde{\mathbf{E}}(\mathbf{r}, t) = (1/2)\mathbf{E}(\mathbf{r}, t)\exp(-i\omega t) + \text{c.c.}$, where the complex amplitude $\mathbf{E}(\mathbf{r}, t)$ (as well as the plasma density $N(\mathbf{r}, t)$) is assumed to be slowly varying (on the time scale $1/\omega$) functions of time. The time variations in the plasma density will be described by using the well-known expressions for the period-averaged gas ionization rate $\partial N/\partial t$. For a wide class of the ionization mechanisms, this rate can be represented as a function of the electric field amplitude $|\mathbf{E}|$ and the electron density N:

$$\partial N/\partial t = f(|\mathbf{E}|, N). \qquad (2)$$

First, we consider the spatiotemporal evolution of a discharge in a one-dimensional model ($\mathbf{E} = \mathbf{x}_0 E(x, t)$, $N = N(x, t)$), which describes the development of unstable perturbations on spatial scales that are smaller than the electromagnetic wavelength. The evolution of the slowly varying complex amplitude of the electric field can be determined from the following fairly simple (in fact, phenomenological) equation, which allows one to describe the generation and damping of Langmuir waves in a non-steady-state plasma (see also [27–29]):

$$\delta^2 \frac{\partial^2 E}{\partial x^2} + \frac{2i}{\omega}\frac{\partial E}{\partial t} + \hat{\Gamma}E + \epsilon E = D. \qquad (3)$$

Here, $\delta = \sqrt{3}\, V_T/\omega$, V_T is the electron thermal velocity, and $\hat{\Gamma}$ is the operator describing collisionless Landau damping. In gas breakdown, the electron thermal velocity V_T is determined, generally speaking, by the amplitude of the electron oscillatory velocity $V_\sim = e|E|/m\omega$. The relationship between these velocities depends on the ionization mechanism: for electron-impact ionization, the thermal velocity is, as a rule, substantially higher that the oscillatory velocity [2], and, for tunneling ionization in a field with an amplitude that is not too small as compared to the intra-atomic field E_a (see below), the velocity V_T is lower than or on the order of $V_\sim$ [30]. In the calculations presented below, we will assume for simplicity that the thermal velocity V_T is a given constant, which is determined in order of magnitude by a certain effective value of $V_\sim$. We also assume that $\nu = \text{const} \ll \omega$ and use the following model expression for $\hat{\Gamma}$:

$$\hat{\Gamma} = i\delta^4 \frac{\partial^4}{\partial x^4}. \qquad (4)$$

The quantity $D = D(t)$ on the right-hand side of Eq. (3) is the x component of the electric induction (electric displacement) vector $\mathbf{D}$. In the one-dimensional model under consideration (the so-called plane capacitor model), this quantity does not depend on x in view of the equation $\nabla \cdot \mathbf{D} = \partial D/\partial x = 0$. The evolution of small-scale one-dimensional (spatially periodic) structures can be determined by assuming that either the electric induction $D(t)$ or the x-averaged electric field $\bar{E}(t)$ is a given function of time. Actually, the functions $D(t)$ and $\bar{E}(t)$ are determined by the two- or three-dimensional evolution of the large-scale field–plasma structure and should be calculated by solving an equation for the averaged (over small-scale perturbations) electric field; an example of such a calculation is presented in Section 2.4.

2.2. Linear Stage of the Instability

Let us consider the stability of a quasi-steady discharge with respect to small spatially periodic field and density perturbations. We linearize Eqs. (2) and (3) against the homogeneous unperturbed state, $E_0(t)$ and $N_0(t)$, satisfying Eqs. (2) and (3) at $\partial/\partial x = 0$. Then, in the absence of dissipation, we obtain the following set of equations for small perturbations of the complex field amplitude $E_1(x, t) = E - E_0$ and the electron density $N_1 = N - N_0$:

$$\delta^2\frac{\partial^2 E_1}{\partial x^2} + \frac{2i}{\omega}\frac{\partial E_1}{\partial t} + \epsilon_0 E_1 - E_0\frac{N_1}{N_c} = 0, \quad (5)$$

$$\frac{\partial N_1}{\partial t} - \frac{1}{2}\alpha N_c(E_1 + \text{c.c.}) - \beta N_1 = 0, \quad (6)$$

where $\epsilon_0(t) = 1 - (N_0(t)/N_c)$ and the coefficients $\alpha = N_c^{-1}\partial f/\partial|E|$ and $\beta = \partial f/\partial N$ are determined by the values of the corresponding derivatives of the ionization rate in the unperturbed state. For perturbations of the form E_1, $N_1 \sim \exp(\int\gamma dt + ikx)$, under the assumption that the homogeneous state evolves on time scale much larger than the characteristics time γ^{-1} during which the instability under consideration develops, Eqs. (5) and (6) yield the following dispersion relation for the time constant γ:

$$4\gamma^3/\omega^3 + \gamma(\epsilon_0 - \delta^2k^2)^2 - \alpha E_0(\epsilon_0 - \delta^2k^2) = 0. \quad (7)$$

When deriving this equation, we neglected the terms containing the factor β, which is justified for all the ionization mechanisms of interest (impact, tunneling, and multiphoton ionization) under the adopted assumption that the homogeneous state is slow varying.

For a given real perturbation wavenumber k, dispersion relation (7) has one real root γ_1 and two complex conjugate roots $\gamma_{2,3}$ with $\text{Re}\gamma_{2,3} = -\gamma_1/2$:

$$\gamma_1 = \omega\frac{(\epsilon_0 - \delta^2k^2)^{1/3}}{2}(A_1 - A_2), \quad (8)$$

$$\gamma_{2,3} = -\frac{\gamma_1}{2} \pm i\omega\frac{(\epsilon_0 - \delta^2k^2)^{1/3}}{4}(A_1 + A_2)\sqrt{3}, \quad (9)$$

$$A_{1,2} = \left(\sqrt{\frac{(\epsilon_0 - \delta^2k^2)^4}{3^3} + \left(\frac{\alpha E_0}{\omega}\right)^2} \pm \frac{\alpha E_0}{\omega}\right)^{1/3}. \quad (10)$$

We can see that for any value of $\delta^2k^2 \neq \epsilon_0$, the dispersion relation has roots with the positive real part $\Gamma = \text{Re}\gamma > 0$, corresponding to unstable solutions. For $\delta^2k^2 = \epsilon_0$, all the roots are zero. For $\delta^2k^2 < \epsilon_0$, the instability is related to the root γ_1, and for $\delta^2k^2 > \epsilon_0$, it is related to the roots $\gamma_{2,3}$. The maximum instability growth rate Γ_m and the corresponding wavenumber k_m depend on the relation between the parameters ϵ_0 and $\epsilon_c = \sqrt{\alpha E_0/\omega}$; in particular, for $\epsilon_0 > \epsilon_c$, we have $\Gamma_m = \sqrt{\alpha E_0\omega}/2$ and $\delta^2k_m^2 = \epsilon_0 - \epsilon_c$. Figure 1 shows the growth rate $\Gamma = \text{Re}\gamma_2$ as a function of the wavenumber for $\epsilon_0 = 0$.

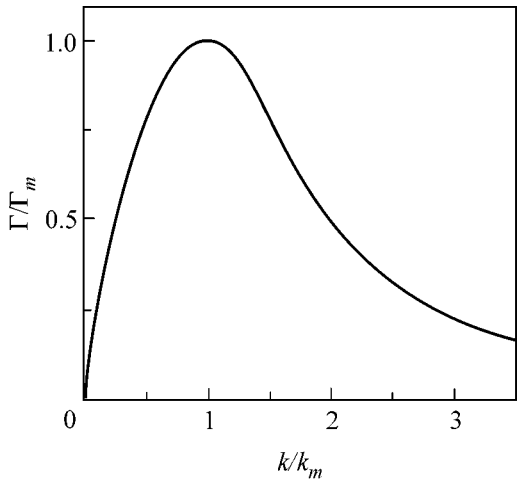

Fig. 1. Instability growth rate $\Gamma = \text{Re}\gamma_2$ vs. wavenumber k for $\omega = \omega_p$ ($k_m = \delta^{-1}(\alpha E_0/\omega)^{1/4}$ and $\Gamma_m = \sqrt{\alpha E_0\omega}/4$).

We note that the above results are applicable in the limited ranges of the time constant and wavenumber: $E_0^{-1}\partial E_0/\partial t \ll \gamma \ll \omega$ and $(\omega/c)\sqrt{\epsilon_0} \ll k \ll \omega_p/V_T$. At the upper boundary of the above wavenumber range, collisionless damping begins to play an important role. At the lower boundary, the perturbation wavelength becomes comparable to the wavelengths of the transverse wave; i.e., the applicability conditions for the used one-dimensional (capacitor) model fail to hold.

2.3. Nonlinear Stage of Instability

The dynamics of large-amplitude perturbations in the nonlinear stage of instability for various ionization mechanisms determining the form of the function $f(|\mathbf{E}|, N)$ in Eq. (2) was studied by using computer simulations. The scenarios of the solution behavior for different f have much in common. Here, we present, as an illustration, the results obtained with the use of the well-known model expression for the average rate of tunneling ionization of hydrogen atoms in a linearly polarized field [17, 31]:

$$f = 4\left(\frac{3}{\pi}\frac{E_a}{|\mathbf{E}|}\right)^{1/2}\Omega(N_g - N)\exp\left(-\frac{2}{3}\frac{E_a}{|\mathbf{E}|}\right). \quad (11)$$

Here, $\Omega = me^4/\hbar^3 = 4.16 \times 10^{16}$ s^{-1} and $E_a = m^2e^5/\hbar^4 = 5.14 \times 10^9$ V/cm are the atomic units of the frequency and electric field, respectively; $\hbar$ is Planck's constant; and N_g is the density of neutral gas atoms before ionization. Equations (2)–(4) and (11) were solved numeri-

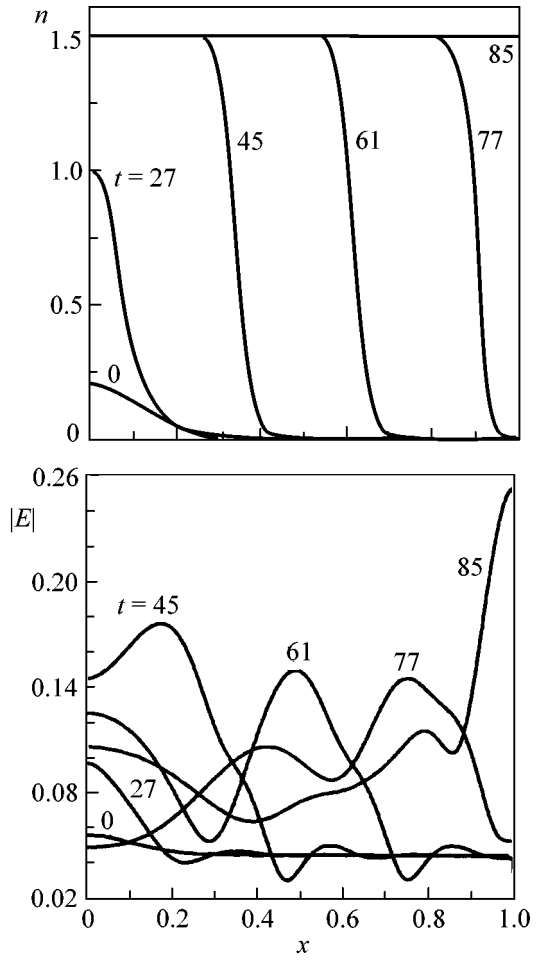

Fig. 2. Spatiotemporal evolution of the plasma density $n(x, t)$ and the field amplitude $|E(x, t)|$ in the nonlinear stage of instability for D = const. Numerals by the curves show the time values.

cally over the interval $0 \le x \le L$ with the following initial and boundary conditions:

$$N(x, 0) = N_0 \exp\left(-\frac{x^2}{l^2}\right), \quad E(x, 0) = \frac{D(0)}{\epsilon(x, 0)}, \quad (12)$$

$$\left.\frac{\partial E}{\partial x}\right|_{x=0} = \left.\frac{\partial^3 E}{\partial x^3}\right|_{x=0} = \left.\frac{\partial E}{\partial x}\right|_{x=L} = \left.\frac{\partial^3 E}{\partial x^3}\right|_{x=L} = 0. \quad (13)$$

Initial condition (12) for $l \ll L$ corresponds to a situation in which small initial (seed) perturbations are localized in a narrow spatial region. Boundary conditions (13) correspond to solutions that are spatially periodic (with a period of $2L$) in the entire space and are mirror symmetric with respect to the ends of the integration interval.

The results of numerical simulations for the case $D = D_0$ = const are presented in Figs. 2–4 in the dimensionless units

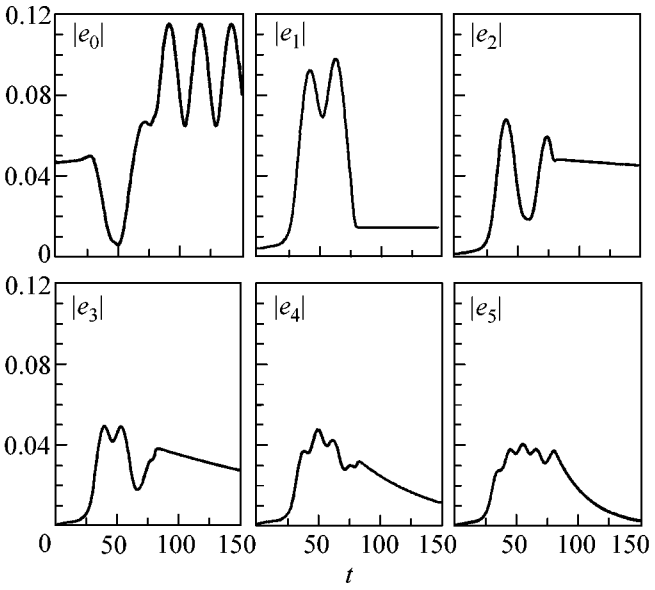

Fig. 3. Time behavior of the amplitudes of the spatial field harmonics for D = const.

$$\begin{aligned} x/L &\longrightarrow x, \quad \omega t \longrightarrow t, \\ E/E_a &\longrightarrow E, \quad n = N/N_c. \end{aligned} \quad (14)$$

The calculations were performed for the following dimensionless parameters: $D_0/E_a = 0.045$, $N_0/N_c = 0.2$, $\Omega/\omega = 25$, $L/l = 6$, $L/\delta = 30$, $\nu/\omega = 0$, and $N_g/N_c = 1.5$. These dimensionless parameters approximately correspond to the following conditions of real experiment on gas breakdown in laser field: the electromagnetic wavelength in a vacuum is $\lambda_0 \approx 1$ μm, the laser intensity is $S \approx 0.6 \times 10^{14}$ W/cm^2, and the gas pressure is $p \approx 50$ atm. If we assume that the characteristic thermal velocity V_T, which determines the parameter of spatial dispersion δ in Eq. (2), is on the order of the oscillatory electron velocity in the plasma resonance region (where, as follows from the calculated results presented below, the field amplitude attains a value of $|E| \approx (0.1–0.15)E_a$), then, for the remaining dimensional parameters of the problem, we obtain $V_T \approx 4 \times 10^8$ cm/s, $\delta \approx 4 \times 10^{-7}$ cm, $l \approx 2 \times 10^{-6}$ cm, and $L \approx 10^{-5}$ cm. We note that the required gas pressure can be substantially reduced as compared to the above value by using laser radiation with a longer wavelength or a gas whose atoms can be multiply ionized.

Figure 2 shows the spatiotemporal evolution of the plasma density $n(x, t)$ and the electric field amplitude $|E(x, t)|$. Figure 3 illustrates the dynamics of the spatial spectrum (the first six spatial harmonics) of the electric field, which is represented as

$$E(x, t) = \sum_{j=0}^{\infty} e_j(t) \cos(\pi j x/L). \quad (15)$$

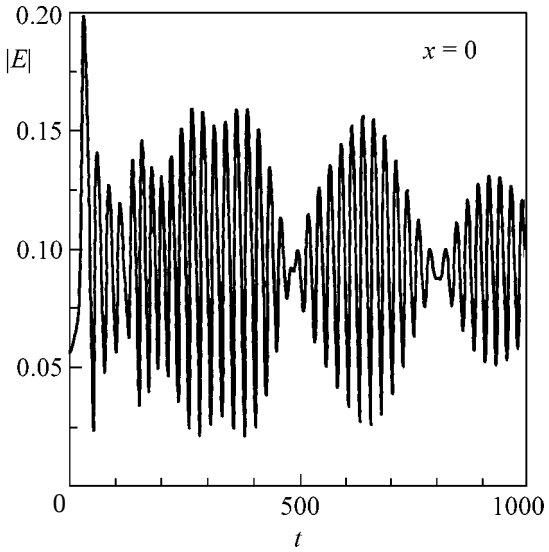

Fig. 4. Time behavior of the field amplitudes at the point $x = 0$ for $D = \text{const}$.

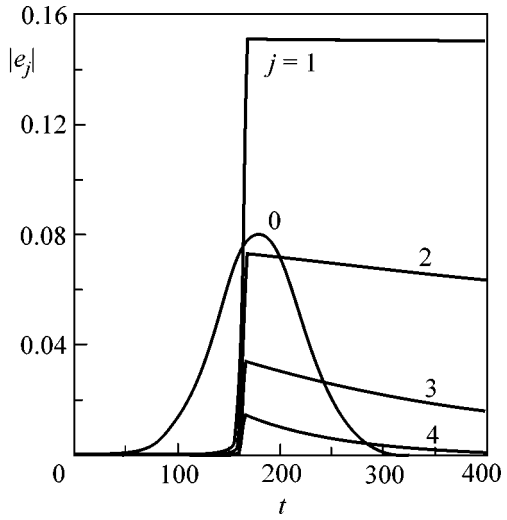

Fig. 5. Time behavior of the amplitudes of the spatial field harmonics, $|e_j(t)|$, for a given (Gaussian) envelope of the average field $\bar{E} = e_0(t)$.

Figures 4 depicts the temporal evolution of the modulus of the complex field amplitude at the point $x = 0$. Three main stages can be distinguished in the field and plasma evolution during the breakdown. In the first stage ($0 < t < t_1 \approx 30$; Fig. 2, curves corresponding to the times $t = 0$ and 27), the peak plasma density $n(0, t)$ grows at a progressively increasing rate and reaches its maximum value. In the second stage ($t_1 < t < t_2 \approx 80$; Fig. 2, curves corresponding to the times $t = 45$, 61, 77, and 85), which begins when the plasma density at the point $x = 0$ passes through the critical value, intense Langmuir oscillations are excited and a fast ionization wave is formed. The propagation velocity of this wave is determined by the processes of the excitation and transportation of Langmuir waves near the wave front where the plasma density changes abruptly and where the plasma resonance point is located. In the example under consideration, this velocity is approximately equal to the electron thermal velocity V_T and is substantially higher than the ionization wave velocity calculated for the same parameters, but without allowance for the excitation of Langmuir waves (i.e., at $\delta = 0$). After the wave front traverses the entire integration region ($t > t_2$), the discharge passes into the third stage, in which the gas is fully ionized; the density is constant both in time and space ($N = N_g$, $\epsilon_s = 1 - N_g/N_c$); and, as follows from Eq. (3), the amplitudes $e_j(t)$ of the spatial field harmonics vary according to the law

$$e_0(t) = \frac{D}{\epsilon_s} + \left(e_0(t_2) - \frac{D}{\epsilon_s}\right)\exp(-i\Delta\omega_0 t');$$
$$e_j(t) = e_j(t_2)\exp(-i\Delta\omega_j t') \quad (j = 1, 2, 3, \ldots), \tag{16}$$

where $t' = t - t_2$. According to Eq. (3), in the parabolic approximation used ($|\Delta\omega_j| \ll \omega$), the complex frequencies $\Delta\omega_j$ of the harmonics (which are in fact the frequency shifts of the excited Langmuir harmonics with respect to the frequency ω of the external field) are determined by the expression

$$\Delta\omega_j = \frac{1}{2}\omega((j\delta\pi/L)^2 - \epsilon_s - i(j\delta\pi/L)^4), \quad (j = 0, 1, 2, 3, \ldots). \tag{17}$$

We note that these frequencies can be calculated more accurately by using the exact dispersion relation for Langmuir waves. The initial amplitudes $e_j(t_2)$ of the damped Langmuir harmonics in expression (16) can be calculated numerically (Fig. 3 presents the amplitudes of the first six harmonics over a fairly wide time interval also including the instant $t = t_2$).

The above breakdown scenario has much in common with scenarios calculated for another initial density profiles and another methods for specifying the electric induction amplitude $D(t)$. Figure 5 presents the calculated temporal evolution of the amplitudes of the first five spatial field harmonics for a version in which the tunneling ionization of a gas by a femtosecond laser pulse was modeled for a given (Gaussian) envelope of the average electric field $\bar{E}(t)$ in a plasma,

$$\bar{E} = e_0 = A\exp(-(t - t_0)^2/\tau^2). \tag{18}$$

Calculations were performed for the initial conditions corresponding to a sinusoidal density modulation against the uniform background density,

$$n = n_0 + n_1\cos(\pi x/L), \tag{19}$$

for the following parameters: $A = 0.08$, $\tau = 60$, $t_0 = 180$, $n_0 = 0.1$, and $n_1 = 0.03$, the other parameters being the

same as in the previous version. It can be seen in Fig. 5 that, in a certain breakdown stage ($t > 160$), along with the given Gaussian zeroth harmonic $e_0(t)$, a set of Langmuir harmonics with amplitudes $e_j \sim e_{0\max} = A$ arise in the plasma (the amplitude of the first harmonic e_1 is twice as large as $e_{0\max}$). After the gas has been fully ionized, the harmonic amplitudes slowly decrease due to Landau damping.

Therefore, both of the above examples demonstrate the intense generation of Langmuir oscillations during gas breakdown and the formation of a relatively long-lived quasi-turbulent state characterized by a large number of spatial Langmuir harmonics with different wavenumbers and different eigenfrequencies in the final stage of breakdown.

2.4. Two-Dimensional Boundary Problem

The above approach can be generalized to a two-dimensional boundary problem that allows us to describe the generation of small-scale field–plasma structures during the breakdown of a gas slab (or half-space filled with a gas) by a finite-duration laser pulse. Below, we formulate the problem, briefly describe the solution method, and present some numerical results (see also [32]).

Let a Gaussian laser pulse with frequency ω and electric field parallel to the x axis be incident from a vacuum onto a plane gas slab (which occupies the region $0 < z < L_z$) along its normal (which is parallel to the z axis) and produce a plasma via tunneling ionization of the gas atoms. We assume that the initial electron density N in the gas is much lower than the critical density N_c and is slightly modulated (in order to ensure seed perturbations for the onset of PRII) along the x axis. The modulation period $2L_x$ is assumed to be small as compared to the electromagnetic wavelength, the gas slab thickness L_z and the characteristic longitudinal scale l_z of the arising structures. The electric field is described under the assumption that the field envelope is a slowly varying function of time. Owing to the inequalities $L_x \ll c/\omega, l_z$, the electric field remains quasi-transverse, $\tilde{\mathbf{E}} = (1/2)\mathbf{x}_0 E(x, z, t)\exp(-i\omega t) + \text{c.c.}$, in spite of the formation of inhomogeneous plasma structures stretched along the z axis.

The method for describing the field evolution is based on the separation of long (electromagnetic) and short (Langmuir) spatial scales. The complex amplitude $E(x, z, t)$ is assumed to be a periodic (with the period $2L_x$) function of x and a slowly varying (on the scale L_x) function of z. The small-scale (transverse) field structure is described by the quasi-one-dimensional equation

$$\epsilon E + \frac{2i}{\omega}\frac{\partial E}{\partial t} + \delta^2\frac{\partial^2 E}{\partial x^2} + \hat{\Gamma}E = -\frac{c^2}{\omega^2}\frac{\partial^2 \bar{E}}{\partial z^2}, \qquad (20)$$

which generalizes one-dimensional phenomenological equation (3) by taking into account the slow dependence of the average (macroscopic) field $\bar{E} = L_x^{-1}\int_0^{L_x} E\,dx$ on the longitudinal coordinate z, which enters into Eq. (20) as a parameter.

The long-scale (longitudinal) structure is described by the parabolic equation for the average field,

$$\frac{c^2}{\omega^2}\frac{\partial^2 \bar{E}}{\partial z^2} + \frac{2i}{\omega}\frac{\partial \bar{E}}{\partial t} + \overline{\epsilon E} = 0, \quad \overline{\epsilon E} = \frac{1}{L_x}\int_0^{L_x}\epsilon E\,dx \qquad (21)$$

with the radiation conditions at the slab boundaries:

$$\left(\frac{\partial \bar{E}}{\partial z} + i\frac{\omega}{c}\bar{E}\right)\Big|_{z=0} = 2i\frac{\omega}{c}E_0^{(i)}(t),$$
$$\left(\frac{\partial \bar{E}}{\partial z} - i\frac{\omega}{c}\bar{E}\right)\Big|_{z=L_z} = 0, \qquad (22)$$

where $E_0^{(i)}(t)$ is the amplitude of the incident wave at the inlet boundary of the slab ($z = 0$).

Equations (2), (4), (11), (20), and (21) were solved numerically in the region $0 \le x \le L_x$, $0 \le z \le L_z$ under the initial conditions

$$E(x, z, 0) = 0,$$
$$N(x, z, 0) = \left(N_0 + N_1\cos\left(\frac{\pi x}{L_x}\right)\right)f(z) \qquad (23)$$

for the given time dependence of the incident wave amplitude

$$E_0^{(i)}(0 \le t \le 2t_0) = A\left(\exp\left(-\left[\frac{t - t_0}{t_1}\right]^2\right) - \exp\left(-\left[\frac{t_0}{t_1}\right]^2\right)\right), \quad E_0^{(i)}(t \ge 2t_0) = 0, \qquad (24)$$

and the given initial profile of the gas density $N_g(z) = N_{g\max} f(z)$

$$f(0 \le z \le z_1) = \sin^2\left(\frac{\pi z}{2z_1}\right),$$
$$f(z_1 \le z \le z_2) = 1,$$
$$f(z_2 \le z \le L_z) = \cos^2\left(\frac{\pi(z - z_2)}{2(L_z - z_2)}\right). \qquad (25)$$

The results of numerical calculations are presented in Fig. 6–8 in dimensionless units that differ from units (14) only in another unit of length: $(\omega/c)x \longrightarrow x$ and $(\omega/c)z \longrightarrow z$. The calculations were performed for the following parameter values: $\Omega/\omega = 25$, $\delta\omega/c = 0.01$, $\nu = 0$, $N_{g\max} = 1.2N_c$, $A/E_a = 0.07$, $t_0\omega = 85$, $t_1\omega = 60$, $L_z\omega/c = 2$, $z_1\omega/c = 0.2$, $z_2\omega/c = 1.8$, $L_x\omega/c = 0.3$, $N_0/N_c = 0.03$, and $n_1 = N_1/N_c = 0.003$. These parameter values

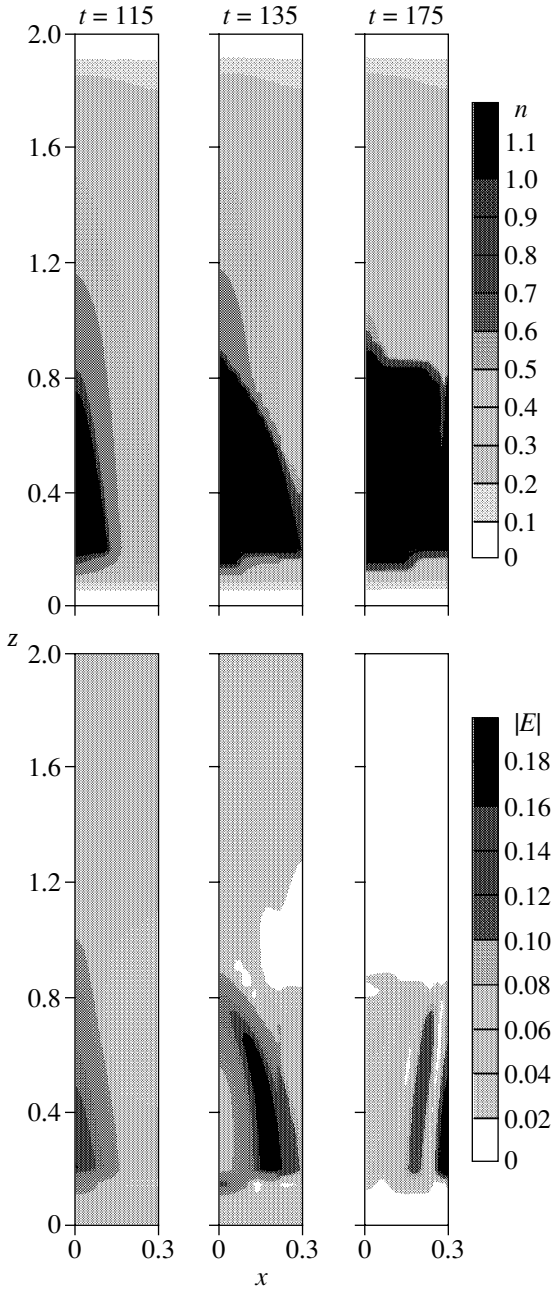

Fig. 6. Two-dimensional evolution of the plasma density $n(x, z, t)$ and the field amplitude $|E(x, z, t)|$ in a gas slab during the intense excitation of Langmuir oscillations.

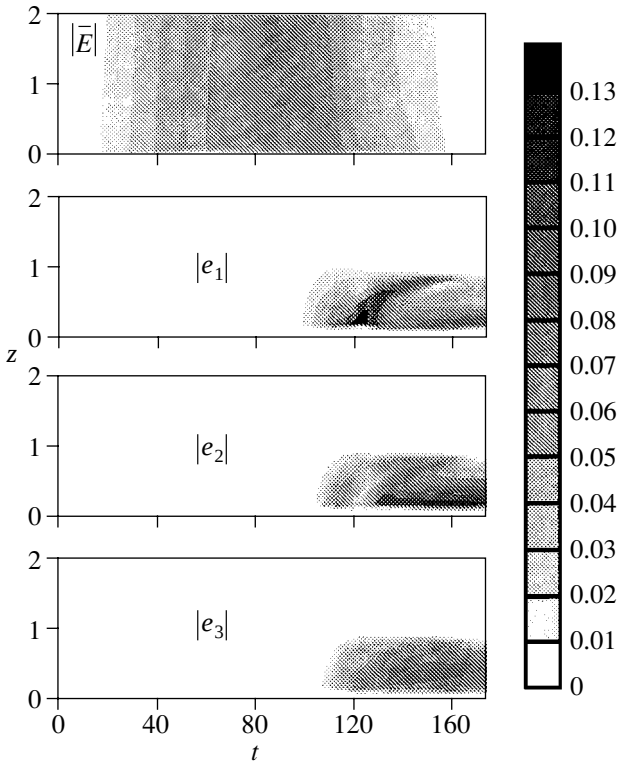

Fig. 7. Evolution of the spatial field spectrum $|e_j(x, z, t)|$ (j = 0, 1, 2, 3; $e_0 = \bar{E}$) under the same conditions as in Fig. 6.

correspond to the laser wavelength $\lambda_0 \approx 1$ μm, the peak intensity $S \approx 1.4 \times 10^{14}$ W/cm^2, the pulse duration (at a level of $1/e$ of the peak intensity) $\sqrt{2}\,t_1 \approx 50$ fs, and the pressure $p \approx 40$ atm. The evolution of the field and plasma during breakdown is shown in Fig. 6, which presents the spatial distributions of the plasma density $n(x, z)$ and the modulus of the complex field amplitude $|E(x, z)|$ for different times t. It can be seen that the gas is highly ionized in a gas layer of thickness $\Delta z \approx 0.8$. In each cross section z = const of this layer, the main breakdown stages are the same as in the one-dimensional problem considered above: (i) the growth of the maximum plasma density in the plane $x = 0$ and the formation of a thin (first critical and then fully ionized) layer stretched along the z axis, (ii) the expansion of this layer over x in the course of propagation of a fast (with a velocity of $\sim V_T$) ionization wave sustained by the field of the excited Langmuir waves, and (iii) the coalescence of two ionization waves propagating in opposite directions and the formation of a fully ionized homogeneous plasma layer of thickness Δz with slowly damping Langmuir harmonics excited in it. The wavenumbers and eigenfrequencies of these harmonics (except for the zeroth harmonic, which coincides with the average field $\bar{E}$) are described by the same expressions (15)–(17) as in the one-dimensional problem. The spatiotemporal evolution of the average field $\bar{E} = e_0$ and the amplitudes of the first three Langmuir harmonics (j = 1, 2, and 3) in the course of ionization is shown in Fig. 7. For the chosen parameters (which correspond to the case of a relatively weak reflection of the incident wave from the plasma), this evolution turned out to be close to that calculated above for a given Gaussian time dependence of the average field $\bar{E}(t)$.

The role of both the ionization instability under study and the related generation of Langmuir waves during gas breakdown is illustrated in Fig. 8, which

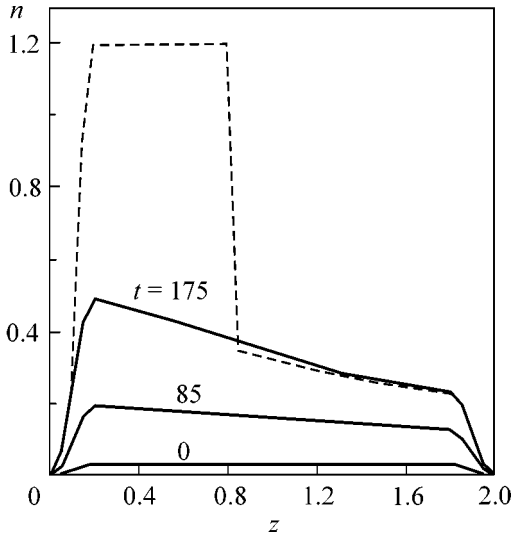

Fig. 8. Longitudinal profiles of the plasma density in a gas slab in the absence of instability ($n_1 = 0$) and under developed instability (dashed curve; $n_1 = 0.003$, $t = 175$, and $x = 0.15$).

shows the calculated spatial profiles of the plasma density $n(z)$ in the slab at times $t = 0$, 85, and 175 for the case where small-scale seed plasma-density perturbations, which are required for the onset of instability, are absent ($n_1 = 0$, the other parameters being the same as in Figs. 6 and 7). The dashed curve shows the profile $n(z)$ at the instant $t = 175$ (after the electromagnetic pulse has already passed through the slab) for $n_1 = 0.003$, i.e., under conditions corresponding to the generation of intense Langmuir waves. It can be seen that, in the absence of instability, the gas is everywhere incompletely ionized and the plasma density does not exceed a value of $N = 0.5N_c$, whereas the onset of instability results in the formation of a completely ionized plasma slab with $N = 1.2N_c$. It is interesting that, in the latter case, in spite of the formation of an overcritical plasma slab, the field amplitude and the total energy of radiation transmitted through the slab decrease only slightly. The energies of transmitted and reflected radiation are 92.5 and 3.3% of the incident pulse energy, respectively; 4.2% of the total energy is transformed into Langmuir oscillations. The low fraction of radiation reflected from a fairly thick plasma slab with an overcritical density can be explained by the effect of delayed ionization, which is mainly produced by the excited Langmuir waves after most of the incident radiation have already passed through the slab (rather than by the electric field of the pulse itself). We note, however, that, as applied to a real experiment, such small losses of the pulse energy can only be regarded as a rough estimate, because, in calculations, a number of other mechanisms for energy losses (such as electron collisions and energy losses related to both the detachment of electrons from atoms and the directed velocity that is acquired by an electron at the instant of detachment and that depends on the field phase at this instant) were not taken into account. Although, under conditions of gas ionization by high-intensity radiation and in the adopted parabolic approximation, these losses are small, they may be comparable with the small energy losses obtained above.

3. DISCHARGE IN A BESSEL WAVE BEAM

In this section, we consider resonance phenomena accompanying gas breakdown in the field of a Bessel wave beam. Such a beam, which is a cylindrical wave propagating at a certain angle θ to the z axis, can be produced by focusing laser radiation by an axicon lens. An extended filamentary discharge excited in the focal region of such a lens attracts considerable attention because of the possibility of using it for the channeling of electromagnetic radiation in the modern projects of X-ray lasers and laser–plasma accelerators. A number of problems related to axicon breakdown were investigated both experimentally and theoretically (in the scalar approximation) [23, 33, 34]. A possible role of Langmuir oscillations in the formation of the spectrum of radiation scattered by such a discharge [23] was pointed out; however, the problems of the resonance excitation of Langmuir oscillations and their influence on the discharge dynamics (i.e., the problems in which we are interested here) were not discussed or analyzed. These problems can adequately be investigated only in the framework of a self-consistent vector problem for an electromagnetic field in a nonsteady plasma with allowance for spatial dispersion. The formulation of such a problem in a simple model of a longitudinally uniform axisymmetric discharge in the field of a circularly polarized cylindrical wave and the results of numerically solving this problem are presented below (some of these results were also reported in [35]).

The basic vector equation for the slowly varying envelope of the electric fields in plasma has the form

$$\frac{2i}{\omega}\frac{\partial \mathbf{E}}{\partial t} + \delta^2\nabla(\nabla\cdot\mathbf{E}) + \epsilon\mathbf{E} - \frac{1}{k_0^2}[\nabla\times[\nabla\times\mathbf{E}]] + \hat{\Gamma}\mathbf{E} = 0. \quad (26)$$

We are interested here in such solutions to this equation that, in the absence of a discharge (at $N \equiv 0$), describe the field of a Bessel wave beam with a circularly polarized transverse component, which has a maximum on the axis:

$$\mathbf{E}_\perp^{(0)} \sim (\mathbf{x}_0 + i\mathbf{y}_0)J_0(k_\perp r)\exp(ik_z z). \quad (27)$$

Here, $\mathbf{x}_0$ and $\mathbf{y}_0$ are the unit vectors along the corresponding transverse Cartesian axes; r, φ, and z are the cylindrical coordinates; $k_z = k_0\cos\theta$ and $k_\perp = k_0\sin\theta$ are the longitudinal and transverse wavenumber, respectively; $k_0 = \omega/c$ is the wavenumber in free space; θ is the

convergence angle of a cylindrical wave; and J_0 is the zero-order Bessel function. In fact, such a beam is a "hybrid" (EH) wave, i.e., a superposition of TE and TM waves with the longitudinal electric and magnetic field components, E_z and H_z, related by

$$E_z^{(0)} \sim J_1(k_\perp r)\exp(i\varphi + ik_z z), \quad H_z^{(0)} = -i\cos\theta E_z^{(0)}. \tag{28}$$

For the given type of the field symmetry, the ionization rate and the density of the plasma produced during breakdown are independent of z and φ ($N = N(r, t)$); hence, in the presence of plasma, the dependence of the desired solution to Eq. (26) on z and φ everywhere remains the same as in Eqs. (27) and (28). This allows us to rewrite Eq. (26) as a set of equations for the amplitudes of the field components E_r, E_φ, and E_z, which depend on time t and only one space coordinate r. The resulting equations (which are not presented here because of their cumbersome form) were solved numerically over the interval $0 \le r \le R$ together with Eq. (2) for the plasma density. In the latter equation, the ionization rate f, as in the previous section, was described by expression (11), which is also applicable for the qualitative description of the breakdown dynamics in the case of elliptic or circular field polarization. The radius R was chosen to be large enough for the plasma density in the region $r \sim R$ to satisfy the inequality $N(r) \ll N_c\sin^2\theta$, which allows us to neglect in this region the influence of plasma on the structure of long-scale-length (averaged over the scale length δ) solutions to Eq. (26).

In the region $r \ge R$, the field was described by Maxwell's equations for free space and was represented as a superposition of converging (incident) and diverging (reflected) cylindrical waves of the TE and TM types with given longitudinal and transverse wavenumbers k_z and $k_\perp$. The longitudinal components of the electric and magnetic fields of the incident waves were written as

$$E_z^{(i)} = C(t)H_1^{(2)}(k_0 r\sin\theta), \quad H_z^{(i)} = -i\cos\theta E_z^{(i)} \tag{29}$$

and those of the reflected waves were written as

$$E_z^{(r)} = F(t)H_1^{(1)}(k_0 r\sin\theta), \quad H_z^{(r)} = G(t)H_1^{(1)}(k_0 r\sin\theta). \tag{30}$$

Here, $H_1^{(2)}$ and $H_1^{(1)}$ are the first-order Hankel functions describing the converging and diverging waves, respectively; $C(t)$ is the given envelope of the incident pulse amplitude; and $F(t)$ and $G(t)$ are the sought-for electric and magnetic field envelopes of the reflected waves. The relation between the amplitudes of the longitudinal components of the incident TE and TM waves, $H_z^{(i)}/E_z^{(i)} = -i\cos\theta$, was chosen [as in (28)] such that the transverse field in the absence of plasma was everywhere circularly polarized and was described by expression (27) (in this case, in cylindrical coordinates, we have $E_\varphi^{(0)}(r) = iE_r^{(0)}(r) \sim J_0(k_0 r\sin\theta)$). We note that, in the presence of plasma, the field remains circularly polarized only on the axis, where we always have $E_\varphi(0) = iE_r(0)$.

The calculations were performed with the initial conditions

$$N(r, 0) = 0, \quad E_\varphi(r, 0) = iE_r(r, 0) = -2C(0)\cot\theta J_0(k_0 r\sin\theta), \quad E_z(r, 0) = 2C(0)J_1(k_0 r\sin\theta). \tag{31}$$

and the following boundary conditions: (a) the solution is analytical at the point $r = 0$,

$$E_z = 0, \quad \partial E_r/\partial r = \partial E_\varphi/\partial r = 0; \tag{32}$$

and (b) the tangential components of the electric and magnetic fields (E_z, H_z, E_φ, H_φ) and the normal component of the electric field E_r are continuous at $r = R$. The latter condition (the continuity of E_r) is the simplest version of an additional boundary condition, whose necessity stems from the presence of the term $\delta^2\nabla(\nabla\cdot\mathbf{E})$ in Eq. (26), because this term (which takes into account spatial dispersion) increases the order of the set of equations under study. In order to avoid additionally increasing this order by introducing the model fourth-order operator $\hat{\Gamma}$ (4), collisionless damping was described by the simpler second-order operator $\hat{\Gamma}\mathbf{E} = -ia\nabla(\nabla\cdot\mathbf{E})$, which, at a relevant choice of the coefficient a, provides a sufficiently accurate description of the Langmuir wave damping. Conditions (b) allow us to derive expressions that relate the components of the electric field and their normal derivatives at the boundary $r = R$ to the amplitude function $C(t)$ of the incident wave:

$$\frac{1}{k_0}\frac{\partial E_z}{\partial r} - E_z Q_1\sin\theta = CQ_2\sin\theta,$$

$$\frac{1}{k_0}\frac{\partial E_\varphi}{\partial r} - E_\varphi Q_3\sin\theta + E_z Q_4\cos\theta = CQ_5\cos\theta,$$

$$E_r + E_\varphi Q_6 + E_z Q_7\cot\theta = CQ_8\cot\theta, \quad Q_1 = \frac{h_0}{h_1} - \frac{1}{\rho},$$

$$Q_2 = -2ih_1^*\mathrm{Im}Q_1, \quad Q_3 = \frac{1}{Q_1}\left(\frac{1}{\rho^2} - 1\right) - \frac{1}{\rho}, \tag{33}$$

$$Q_4 = \frac{1}{\rho}\left(Q_1 - Q_3 - \frac{1}{\rho}\right), \quad Q_5 = -\frac{Q_2}{\rho} + 2ih_1^* Q_1^*\mathrm{Im}Q_3,$$

$$Q_6 = \frac{i}{\rho Q_1}, \quad Q_7 = i\left(\frac{1}{\rho^2 Q_1} - Q_1\right),$$

$$Q_8 = iQ_2(1 + iQ_6),$$

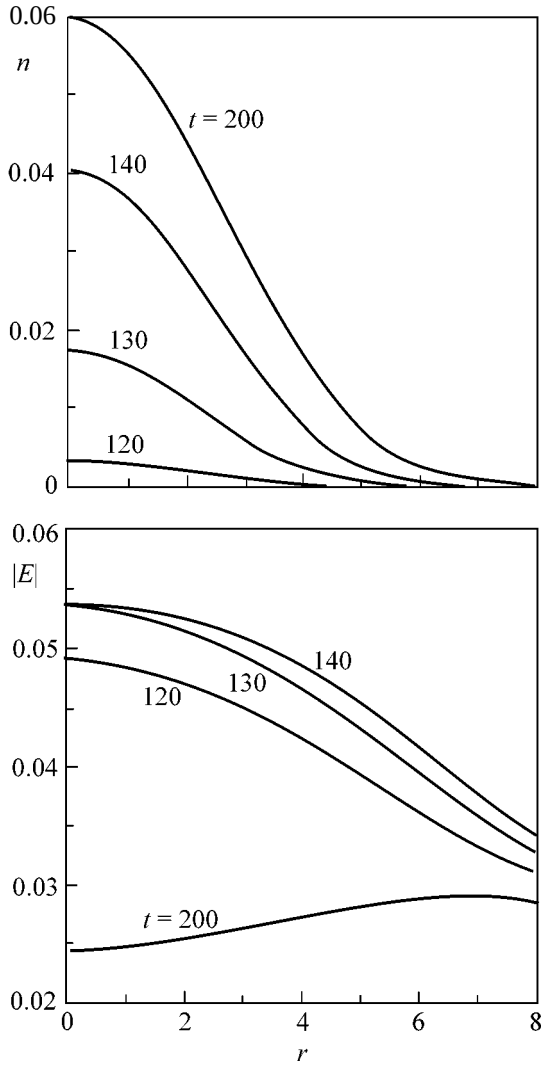

Fig. 9. Evolution of the plasma density $n(r, t)$ and the field amplitude $|\mathbf{E}(r, t)|$ in an axicon discharge for $\theta = 6°$. Numerals by the curves show the time values.

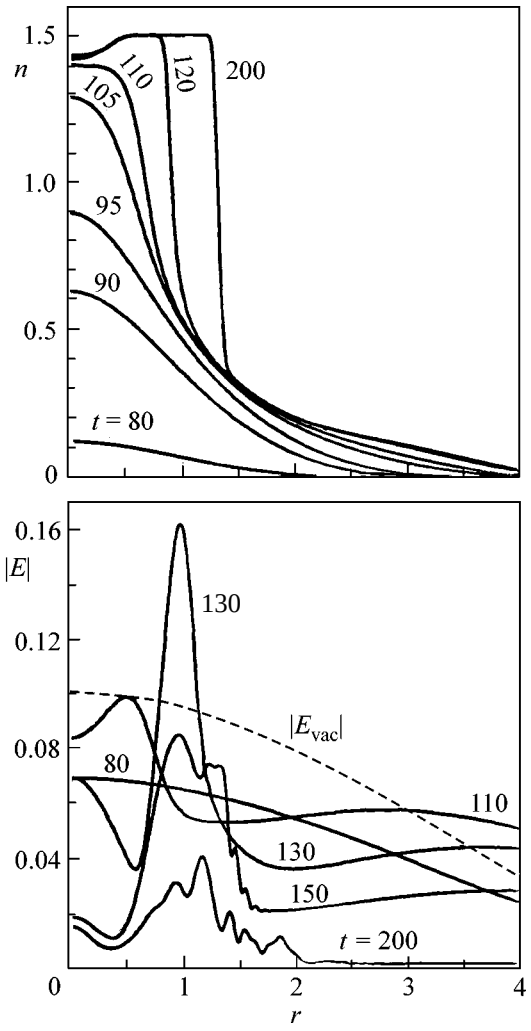

Fig. 10. Evolution of the plasma density $n(r, t)$ and the field amplitude $|\mathbf{E}(r, t)|$ in an axicon discharge for $\theta = 30°$. Numerals by the curves show the time values. The dashed curve shows the unperturbed field $|\mathbf{E}_{vac}(r)|$ (in the absence of a plasma) at the instant when the field on the axis reaches its maximum ($t \approx t_0$).

$$\rho = k_0 R \sin\theta, \quad h_0 = H_0^{(1)}(\rho), \quad h_1 = H_1^{(1)}(\rho).$$

The calculations have shown that the scenario of the process under study depends substantially on the convergence angle θ of the incident wave. If this angle is smaller than a certain critical angle $\theta_c \approx 25°$, the field and the plasma density behave according to the predictions of the scalar models [4, 6, 9, 10, 34]: the maximum of the plasma density is $N_{max}/N_c = K\sin^2\theta$, the coefficient K being in the range 3–6; hence, at small angles, we have $N_{max} \ll N_c$. However, at $\theta > \theta_c$, the process of ionization in the axial region is similar to that occurring in the nonlinear stage of PRII, which have been considered in the previous section: the plasma density and the field amplitude at the axis grow at a progressively increasing rate, and, after the plasma density have passed through the critical value, a fast ionization wave is formed that propagates in the radial direction over a distance of $r \sim k_0^{-1}$ and contains the plasma resonance point at its front.

The above characteristic scenarios of the field and plasma evolution are illustrated in Fig. 9 ($\theta = 6°$) and Figs. 10–12 ($\theta = 30°$) in same dimensionless variables that were used in Section 2: $k_0 r \longrightarrow r$, $\omega t \longrightarrow t$, $E/E_a \longrightarrow E$, and $N/N_c = n$. Figures 9 and 10 show the radial profiles of the plasma density $n(r, t)$ and the module of the electric field amplitude $|\mathbf{E}(r, t)|$ at different instants for a Gaussian envelope of the incident pulse, $C(t) = A\exp[-(t - t_0)^2/\tau^2]$, and the following parameters of the problem: $\Omega/\omega = 22$, $k_0\delta = \sqrt{3}\, V_T/c = 0.02$; $\nu/\omega = 0.01$, $a = 0.1$, $N_g = 1.5N_c$, $t_0\omega = 100$, $\tau\omega = 50$, $A/E_a =$

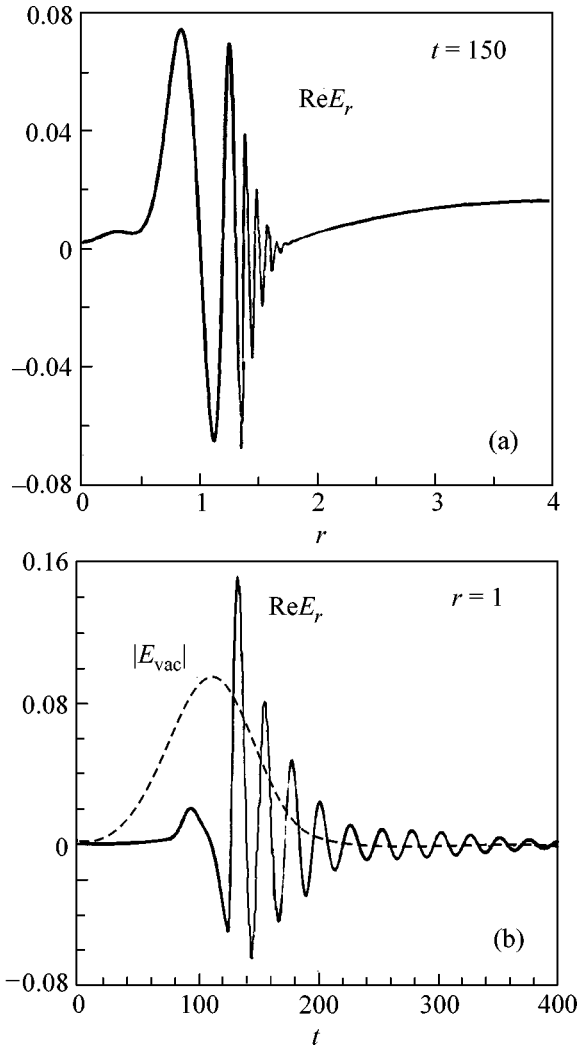

Fig. 11. Spatial and temporal behavior of Langmuir oscillations: (a) $\mathrm{Re}E_r(r)$ at $t = 150$ and (b) $\mathrm{Re}E_r(t)$ at $r = 1$. The dashed curve shows the time dependence of the amplitude of the unperturbed Gaussian pulse, $|\mathbf{E}_{\mathrm{vac}}(t)|$, at $r = 1$.

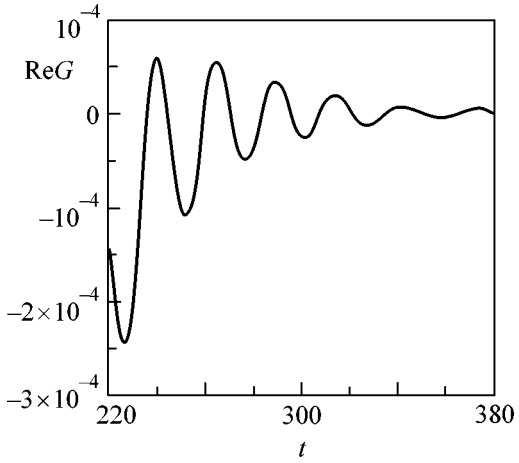

Fig. 12. Time behavior of the amplitude function $\mathrm{Re}G(t)$ of the reflected TE wave [see Eq. (30)] at large times. The curve illustrates the presence of radiation from the discharge at the upshifted frequency $\omega_{p\max} = 1.22\omega$.

0.0037 at $\theta = 6°$ and $A/E_a = 0.0204$ at $\theta = 30°$, and $k_0R = 8$ at $\theta = 6°$ and $k_0R = 4$ at $\theta = 30°$. At the given values of A, the maximum field at the axis (in the absence of plasma) is the same in both cases: $|\mathbf{E}|_{\max}/E_a = 0.1$. The above dimensionless parameters correspond to the vacuum wavelength $\lambda_0 \approx 0.8$ μm, the maximum intensity (recalculated for a homogeneous plane wave with an amplitude equal to $|\mathbf{E}|_{\max}$) $S \approx 3 \times 10^{14}$ W/cm^2, the pulse duration (at a level of $1/e$) $\tau\sqrt{2} \approx 30$ fs, and the gas pressure $p \approx 60$ atm.

The transition of the plasma density through the critical value (Fig. 10) is accompanied by the excitation of intense Langmuir oscillations, whose amplitude reaches its maximum (twice as high as the amplitude of the unperturbed electric field at the axis) at the front of the ionization wave at $r \approx 1$. The oscillating character of the Langmuir field is clearly seen in Fig. 11. Figure 11a shows the profile of $\mathrm{Re}E_r(r)$ at $t = 150$, and Fig. 11b presents the time behavior of $\mathrm{Re}E_r(t)$ at $r = 1$ ($\mathrm{Im}E_r(r, t)$ behaves in a similar way). The wavelength of Langmuir oscillations (the characteristic spatial scale of the field variations) in the region where the gas is completely ionized is on the order of the radius of this region and gradually decreases with decreasing plasma density (Fig. 11a). The oscillation period of the complex amplitude $E_r(t)$ (Fig. 11b) is determined by the frequency shift of the excited Langmuir oscillations with respect to the external field frequency ω. The amplitude of these oscillations exceeds the maximum field amplitude of the Gaussian pulse in the absence of plasma, $|\mathbf{E}_{\mathrm{vac}}(t)|$, shown for comparison in Fig. 11b by the dashed line.

The coupling of the excited Langmuir oscillations to an external electromagnetic field (due to the presence of a fairly sharp boundary of the ionized region) gives rise to the partial emission of their energy into the surrounding space, i.e., to the occurrence (along with the fundamental frequency component ω) of one or several components at frequencies close to $\omega_{p\max} = \sqrt{4\pi e^2 N_g/m} \approx 1.22\omega$ in the spectrum of the cylindrical wave reflected from the discharge. In view of the linear character of the "transition" resonant excitation of Langmuir oscillations, the intensities the shifted spectral components are proportional to the intensity of the incident wave. This linear parametric conversion of the scattered spectrum of an ionizing electromagnetic wave (previously described in the model of a thin gas slab [26]) is illustrated in Fig. 12 by the time dependence of the quantity $\mathrm{Re}G(t)$ [which, according to Eq. (30), determines the behavior of the amplitude $H_z^{(r)}(t)$ of the reflected wave] at large times $t > 220$ (after the end of

the incident pulse), when the signal amplitude at the fundamental frequency has already substantially decreased, but the Langmuir oscillations still exist and continue emitting. At $t \approx 250$, the intensity of the shifted frequency component is about 10^{-4} of the maximum intensity of the incident wave. The divergent cylindrical waves with the frequencies ω and $\omega_{p\max}$ are inclined to the symmetry axis of the discharge at different angles θ and θ_p related by $\cos\theta_p = (\omega/\omega_{p\max})\cos\theta$ (in the given numerical example, $\theta = 30°$ and $\theta_p = 45°$). A similar (annular) frequency–angular structure of radiation reflected from the plasma was actually observed in experiments on the axicon breakdowns of solid dielectrics [23], although the unambiguous interpretation of these experiments is still lacking. Another macroscopic effect that can be, in principle, verified experimentally is the transformation of radiation polarization. Calculations show that, after the plasma density have passed through the critical value, the relationship between the amplitudes E_z and H_z of the reflected wave changes abruptly; i.e., the TE and TM waves undergo transformation. In the above numerical example ($\theta = 30°$), the energy fractions of these waves in the incident pulse are 43 and 57%, respectively, whereas in the reflected wave these are 59 and 31% (10% of energy is absorbed). It can be shown that the polarization of the transverse components of the wave is transformed from circular to elliptic with the principal axis oriented in the azimuth direction.

4. CONCLUSION

The considered models of optical discharge in a dense gas show that the transition of the plasma density through the critical value is accompanied by the generation of intense Langmuir waves with amplitudes exceeding the amplitude of the laser field creating the discharge. This process leads to a substantial increase in the gas ionization rate and, after complete ionization, to the formation of a relatively long-living quasi-turbulent state, characterized by broad-spectrum Langmuir oscillations. The results obtained are of interest for various applications related to the production and implementation of laser plasmas. In our opinion, further investigations in this field should be directed to the solution of the following problems: (i) a more detailed and specified analysis of the possible macroscopic consequences of the considered effects and their experimental observation, (ii) the study of the dynamics of various types of Langmuir excitations during breakdowns of small-size objects (thin films, fibers, and atomic clusters), and (iii) the study of resonance phenomena during optical breakdowns of condensed media. One of the most important problems here is the calculation of the ionization rates and effective electron collision frequencies in strong optical fields.

This study was supported in part by the Russian Foundation for Basic Research (project nos. 99-02-16238, 02-02-17271, 01-02-16575, and 02-02-06266) and the Russian Academy of Sciences (grant no. 1999(6)-37).

REFERENCES

1. A. V. Gurevich, *Nonlinear Phenomena in the Ionosphere* (Springer-Verlag, New York, 1978).
2. Yu. P. Raizer, *Gas Discharge Physics* (Nauka, Moscow, 1987; Springer-Verlag, Berlin, 1991).
3. V. B. Gildenburg and A. V. Kim, Zh. Éksp. Teor. Fiz. **74**, 141 (1978) [Sov. Phys. JETP **47**, 72 (1978)].
4. V. B. Gildenburg, in *Nonlinear Waves* (Nauka, Moscow, 1981), p. 87.
5. W. Wo and J. S. Degroot, Phys. Fluids **27**, 475 (1984).
6. A. L. Vikharev, V. B. Gildenburg, S. V. Golubev, *et al.*, Zh. Éksp. Teor. Fiz. **94** (4), 136 (1988) [Sov. Phys. JETP **67**, 724 (1988)].
7. V. B. Gildenburg, A. V. Kim, V. A. Krupnov, *et al.*, IEEE Trans. Plasma Sci. **21**, 34 (1993).
8. S. P. Kuo, Phys. Rev. Lett. **65**, 1000 (1990).
9. W. P. Leemans, C. E. Clayton, W. B. Mori, *et al.*, Phys. Rev. A **46**, 1091 (1992).
10. S. C. Rae, Opt. Commun. **104**, 330 (1994).
11. Yu. M. Aliev, A. V. Maximov, U. Kortshagen, *et al.*, Phys. Rev. E **51**, 6091 (1995).
12. V. B. Gildenburg, A. G. Litvak, and N. A. Zharova, Phys. Rev. Lett. **78**, 2968 (1997).
13. T. M. Antonsen, Jr. and Z. Bian, Phys. Rev. Lett. **82**, 3617 (1999).
14. A. M. Sergeev, M. Lontano, A. V. Kim, *et al.*, Laser Part. Beams **17**, 129 (1999).
15. L. Berge and A. Couairon, Phys. Plasmas **7**, 210 (2000).
16. C. S. Liu and V. K. Tripathi, Phys. Plasmas **7**, 4360 (2000).
17. V. B. Gildenburg and N. V. Vvedenskii, Phys. Plasmas **8**, 1953 (2001).
18. A. L. Vikharev, V. B. Gildenburg, O. A. Ivanov, and A. N. Stepanov, Fiz. Plazmy **10**, 165 (1984) [Sov. J. Plasma Phys. **10**, 96 (1984)].
19. V. B. Gildenburg and A. A. Solodov, Pis'ma Zh. Éksp. Teor. Fiz. **62**, 535 (1995) [JETP Lett. **62**, 551 (1995)].
20. V. B. Gildenburg, V. E. Semenov, and N. V. Vvedenskii, Physica D (Amsterdam) **152–153**, 714 (2001).
21. N. V. Vvedenskii, V. B. Gildenburg, and A. A. Solodov, Izv. Vyssh. Uchebn. Zaved., Prikl. Nelineĭnaya Din. **8**, 3 (2000).
22. D. Giulietti, L. A. Gizzi, A. Giulietti, *et al.*, Phys. Rev. Lett. **79**, 3194 (1997).
23. A. A. Babin, A. M. Kiselev, K. I. Pravdenko, *et al.*, Usp. Fiz. Nauk **169**, 80 (1999).
24. T. Ditmire, E. Springate, J. W. G. Tisch, *et al.*, Phys. Rev. A **57**, 369 (1998).
25. A. M. Bystrov and V. B. Gildenburg, Fiz. Plazmy **27**, 71 (2001) [Plasma Phys. Rep. **27**, 68 (2001)].
26. M. I. Bakunov, A. M. Bystrov, and V. B. Gildenburg, Phys. Plasmas **9**, 2803 (2002).

27. V. E. Zakharov, in *Basic Plasma Physics*, Ed. by A. A. Galeev and R. N. Sudan (Énergoatomizdat, Moscow, 1984; North-Holland, Amsterdam, 1984), Vol. 2.

28. S. V. Bulanov, L. M. Kovrizhnykh, and A. S. Sakharov, Zh. Éksp. Teor. Fiz. **72**, 1810 (1977) [Sov. Phys. JETP **45**, 949 (1977)].

29. M. I. Bakunov and Yu. M. Sorokin, Izv. Vyssh. Uchebn. Zaved., Radiofiz. **32**, 122 (1989).

30. P. B. Corcum, N. H. Burnett, and F. Brunel, Phys. Rev. Lett. **62**, 1259 (1989).

31. N. H. Burnett and P. B. Corcum, J. Opt. Soc. Am. B **6**, 1195 (1989).

32. N. V. Vvedenskii and V. B. Gildenburg, in *Proceedings of the Conference on Physics of Low-Temperature Plasmas, Petrozavodsk, 2001*, Vol. 1, p. 20.

33. L. Ya. Margolin, L. Ya. Polonskiĭ, and L. N. Pyatnitskiĭ, Pis'ma Zh. Tekh. Fiz. **13**, 218 (1987) [Sov. Tech. Phys. Lett. **13**, 89 (1987)].

34. H. M. Milchberg, T. R. Clark, C. G. Durfee III, *et al.*, Phys. Plasmas **3**, 2149 (1996).

35. V. B. Gildenburg and N. V. Vvedenskii, in *Proceedings of the 29th EPS Conference on Plasma Physics and Controlled Fusion, Montreux, 2002*, ECA **26B**, paper no. P-2.011.

Translated by A. Sakharov

JETP Letters, Vol. 76, No. 6, 2002, pp. 394–400. Translated from Pis'ma v Zhurnal Éksperimental'noĭ i Teoreticheskoĭ Fiziki, Vol. 76, No. 6, 2002, pp. 455–462.

SUMMARY OF THE STUDIES SUPPORTED BY THE RUSSIAN FOUNDATION FOR BASIC RESEARCH PROJECT NO. 99-02-16238

Tunneling and Andreev Spectroscopies of High-T_c Superconductors

Ya. G. Ponomarev[1] and E. G. Maksimov[2]

[1]*Faculty of Physics, Moscow State University, Vorob'evy gory, Moscow, 119899 Russia*

[2]*Lebedev Physical Institute, Russian Academy of Sciences, Leninskiĭ pr. 53, Moscow, 117924 Russia*

Received August 9, 2002

Tunneling spectroscopic studies of high-temperature superconductors (HTSC) are overviewed. It is demonstrated, in particular, that the superconducting gaps determined from Andreev reflections and tunneling current–voltage characteristics coincide at all doping levels. Facts are presented evidencing the strong electron–phonon interaction in the HTSC systems. The nature of the so-called pseudogap, which is observed in some tunneling experiments, is briefly discussed. © *2002 MAIK "Nauka/Interperiodica".*

PACS numbers: 74.20.-z; 74.50.+r; 74.72.-h; 74.80.Dm

1. INTRODUCTION

Although the theoretical and experimental studies of the nature of high-T_c superconductivity are far from completion, vast experimental material has been accumulated during 15 years of studying high-temperature superconductors (HTSC) by the most up-to-date experimental methods, and theoretical models were developed for the description of the unique properties of HTSC materials. Note that, up to the present time, the pairing mechanism has been the subject of controversy [1–8], although the isotope effect observed in the underdoped and overdoped superconducting cuprates and some other phenomena indicate that phonons play an important role in the formation of superconducting properties of HTSC materials [2, 8].

According to modern concepts [9–11], the doped crystals of most anisotropic superconducting cuprates $Bi_2Sr_2Ca_{n-1}Cu_nO_{2n+4+\delta}$, $Tl_2Ba_2Ca_{n-1}Cu_nO_{2n+4+\delta}$, and $HgBa_2Ca_{n-1}Cu_nO_{2n+4+\delta}$ are natural superlattices of the S–I–S–I– … type, where S is a thin superconducting block containing one or several calcium-intercalated CuO_2 planes and I is an insulating layer (spacer), which, in particular, provides doping of the CuO_2 blocks upon the introduction of excess oxygen into the central part of the spacer. Since the dopant is outside the CuO_2 blocks, it does not strongly affect the hole relaxation time in the CuO_2 planes. The introduction of impurities (both magnetic and nonmagnetic) into the CuO_2 plane suppresses superconductivity. In HTSC cuprates, the spacers occupy up to 80% of crystal volume, and only 20% of its volume is occupied by the superconducting CuO_2 blocks. The spacers play an important role in the *c*-directed electron transport because of the resonance tunneling [10].

At $T < T_c$, the doped HTSC crystal behaves as a stack of strongly coupled Josephson junctions, and, hence, the superconducting current in the *c* direction has the Josephson character (weak superconductivity). It is worth noting that the specificity of the superconducting properties of layered crystals with the Josephson interlayer interaction was discussed in detail well before the discovery of HTSC materials [12, ch. 6].

In cuprates, the CuO_2 plane with half-filled 2D band is unstable against the transition to Mott's insulator phase and against the formation of long-range antiferromagnetic order. Weak doping with oxygen destroys the antiferromagnetic long-range order. It is likely that further doping leads to the metal–insulator transition and to the appearance of the open hole Fermi surface [13]. In this case, the Fermi level may fall within the vicinity of an extended Van Hove singularity [14, 15]. It should be noted that the experimentally studied Fermi surface in optimally doped cuprate compounds coincides, to a good accuracy, with the one calculated theoretically by the density-functional technique [13].

High-temperature superconductivity in the CuO_2 planes arises in a relatively narrow range of doping level *p*. However, the physical nature of parameter *p* still remains to be clarified. The matter is that the Fermi surface area and, hence, the total hole concentration change only slightly in the doping range corresponding to superconductivity. This fact was pointed out both in works devoted to studying the optical properties of HTSC materials [16] and in the angle-resolved photoemission spectroscopic (ARPES) experiments. Instead

of an appreciable decrease in the Fermi surface area with decreasing doping level, an anisotropic "pseudogap" arises at the surface [17, 18]. The nature of this phenomenon is unclear. The photoemission data suggest [19] that the superconducting gap is maximal in the Γ–M direction, i.e., in the direction where the pseudogap is maximal, and it is minimal in the Γ–Y direction. In the presence of the extended Van Hove singularity at the Fermi level, the quasiparticle density of states is also maximal in the Γ–M direction. The gap anisotropy decreases appreciably with increasing doping level [20].

To first approximation, the critical temperature T_c changes with p following the parabolic law [20].

2. SOME EXPERIMENTAL RESULTS OBTAINED FOR THE HTSC MATERIALS BY TUNNELING AND ANDREEV SPECTROSCOPIES

The methods of tunneling and Andreev (microjunction) spectroscopies, as applied to HTSC materials, have demonstrated that they are quite efficient and allow the obtaining of valuable information on the physical properties of these materials in their superconducting and normal states. Below, we briefly discuss some recent experimental results obtained by the tunneling and microjunction measurements on the HTSC samples.

2.1. Internal Josephson Effect and Characteristic Properties of the S–I–S–I … Structure.

The discovery and investigation of the internal Josephson effect (IJE) [21–27] in the cuprate superconductors is among the most significant achievements of the last years, because it clearly demonstrates the 2D character of electron transport in HTSC materials. The detailed studies of IJE in various HTSC systems have culminated in the development of a new method of studying layered superconductors, namely, the method of *internal tunneling spectroscopy.*

The studies of the internal Josephson effect in HTSC mesa structures fully confirmed the S–I–S–I … model. (i) At $T < T_c$, multibranched current–voltage characteristics (CVCs) are observed for the c-directed current in mesas [21–23]; (ii) the CVCs of mesas show geometrical Fiske resonances [25]; (iii) the critical Josephson current, as a function of an external magnetic field, exhibits Fraunhofer oscillations in mesas [26]; and (iv) the microwave radiation is observed from the mesa structures upon passing above-critical current through the HTSC mesa structures [21–23].

2.2. Internal Josephson Effect; the Determination of Superconducting Gap and the Shape of CVC Curves

In [27], the internal Josephson effect was observed in the doped single crystals Bi-2212 at the natural ultrathin steps (of height from 1.5 to 30 nm), which always present at the surface of cryogenic cleavages (break junction technique). The direct STM measurements showed that the height of these steps is proportional to half of the unit cell $c/2$ = 1.5 nm (the cleavage plane passes between two BiO planes) [28, 29]. Note that half of the unit cell in the c direction corresponds to one Josephson junction.

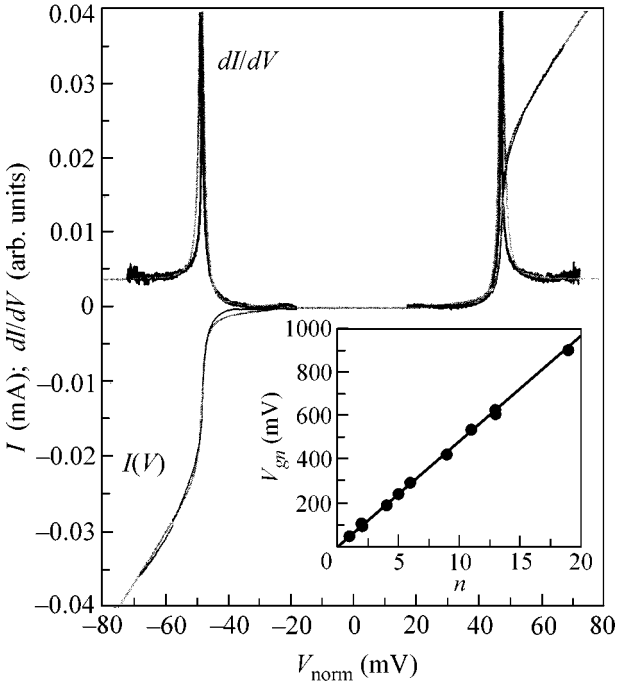

Fig. 1. CVC (normalized to one contact; $V_{\text{norm}} = V/N$) of a microstep at the cryogenic cleavage in underdoped Bi-2212(La) single crystal with the number of contacts N = 13 at T = 4.2 K (T_c = 81 ± 3 K). The dotted line is for the Dines model with parameters per contact Δ_s = 24 meV, Γ = 0.5 meV, and R_n = 1700 Ω. Inset: the dependence of gap voltage V_g on the number N of SIS contacts in microsteps of various height, as obtained in one experiment.

According to the data in [28, 29], the microstep width does not exceed 1 μm. This result coincides with the estimates made in [27]. By changing the junction using a micrometer screw, one can pass from one step to the other in one experiment and record alternately their CVCs (**j** ∥ **c**).

At helium temperature, the authors of [27] observed well-defined gap structure in the CVCs of microsteps at the surfaces of cryogenic cleavages in the underdoped and optimally doped Bi- 2212(La) single crystals and in the overdoped Bi-2212 single crystals and whiskers (Fig. 1). The stacks of $1 \le n \le 25$ Josephson junctions were studied. A high resistance of stacks ($R_{n4.2\,\text{K}}$ = 200–1500 Ω per junction) allowed the voltage range to be increased higher than the gap bias V_{gn} without any appreciable junction overheating. For the stack of n equivalent junctions, the gap bias V_{gn} corresponding to a sharp increase in the quasiparticle current $\mathbf{j_{qp}} \parallel \mathbf{c}$ is

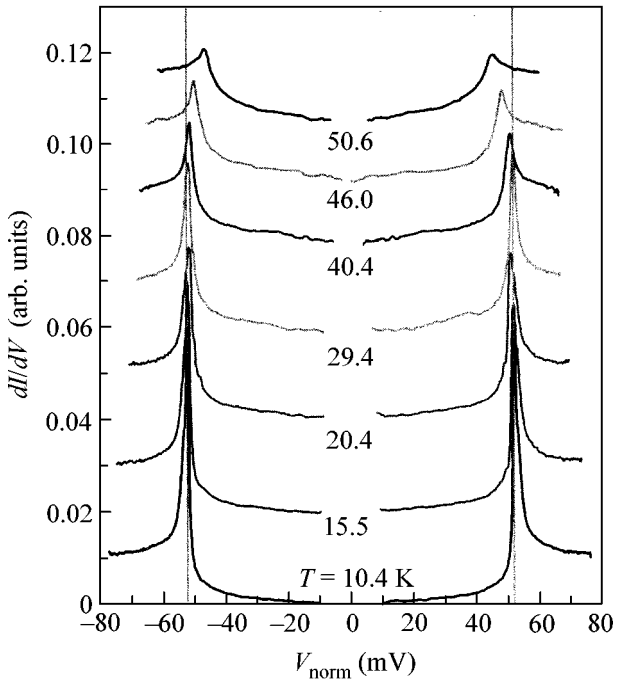

Fig. 2. Influence of temperature on the $dI(V)/dV$ characteristics (normalized to one contact) of a microstep at the cryogenic cleavage in underdoped Bi-2212(La) single crystal with the number of contacts $N = 18$ ($T_c = 87 \pm 2$ K).

given by the expression $V_{gn} = (2\Delta/e)n$. The experimental dependence $V_{gn}(n)$ can be used to determine the gap parameter Δ with a high accuracy (inset in Fig. 1). For the optimally doped BSCCO(La) samples with $T_c = 91 \pm 2$ K, $\Delta_{4.2\,\mathrm{K}} = (27 \pm 0.5)$ meV and $2\Delta/kT_c = 6.9 \pm 0.5$. With a rise in temperature, the gap structure in the CVCs of stacks retains its sharp shape over a sufficiently wide temperature interval, allowing the temperature dependence $\Delta(T)$ to be determined for the gap (Fig. 2).

It was found that the CVCs of the stacked S–I–S junctions coincide well in the reduced coordinates. The gap singularity in CVC has the shape typical of the "*s*-symmetric" (isotropic) gap parameter. At first glance, this result is hard to fit to the photoemission data, according to which the gap parameter in the *ab* plane is highly anisotropic [19]. There are, however, a number of reasons why the shape of gap singularity, even in the case of *d* pairing, can closely resemble the shape corresponding to the isotropic order parameter. First, it was shown in [30] that the Van Hove singularity renders the gap structure in the CVCs of junctions much more prominent even if the order parameter in the *ab* plane is strongly anisotropic. Second, for the tunneling in the *c* direction, which is most likely to occur in our experiments, one should take into account that the overlap integral $t_\perp$ in the *c* direction depends strongly on the wave vectors in the *ab* plane and has the form [31]

$$t_\perp \approx (\cos k_x a - \cos k_y a). \qquad (1)$$

Thus, it turns to zero simultaneously with the superconducting gap, so that tunneling from the zero-gap regions does not occur. It is worth noting that the CVC shape similar to ours was observed in [32] at the natural ultrathin steps (mesas).

It should also be noted that poorly defined gap structure (pseudogap), which is observed in some cases in the CVCs of Bi- 2212 mesas at $T > T_c$ [32, 33], bears no direct relation to the superconductivity and, probably, is a consequence of the two- dimensionality of metallic CuO_2 blocks. Note that the influence of 2D (surface) bands on the CVCs of normal tunneling junctions was considered in the theoretical work of Ben Daniel and Duke [34]. A "multigap" structure predicted by the authors of [34] was observed in [35] in the CVCs of normal Bi–Al_2O_3–Al junctions over a very wide temperature range.

2.3. Josephson Spectroscopy; Excitation of Raman Active (Nonpolar) Optical Phonons by ac Josephson Current in the HTSC Josephson Junctions over the Frequency Range up to 20 THz

As was mentioned above, there is some evidence of the strong electron–phonon interaction (EPI) in HTSC cuprates [2, 8]. This was confirmed, in particular, by studying the excitation of optical Raman active phonons by ac Josephson current in Bi-2201, Bi-2212, and Bi-2223 Josephson junctions over the frequency range up to 20 THz [36–40] (Fig. 2), by photoemission data [41], and by studying the isotope effect [42, 43] and the renormalization of the quasiparticle density of states at $T < T_c$ [44–46].

The fine structure in the CVCs of Josephson Bi-2212 junctions was first observed in [47] and, as it is now clear, was due to the excitation of nonpolar optical phonons by ac Josephson current in the energy range $\varepsilon_{ph} = 38$–54 meV. More recently [48, 49], resonances with optical modes corresponding to the vibrations of heavy bismuth, strontium, and copper ions ($\varepsilon_{ph} = 6$–24 meV) were observed in the CVCs of the Bi-2212 mesa structures. The phenomenological theory describing the interaction of ac Josephson current with IR-active (polar) optical phonons was proposed in [49, 50]. The theory involving the interaction with all (Raman and IR-active) optical modes was developed by one of us in [40]. In that work, it was shown that the phonon emission by the Josephson current flowing through the tunneling junction gives rise to an excess dc current $\Delta I(V)$. This current can be expressed in terms of the Josephson current $J_P(V)$ and the phonon Green's function as

$$\Delta I(V) = \sum_\lambda \frac{\alpha_{0\lambda}^2 \omega_{0\lambda}}{e} \frac{\gamma\omega_j [\mathrm{Re}\, J_P(\omega_j/2)]}{(\omega_j^2 - \omega_{0\lambda}^2)^2 + \gamma^2\omega_j^2}. \qquad (2)$$

Here, $\alpha^2_{0\lambda}$ is the coupling constant of optical phonons and electrons for the wave vector $q = 0$, γ is the phonon damping constant due to the anharmonicity or electron–phonon interaction, and $\omega_{0\lambda}$ is the phonon frequency. The quantity ω_j is expressed through the voltage V on the junction by the Josephson relation

$$\omega_j = 2eV/\hbar. \quad (3)$$

A similar expression, though naturally without the Josephson current, can be written for the intensity of Raman scattering by optical phonons. Equation (2) demonstrates that the excess current ΔI has peaks at voltages satisfying the condition

$$2eV = \hbar\omega_{0\lambda}. \quad (4)$$

Accordingly, the quantity dI/dV has minima at voltages close to the values given by Eq. (4). The difference between the positions of the maxima of ΔI and minima of dI/dV is small and is determined by the phonon damping constant γ.

In [37], the interaction of ac current with Raman active phonon modes, including the apical oxygen mode ($\varepsilon_{ph} \approx 80$ meV) was observed over the whole range of phonon frequencies (up to 20 THz; Fig. 3). One can clearly see in Fig. 3 that the intragap features in the CVC curves coincide well with the spectrum of Raman active phonons in optical experiments [51]. In the upper part of Fig. 3, the fragments of resonance structure in the dI/dV curves of several break junctions are shown as functions of $2eV$ for the near-optimum doped Bi-2212 single crystals at $T = 4.2$ K. The structure is observed in the energy range $0 \le 2eV \le 85$ meV, which covers the range of Raman active optical phonons in Bi-2212. It is worth noting that the resonance structure appears at the biases V satisfying the condition $2eV = \hbar\omega_{ph}$. For comparison, the results of measuring Raman spectra of Bi-2212 [51] are presented in the bottom of the figure for two main polarizations (curves *1* and *2* correspond to the $Z(X, X)Z$ geometry and curve *3* is for the $Y(Z, Z)Y$ geometry). The bars in the central part of Fig. 3 indicate the energies of Raman active phonons corresponding to the atomic vibrations in the Bi-2212 structure (see Table 1 in [37]).

Further experimental studies of the low-frequency resonances (Bi-, Sr-, and Cu-related optical modes) in the CVCs of break junctions in the Bi-2201(La) single crystals have shown that the ac Josephson current excites optical phonons not only in the SIS but also in the SNS junctions [39], unequivocally confirming the validity of our model [40]. It was also established that the CVC structure due to the excitation of optical modes in the doped Bi-2212(La) Josephson junctions is observed both in underdoped and overdoped single crystals and that the degree of doping has little effect on the frequency of the main phonon modes [39]. This signifies that the electron–phonon coupling strength in

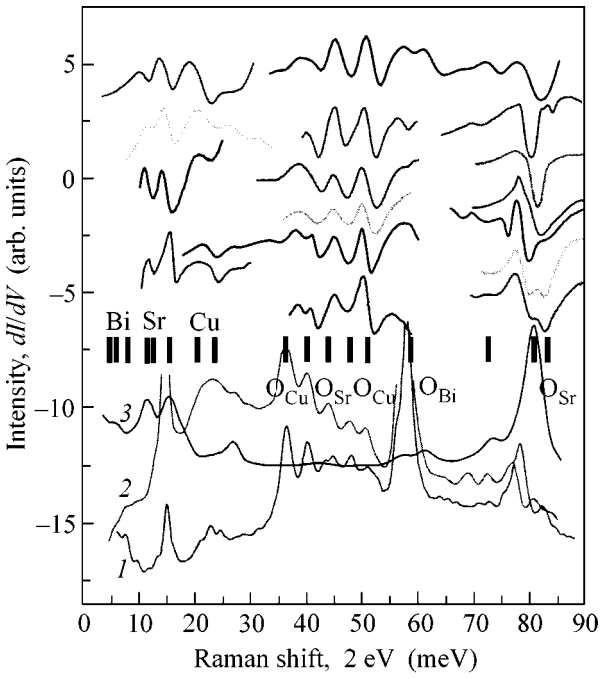

Fig. 3. Comparison of the structure due to the excitation of optical phonons by ac Josephson current in $dI(V)/dV$ characteristics of the Josephson Bi-2212 junctions with the Raman phonon spectra of Bi-2212 (see text).

BSCCO does not change appreciably in the whole domain of existence of superconductivity.

The studies of the internal Josephson effect in microsteps at the surface of cryogenic cracks in BSCCO with few SIS junctions showed [39] that, in some cases, the nonequilibrium optical phonons were generated synchronously. It should also be noted that the temperature anomalies of 2Δ were observed in [39] for the Cu-related phonon mode at $T < T_c$ in near-optimum doped Bi-2201(La) samples. It is conceivable that these anomalies are caused by the renormalization of the optical phonons with $k \longrightarrow 0$ and frequencies close to $2\Delta(0)$ in HTSC materials with strong electron–phonon coupling at $T < T_c$. Depending on the $\omega_0/2\Delta$ ratio, where ω_0 is the phonon frequency at $T > T_c$, the phonon frequencies at $T < T_c$ should either increase anomalously ($\omega_0/2\Delta > 1$) or decrease (soften) anomalously ($\omega_0/2\Delta \le 1$) with lowering temperature.

2.4. Andreev, Tunneling, and Internal-Tunneling Spectroscopies; Influence of Doping on the Superconducting Gap Δ in Bismuth Cuprates

It is well known that the underdoped HTSC cuprates have two gaps Δp and Δs in the electronic excitation spectrum [18]. It has recently been assumed [54] that the larger gap Δp (pseudogap) measured over a wide temperature range in the underdoped HTSC cuprates by photoemission or tunneling spectroscopy characterizes the binding energy $2\Delta p$ of Cooper pairs that remain

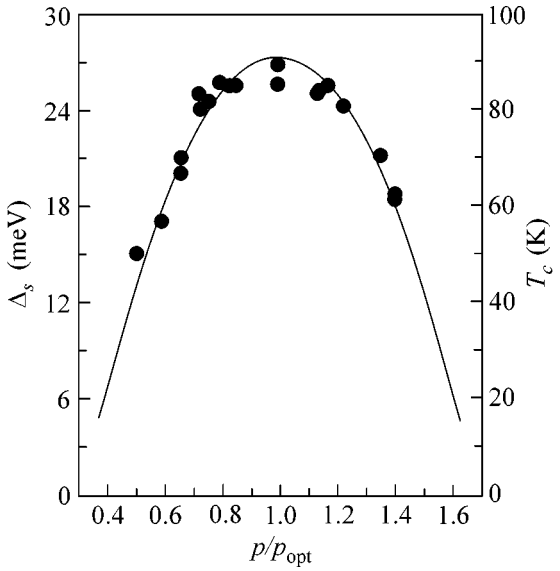

Fig. 4. Superconducting gap and $2\Delta/kT_c$ as functions of the reduced concentration p/p_{opt} of impurity holes in Bi-2212.

in the incoherent state at $T > T_c$. The smaller gap Δs (superconducting gap), as measured using Andreev or Raman spectroscopy, defines the minimal excitation energy $2\Delta s$ of superconducting condensate at $T < T_c$ ($T_c < T^*$ in the underdoped samples). According to the model suggested in [54], the superconducting gap Δ_s changes with changing hole concentration p in parallel with T_c and passes through a maximum at the point of optimum doping (scaling between Δ_s and T_c). At the same time, Δ_p increases monotonically as $p \longrightarrow 0$ (i.e., upon passing from the overdoped to the underdoped samples).

Note that no scaling relationship between Δ_s and T_c was observed in the doped HTSC materials in some works where STM spectroscopy was mostly used [55–58]. At the same time, the detailed studies in works [59–61] have confirmed the scaling model for Δ_s and T_c (in bismuth cuprates at least).

In [59–61], the CVCs of Josephson break junctions were measured over a wide temperature range up to the critical temperature T_c. The following objects were used for the investigation:

(1) underdoped (UND), optimally doped (OPD), and overdoped (OVD) Bi-2201(La) single crystals;

(2) underdoped (UND) and optimally doped (OPD) Bi-2212(La) single crystals and overdoped (OVD) Bi-2212 single crystals and whiskers.

The following experimental techniques were used:

(1) Andreev spectroscopy (multiple Andreev reflections in the SNS-type microjunctions),

(2) tunneling spectroscopy (single tunneling SIS junctions),

(3) internal-tunneling spectroscopy (internal Josephson effect in microsteps at the surface of cryogenic cleavages).

All these methods of studying the superconducting properties of HTSC materials are implemented using break junctions in HTSC single crystals and whiskers. Passing from one measurement regime to the other can be accomplished by mechanical changing the break junction at helium temperature.

Note that there are specific difficulties in obtaining single tunneling HTSC junctions at **j** ‖ **c** because of the layered structure of cuprate samples (in the **c** direction, the edges of tunneling junction represent a natural stack of SIS Josephson junctions). The superconducting current in the **c** direction is often suppressed near the surfaces of the (especially underdoped) samples. A single CuO_2 block cannot completely screen an external electric field in the **c** direction, because the screening length exceeds the thickness of this block [62]. In this case, a number of strongly nonequivalent additional SIS junctions arise in series with the main (planned) junction, which may shift the overall gap structure in the CVCs to larger biases. This effect was repeatedly observed in [59–61] in the underdoped samples. To reject CVCs of the complicated junctions, phonon resonances were used in [59–61], which were clearly seen in the dI/dV characteristics in the presence of ac Josephson current. These resonances serve as reliable calibration marks in the CVCs and allow a true single junction to be distinguished from the complicated combined junction. As is mentioned in Section 2.3, the biases at which CVC features appear due to the interaction of ac Josephson current with optical phonons are determined from the condition $2eV = \hbar\omega_{ph}$. For the stack junctions this condition changes to $2eV/n = \hbar\omega_{ph}$, where n is the number of junctions in the stack.

Note that these difficulties are, probably, the reason why the gap in the underdoped Bi-2212 samples is strongly overstated in [55–58].

In [59–61], the gap structure in the dI/dV characteristic of a junction in the tunneling regime (a peak of differential conductivity at the gap bias $V_g = 2\Delta/e$) became the same as the subharmonic gap structure in the dI/dV characteristic of the same junction in the microjunction (Andreev) regime (a set of dips in the differential conductivity for biases $V_g = 2\Delta/en$, where n is an integer). Similar work was carried out earlier with a niobium break junction [63]. The value of the superconducting gap was assumed to be reliable only if the Δ values obtained by the two above-mentioned methods were the same. The data of tunneling, internal tunneling, and Andreev spectroscopies were used to construct the dependence of superconducting gap Δ on the concentration p of impurity holes in Bi-2212 (Fig. 4).

One can see from Fig. 4 that there is a scaling relation between the superconducting gap Δ ($T = 4.2$ K) and the critical temperature T_c over the whole doping range. The dependence of superconducting gap Δ on the dop-

ing level in Bi-2212 shows a weak plateau in the optimum doping region (Fig. 4), which is probably a consequence of Fermi level pinning by the Van Hove singularity. To first approximation, the ratio $2\Delta/kT_c = 7.0 \pm 0.5$ is independent of doping. Similar behavior is observed for the superconducting gap in Bi-2201 as well [59–61], though at the ratio $2\Delta/kT_c \approx 12$. These results are in conflict with the results of some other works [55–58], according to which the gap Δ in the underdoped Bi-2212 samples increases drastically with lowering T_c, so that the $2\Delta/kT_c$ ratio attains a value of 20 and larger.

It was also established in [59–61] that the gap measured by tunneling and microjunction spectroscopies goes, as it must, to zero in the region where the resistance becomes zero at the resistive transition (i.e., at $T = T_c$) in the UND, OPD, and OVD samples of the Bi-2212 and Bi-2201 phases, in contrast to the results obtained in [56, 57], according to which the superconducting gap in underdoped samples is independent of temperature and becomes a pseudogap of the same value at $T = T_c$.

We do not deny the presence of a pseudogap in the underdoped HTSC cuprates. However, the following facts deserve attention. First, it was shown in the experiments on measuring electronic heat capacity [64] and in studying the magnetic-field effect on the CVCs [33] in the underdoping regime that the pseudogap is related neither to the superconducting fluctuations nor to the uncorrelated Cooper pairs higher than T_c. The pseudogap has a different nature, which is not related directly to the superconductivity. Second, tunneling spectroscopy is not the best method of studying the pseudogap properties, especially in the normal state, where it mainly accounts for the surface properties of the samples. It has been pointed out in theoretical work [34] that the CVCs of the normal tunneling junctions can be strongly influenced by the 2D surface bands. A multigap structure that was predicted by the authors of [34] was observed in [35] over a very wide temperature range in the CVCs of normal Bi–Al_2O_3–Al junctions. In this respect, special care should be taken in the STM measurements, where, as was shown in [65], the tunneling current may depend strongly on the impurities, tip, etc.

Note in conclusion that the superconducting gap Δ increases linearly as a function of the number n of CuO_2 planes in the superconducting blocks of the optimally doped samples of cuprate families $Bi_2Sr_2Ca_{n-1}Cu_nO_{2n+4+\delta}$, $Tl_2Ba_2Ca_{n-1}Cu_nO_{2n+4+\delta}$, and $HgBa_2Ca_{n-1}Cu_nO_{2n+2+\delta}$ ($1 \le n \le 3$) [59]. Recall that the dependence of maximal critical temperature $T_{c\max}$ on n in cuprates does not obey a simple linear law [66]. Our observations of the linear relation between the superconducting gap and the number of CuO_2 layers are confirmed by the photoemission data. However, we do not know any simple theoretical explanation for such a behavior of the gap. There are a number of models [4] which can account for an increase in the T_c and the gap as the number n of layers increases. It should, however, be noted, first, that rigorous proof for the applicability of these models to the HTSC materials is lacking and, second, that these models do not provide a linear relation between the gap and the number of layers [67].

We are grateful to V.L. Ginzburg, V.F. Gantmakher, Yu.M. Kagan, M.P. Trunin, and L.M. Fisher for useful discussions of the results of our work. This work was supported in part by the Scientific Council of the Russian Scientific and Technical program "Topical Directions in Condensed Matter Physics" (projects "Delta" and "HTSC-64") and the Russian Foundation for Basic Research (project nos. 99-06-16366 and 02-02-17915).

REFERENCES

1. V. L. Ginzburg, Usp. Fiz. Nauk **170**, 619 (2000).
2. E. G. Maksimov, Usp. Fiz. Nauk **170**, 1033 (2000).
3. Yu. A. Izyumov, Usp. Fiz. Nauk **169**, 225 (1999).
4. P. W. Andersen, *The Theory of Superconductivity in the High-T_c Cuprates* (Addison-Wesley, Reading, 1990).
5. D. J. Scalapino, Phys. Rep. **250**, 329 (1995).
6. A. A. Abrikosov, Physica C (Amsterdam) **341–348**, 97 (2000).
7. D. Pines, Turk. J. Phys. **20**, 535 (1996).
8. M. L. Kulic, Phys. Rep. **338**, 1 (2000).
9. L. N. Bulaevskii, Turk. J. Phys. **20**, 594 (1996).
10. A. A. Abrikosov, Phys. Rev. B **55**, 11735 (1997).
11. N. Nucker, H. Rombers, S. Nakai, *et al.*, Phys. Rev. B **39**, 12379 (1989).
12. *Problems in High-Temperature Superconductivity*, Ed. by V. L. Ginzburg and D. A. Kirzhnits (Nauka, Moscow, 1977).
13. W. E. Pickett, Rev. Mod. Phys. **61**, 433 (1989).
14. A. A. Abrikosov, Phys. Rev. B **64**, 104521 (2001).
15. D. S. Dessau, Z.-X. Shen, D. M. King, *et al.*, Phys. Rev. Lett. **71**, 2781 (1993).
16. U. S. Uchida, T. Ido, H. Takagi, *et al.*, Phys. Rev. B **43**, 7942 (1991).
17. H. Ding, M. R. Norman, T. Yokoya, *et al.*, Phys. Rev. Lett. **78**, 2628 (1997).
18. T. Timusk and B. Statt, Rep. Prog. Phys. **62**, 61 (1999).
19. Z.-X. Shen and D. S. Dessau, Phys. Rep. **253**, 1 (1995).
20. I. Vobornik, R. Gatt, T. Schmauder, *et al.*, Physica C (Amsterdam) **317–318**, 589 (1999).
21. R. Kleiner and P. Müller, Phys. Rev. B **49**, 1327 (1994); K. Schlenga, R. Kleiner, G. Hechtfischer, *et al.*, Phys. Rev. B **57**, 14518 (1998).
22. R. Kleiner and P. Müller, Physica C (Amsterdam) **293**, 156 (1997).
23. S. Heim, T. Nachtrab, M. Möβle, *et al.*, cond-mat/0107463 (2001).
24. A. A. Yurgens, Supercond. Sci. Technol. **13**, R85 (2000).
25. V. N. Krasnov, N. Mros, A. Yurgens, and D. Winkler, Phys. Rev. B **59**, 8463 (1999).

26. T. Yamashita, S.-J. Kim, Y. Latyshev, and K. Nakajima, Physica C (Amsterdam) **335**, 219 (2000).
27. Ya. G. Ponomarev, Chong Soon Khi, Kim Ki Uk, *et al.*, Physica C (Amsterdam) **315**, 85 (1999).
28. S. Kaneko, H. Sakata, Y. Ono, *et al.*, Surf. Sci. **438**, 353 (1999).
29. C. E. J. Mitchell, E. Whittaker, W. R. Flavell, and L. Leonyuk, Surf. Sci. **433–435**, 728 (1999).
30. J. Y. T. Wei, C. C. Tsuei, P. J. M. van Bentum, *et al.*, Phys. Rev. B **57**, 3650 (1998).
31. O. K. Andersen, A. I. Liechtenstein, O. Jepsen, *et al.*, J. Phys. Chem. Solids **56**, 1573 (1995).
32. M. Suzuki, T. Watanabe, and A. Matsuda, Phys. Rev. Lett. **82**, 5361 (1999); M. Suzuki and T. Watanabe, Phys. Rev. Lett. **85**, 4787 (2000).
33. V. M. Krasnov, A. E. Kovalev, A. Yurgens, *et al.*, Phys. Rev. Lett. **86**, 2657 (2001); cond-mat/0002172 (2000).
34. D. J. Ben Daniel and C. B. Duke, Phys. Rev. **152**, 683 (1966); Phys. Rev. **160**, 679 (1967).
35. G. A. Mironova, Ya. G. Ponomarev, and L. Roshta, Fiz. Tverd. Tela (Leningrad) **17**, 906 (1975) [Sov. Phys. Solid State **17**, 574 (1975)].
36. Ya. G. Ponomarev, E. B. Tsokur, M. V. Sudakova, *et al.*, Solid State Commun. **111**, 513 (1999).
37. Ya. G. Ponomarev, A. I. Kuzmitch, E. B. Tsokur, *et al.*, in *Abstracts of the 5th International Workshop in High-Temperature Superconductivity and Novel Inorganic Materials Engineering (MSU-HTSC V), Moscow, 1998*, S-59.
38. M. A. Lorenz, M. A. Hein, and G. Müller, J. Low Temp. Phys. **117**, 527 (1999).
39. Ya. G. Ponomarev, M. E. Shabalin, A. I. Kuzmich, *et al.*, in *Proceedings of the XXXI Conference on Low Temperature Physics, Moscow, 1998*, pp. 228–229.
40. E. G. Maksimov, P. I. Arseev, and N. S. Maslova, Solid State Commun. **111**, 391 (1999).
41. A. Lanzara, P. V. Bogdanov, X. J. Zhou, *et al.*, Nature **412**, 510 (2001).
42. G. M. Zhao, M. B. Hunt, H. Keller, and K. A. Muller, Nature (London) **385**, 236 (1997).
43. J. P. Franck, J. Jung, A.-K. Mohamed, *et al.*, Phys. Rev. B **44**, 5318 (1991).
44. S. I. Vedeneev, A. A. Tsvetkov, A. G. M. Jansen, and P. Wyder, Physica C (Amsterdam) **235–240**, 1851 (1994).
45. D. Shimada, N. Tsuda, U. Paltzer, and F. W. de Wette, Physica C (Amsterdam) **298**, 195 (1998).
46. R. S. Gonnelli, G. A. Ummarino, and V. A. Stepanov, Physica C (Amsterdam) **275**, 162 (1997).
47. B. A. Aminov, A. A. Bush, L. I. Leonyuk, *et al.*, Springer Proc. Phys. **64**, 45 (1992).
48. A. Yurgens, D. Winkler, N. Zavaritsky, and T. Claeson, Proc. SPIE **2697**, 433 (1996).
49. K. Schlenga, G. Hechtfischer, R. Kleiner, *et al.*, Phys. Rev. Lett. **76**, 4943 (1996).
50. Ch. Helm, Ch. Preis, F. Forsthofer, *et al.*, Phys. Rev. Lett. **79**, 737 (1997); cond-mat/9909318 (1999).
51. C. Thomsen, in *Light Scattering in Solids VI*, Ed. by M. Cardona and C. Günterrodt (Springer-Verlag, Berlin, 1991), p. 285.
52. R. Zeyer and G. Zwicknagl, Z. Phys. B **78**, 175 (1990).
53. A. E. Karakozov and E. G. Maksimov, Zh. Éksp. Teor. Fiz. **115**, 1799 (1999) [JETP **88**, 987 (1999)].
54. G. Deutscher, Nature **397**, 410 (1999).
55. L. Ozyuzer, J. F. Zasadzinski, N. Miyakawa, *et al.*, Physica C (Amsterdam) **341–348**, 927 (2000).
56. N. Miyakawa, J. F. Zasadzinski, L. Ozyuzer, *et al.*, Phys. Rev. Lett. **83**, 1018 (1999).
57. Ch. Renner, B. Revaz, J.-Y. Genoud, *et al.*, Phys. Rev. Lett. **80**, 149 (1998).
58. M. Oda, R. M. Dipasupil, N. Momono, *et al.*, Int. J. Mod. Phys. **13**, 3605 (1999).
59. Ya. G. Ponomarev, Kim Ki Uk, M. A. Lorenz, *et al.*, Inst. Phys. Conf. Ser. **167**, 241 (2000).
60. H. Schmidt, in *Abstracts of the International Conference M^2 2S-HTSC-VI, Houston, Texas, 2000*, 2C2.6, p. 170.
61. N. Z. Timergaleev, in *Abstracts of the All-Russia Conference on Low Temperatures, 2000*, SCP30, p. 104.
62. M. Machida, T. Koyama, and M. Tachiki, Phys. Rev. Lett. **83**, 4618 (1999).
63. C. J. Muller, J. M. van Ruitenberg, and L. J. de Jongh, Physica C (Amsterdam) **191**, 485 (1992).
64. J. L. Tallon, G. V. M. Williams, and J. W. Loram, Physica C (Amsterdam) **338**, 9 (2000).
65. A. Depuydt, C. van Haesendonck, and N. S. Maslova, Phys. Rev. B **60**, 2619 (1999).
66. J. C. Phillips, Phys. Rev. Lett. **72**, 3863 (1994).
67. A. J. Sudbø, J. Low Temp. Phys. **97**, 403 (1993).

Translated by V. Sakun

JETP Letters, Vol. 76, No. 6, 2002, pp. 401.

ERRATA

Erratum: Neutrino Mixing and Leptonic CP Phase in Neutrino Oscillations (Pis'ma Zh. Éksp. Teor. Fiz. 74, 157 (2002) [JETP Lett. 74, 139 (2002)])

D. A. Ryzhikh and K. A. Ter-Martirosyan

PACS numbers: 14.60.Pq; 99.10.+g

In the article of D.A. Ryzhikh and K.A. Ter-Martirosyan published in vol. 74, no. 3, pp. 139–143:

c_{13} should be replaced by c_{23} in the third row of Eq. (6), in the second row of Eq. (8), and in the first and seventh rows of Eq. (9).

We are grateful to Prof. Luciano Moscoso for attention and for pinpointing these misprints.

0021-3640/02/7606-0401$22.00

JETP Letters, Vol. 76, No. 6, 2002, pp. 401.

ERRATA

Erratum: Optical Chaos in Nonlinear Photonic Crystals (Pis'ma Zh. Éksp. Teor. Fiz. 75, 206 (2002) [JETP Lett. 75, 174 (2002)])

K. N. Alekseev and A. V. Ponomarev

PACS numbers: 42.65.Sf; 42.70.Mp; 42.65.Ky; 42.65.Hw; 99.10.+g

In the article of K.N. Alekseev and A.V. Ponomarev published in vol. 75, no. 4, pp. 174–178,

(1) $10\chi_{max}$ should be written instead of χ_{max} in Fig. 3;
(2) the article was received January 9, 2002.